

Investigation of Pseudo-Passive Layer Formation in CO<sub>2</sub> Corrosion

A thesis presented to  
the faculty of  
the Russ College of Engineering and Technology of Ohio University

In partial fulfillment  
of the requirements for the degree  
Master of Science

Wei Li

June 2011

©2011 Wei Li. All Rights Reserved.

This thesis titled  
Investigation of Pseudo-Passive Layer Formation in CO<sub>2</sub> Corrosion

by  
WEI LI

has been approved for  
the Department of Chemical and Biomolecular Engineering  
and the Russ College of Engineering and Technology by

---

Srdjan Nešić

Professor of Chemical and Biomolecular Engineering

---

Dennis Irwin

Dean, Russ College of Engineering and Technology

## ABSTRACT

LI, WEI, M.S., June 2011, Chemical Engineering

Investigation of Pseudo-Passive Layer Formation in CO<sub>2</sub> Corrosion

Director of Thesis: Srdjan Nešić

CO<sub>2</sub> corrosion is one of the most important forms of corrosion in the oil and gas industry. However, the role of corrosion product layers in CO<sub>2</sub> corrosion remains poorly understood.

In this thesis, the pseudo-passive effect of the CO<sub>2</sub> corrosion product layer on the steel surface has been investigated at elevated temperature over a relatively wide bulk pH range. Electrochemical techniques (LPR, EIS, EFM and potentiodynamic polarization) have been utilized to monitor the formation of this pseudo-passive layer. Materials characterization methods (SEM-EDS, XRD/GIXRD, and TEM-EDS) have been employed to determine its chemical composition and structure. Pseudo-passivity occurred at pH values of 6.0 and above, a dense and continuous sublayer underneath the top corrosion product layer may be the cause of this pseudo-passive behavior.

Approved: \_\_\_\_\_

Srdjan Nešić

Professor of Chemical and Biomolecular Engineering

## ACKNOWLEDGMENTS

I would like to express my sincere gratitude to my advisor, Dr. Srdjan Nešić, for his guidance and advice throughout this program. His mentoring and support have encouraged me to explore the exciting research areas of electrochemical engineering and materials science.

I also would like to thank my parents, Duanfu Li and Airon Yan for their great love and support, which help their son to cope with the stresses in pursuit of advanced studies overseas.

Many thanks also go to my project leader, Bruce Brown, for his great help and advice in my research project. I really enjoy and benefit from the academic discussions between us. I also would like to thank the technicians in the institute for their technical assistance in my research. Special mention is given to Cody Shafer and Daniel Cain.

I would like show my deep appreciation to Dr. David Young, Dr. Yoon-Seok Choi and Professor Brian Kinsella for their academic advices in this project, which greatly broaden my research insight.

I gratefully acknowledge the collaborators for their help of surface analysis in this project: Dr. Yiyun Li from the Department of Materials Science and Engineering at the Ohio State University, Dr. Akhilesh Tripathi from Rigaku Inc. and Dr. Brian Hassler from CEER of Ohio University.

Last but not least, I would like to thank all the staff and students in the Institute for Corrosion and Multiphase Technology at Ohio University for having provided a wonderful working environment.

## TABLE OF CONTENTS

	Page
Abstract.....	3
Acknowledgments.....	4
List of Tables .....	7
List of Figures.....	8
Chapter 1: Introduction.....	13
1.1 CO <sub>2</sub> Corrosion.....	13
1.2 CO <sub>2</sub> Corrosion Product Layer.....	16
1.3 Electrochemical Techniques for Corrosion Study.....	18
1.3.1 Principles of Electrochemical Techniques.....	18
1.3.2 Electrochemical Techniques for Corrosion Study.....	24
Chapter 2: Research Objectives.....	29
Chapter 3: Evaluation of the Electrochemical Frequency Modulation Technique in CO <sub>2</sub> Corrosion Systems .....	31
3.1 Introduction.....	31
3.2 Experimental.....	31
3.2.1 Experimental Setup and Instrumentation.....	31
3.2.2 Test Matrix.....	33
3.2.3 Procedure .....	35
3.2.4 Parameter Selections of Electrochemical Measurements .....	36
3.3 Results and Discussion .....	37
3.3.1 System 1 (5°C baseline).....	37
3.3.2 System 2 (25°C baseline).....	39
3.3.3 System 3 (K2 inhibitor system) .....	41
3.3.4 System 4 (K1 inhibitor system) .....	50
3.3.5 Summary & Conclusions .....	52
Chapter 4: Investigation of Pseudo-Passive Layer Formation in CO <sub>2</sub> Corrosion.....	54
4.1 Introduction.....	54
4.2 Experimental.....	56
4.2.1 Experimental Setup and Instrumentation.....	56

	6
4.2.2 Test Matrix.....	58
4.2.3 Procedure.....	58
4.2.4 Parameter Selections of Electrochemical Measurements.....	60
4.3 Results and Discussion.....	61
4.3.1 Tests at pH 7.8.....	61
4.3.2 Tests at pH 7.1.....	73
4.3.3 Tests at pH 6.6.....	93
4.3.4 Tests at pH 6.0.....	97
4.3.5 Tests at pH 5.6.....	104
4.3.6 Discussion.....	112
Chapter 5: Conclusions.....	113
References.....	115
Appendix: Mathematical Description of the EFM Technique.....	119
1. Activation Model.....	119
2. Diffusion Model.....	122
3. Passivation Model.....	123

## LIST OF TABLES

	Page
Table 1. Selected equilibrium constants for CO <sub>2</sub> corrosion water chemistry from literature [19-22] .....	16
Table 2. Chemical composition of X-65 carbon steel (wt.%) [44] .....	33
Table 3. Test matrix for evaluation of EFM technique in CO <sub>2</sub> corrosion systems .....	34
Table 4. Active chemical components of K1 and K2 inhibitors .....	34
Table 5. Parameter selections of electrochemical measurements .....	36
Table 6. Result comparisons of experimental techniques. 5°C, pH 6.0, 3 wt.% NaCl, 1 bar CO <sub>2</sub> , rotating speed 1000rpm, X-65 carbon steel, 1 day test .....	38
Table 7. Result comparisons of experimental techniques. 25°C, pH 4.0, 3 wt.% NaCl, 1 bar CO <sub>2</sub> , rotating speed 1000rpm, X-65 carbon steel, 1 day test .....	40
Table 8. Test matrix for pseudo-passive layer study in CO <sub>2</sub> corrosion system .....	58
Table 9. Parameter selections of electrochemical measurements .....	60
Table 10. Test arrangement at pH 7.1 .....	73

## LIST OF FIGURES

	Page
Figure 1. Illustration of corrosion current and Tafel slopes determination by polarization curves.....	24
Figure 2. Schematic of glass cell setup: (a) front view and (b) side view.....	32
Figure 3. Images of the cylindrical X-65 carbon steel sample: (a) side view and (b) top view.....	33
Figure 4. Potentiodynamic polarization curves. 5°C, pH 6.0, 3 wt.% NaCl, 1 bar CO <sub>2</sub> , rotating speed 1000rpm, X-65 carbon steel.....	38
Figure 5. Potentiodynamic polarization curves. 25°C, pH 4.0, 3 wt.% NaCl, 1 bar CO <sub>2</sub> , rotating speed 1000rpm, X-65 carbon steel.....	40
Figure 6. EFM result: corrosion rate vs. elapsed time. 3 wt. % NaCl, 25°C, 1 bar CO <sub>2</sub> , pH 4.0, X-65 carbon steel, electrode rotating speed 1000 rpm, 1041ppm K2 inhibitor...	42
Figure 7. EFM result: R <sub>ct</sub> vs. elapsed time. 3 wt. % NaCl, 25°C, 1 bar CO <sub>2</sub> , pH 4.0, X-65 carbon steel, electrode rotating speed 1000 rpm, 1041ppm K2 inhibitor.....	43
Figure 8. EFM result: anodic slope vs. elapsed time. 3 wt. % NaCl, 25°C, 1 bar CO <sub>2</sub> , pH 4.0, X-65 carbon steel, electrode rotating speed 1000 rpm, 1041ppm K2 inhibitor.....	43
Figure 9. EFM result: cathodic slope vs. elapsed time. 3 wt. % NaCl, 25°C, 1 bar CO <sub>2</sub> , pH 4.0, X-65 carbon steel, electrode rotating speed 1000 rpm, 1041ppm K2 inhibitor...	44
Figure 10. EFM result: B value vs. elapsed time. 3 wt. % NaCl, 25°C, 1 bar CO <sub>2</sub> , pH 4.0, X-65 carbon steel, electrode rotating speed 1000 rpm, 1041ppm K2 inhibitor.....	44
Figure 11. Causality factors vs. elapsed time. 3 wt. % NaCl, 25°C, 1 bar CO <sub>2</sub> , pH 4.0, X-65 carbon steel, electrode rotating speed 1000 rpm, 1041ppm K2 inhibitor.....	45
Figure 12. EFM: corrosion rate vs. elapsed time. 3 wt.% NaCl, 25°C, 1 bar CO <sub>2</sub> , pH 4.0, X-65 carbon steel, rotating speed 1000 rpm, sequential addition of K2 inhibitor: 42- 208 ppm. ....	47
Figure 13. EFM: anodic slope vs. elapsed time. 3 wt.% NaCl, 25°C, 1 bar CO <sub>2</sub> , pH 4.0, X-65 steel, rotating speed 1000 rpm, sequential addition of K2 inhibitor: 42- 208 ppm.	47
Figure 14. EFM: cathodic slope vs. elapsed time. 3 wt.% NaCl, 25°C, 1 bar CO <sub>2</sub> , pH 4.0, X-65 steel, rotating speed 1000 rpm, sequential addition of K2 inhibitor: 42- 208 ppm.	48
Figure 15. EFM: B value vs. elapsed time. 3 wt.% NaCl, 25°C, 1 bar CO <sub>2</sub> , pH 4.0, X-65 steel, rotating speed 1000 rpm, sequential addition of K2 inhibitor: 42- 208 ppm. ....	48
Figure 16. EIS: Nyquist plots at different test time. 3 wt.% NaCl, 25°C, 1 bar CO <sub>2</sub> , pH 4.0, X-65 steel, rotating speed 1000 rpm, sequential addition of K2 inhibitor: 42- 208 ppm. ....	49

Figure 17. Comparison of $R_{ct}$ measured by EFM and EIS. 3 wt.% NaCl, 25°C, 1 bar CO <sub>2</sub> , pH 4.0, X-65 steel, rotating speed 1000 rpm, sequential addition of K2 inhibitor: 42- 208 ppm. ....	49
Figure 18. EFM: corrosion rate vs. elapsed time. 3 wt.% NaCl, 25°C, 1 bar CO <sub>2</sub> , pH 4.0, X-65 steel, rotating speed 1000 rpm, sequential addition of K1 inhibitor: 10- 50 ppm. ..	51
Figure 19. EFM: B value vs. elapsed time. 3 wt.% NaCl, 25°C, 1 bar CO <sub>2</sub> , pH 4.0, X-65 steel, rotating speed 1000 rpm, sequential addition of K1 inhibitor: 10- 50 ppm. ....	51
Figure 20. Comparison of $R_{ct}$ for EFM and EIS. 3 wt.% NaCl, 25°C, 1 bar CO <sub>2</sub> , pH 4.0, X-65 steel, rotating speed 1000 rpm, sequential addition of K1 inhibitor: 10- 50 ppm. ..	52
Figure 21. Calculation of the dependency of FeCO <sub>3</sub> solubility on [Fe <sup>2+</sup> ] and pH. 80°C, 0.53 bar CO <sub>2</sub> , 1 wt.% NaCl.....	55
Figure 22. (a) Schematic of glass cell setup; (b) Zoomed in view of glass cell. ....	57
Figure 23. Pictures of (a) cylindrical sample and (b) hanging flat sample. ....	57
Figure 24. Comparison of open circuit potential during the test. 80°C, 0.53 bar CO <sub>2</sub> , stagnant, 1 wt.% NaCl, pH 7.8, X-65 carbon steel. ....	62
Figure 25. LPR corrosion rates during the formation of pseudo-passive layer. 80°C, pH 7.8, 1 wt.% NaCl, 0.53 bar CO <sub>2</sub> , stagnant flow, X-65 carbon steel.....	63
Figure 26. LPR corrosion rates using different polarization directions of test3. 80°C, 0.53 bar CO <sub>2</sub> , 1 wt.% NaCl, stagnant flow, pH 7.8. ....	64
Figure 27. Comparison of open circuit potential and corrosion potential for positive polarization LPR measurements and negative polarization LPR measurements of test4. 80°C, 0.53 bar CO <sub>2</sub> , 1 wt.% NaCl, stagnant flow, pH 7.8. ....	64
Figure 28. Comparison of EFM (active model) and LPR corrosion rates of test4. 80°C, 0.53 bar CO <sub>2</sub> , 1 wt.% NaCl, stagnant flow, pH 7.8. ....	65
Figure 29. Comparison of EFM (active model) and LPR results of test4 at corrosion rates measured below 0.1 mm/yr. 80°C, 0.53 bar CO <sub>2</sub> , 1 wt.% NaCl, stagnant, pH 7.8. .	66
Figure 30. Comparison of EFM (passive model) and LPR corrosion rates of test4. 80°C, 0.53 bar CO <sub>2</sub> , 1 wt.% NaCl, stagnant, pH 7.8.....	66
Figure 31. Nyquist plot of test3, 0.2 hour after the electrode immersed into the electrolyte. 80°C, 0.53 bar CO <sub>2</sub> , 1 wt.% NaCl, stagnant, pH 7.8.....	67
Figure 32. Comparison of the Nyquist plots during test3. 80°C, 0.53 bar CO <sub>2</sub> , 1 wt.% NaCl, stagnant, pH 7.8.....	68
Figure 33. Comparison of Nyquist plots: 42 hour of test3 and result from reference (E=0.5V) [47].....	68
Figure 34. SEM image of X65 flat sample of test2. 80°C, 0.53 bar CO <sub>2</sub> , 1 wt.% NaCl, stagnant flow, pH 7.8, after 38 hours.....	69

Figure 35. EDS result of X65 flat sample of test2. 80°C, 0.53 bar CO <sub>2</sub> , 1 wt.% NaCl, stagnant, pH 7.8, after 38 hours. ....	70
Figure 36. SEM image of X65 flat sample of test4. 80°C, 0.53 bar CO <sub>2</sub> , 1 wt.% NaCl, stagnant flow, pH 7.8, after 60 hours. ....	70
Figure 37. EDS result of X65 flat sample of test4. 80°C, 0.53 bar CO <sub>2</sub> , 1 wt.% NaCl, stagnant, pH 7.8, after 60 hours. ....	71
Figure 38. Conventional XRD pattern of X65 flat sample after test4 at pH 7.8. ....	71
Figure 39. GIXRD pattern of X65 flat sample after test4 at pH 7.8. ....	72
Figure 40. Open circuit potential during the short term test, 80°C, 0.53 bar CO <sub>2</sub> , 1 wt.% NaCl, stagnant, pH 7.1. ....	74
Figure 41. SEM image of X-65 flat sample after short term test. 80°C, 0.53 bar CO <sub>2</sub> , 1 wt.% NaCl, stagnant, pH 7.1. ....	74
Figure 42. Open circuit potential during the mid-term test, 80°C, 0.53 bar CO <sub>2</sub> , 1 wt.% NaCl, stagnant, pH 7.1. ....	75
Figure 43. LPR corrosion rate during the mid-term test, 80°C, 0.53 bar CO <sub>2</sub> , 1 wt.% NaCl, stagnant, pH 7.1. ....	76
Figure 44. SEM image of X65 flat sample after mid-term test. 80°C, 0.53 bar CO <sub>2</sub> , 1 wt.% NaCl, stagnant, pH 7.1. ....	76
Figure 45. Open circuit potential, long term test, 80°C, 0.53 bar CO <sub>2</sub> , 1 wt.% NaCl, stagnant, pH 7.1. ....	77
Figure 46. LPR, long term test, 80°C, 0.53 bar CO <sub>2</sub> , 1 wt.% NaCl, stagnant, pH 7.1. ....	78
Figure 47. Nyquist plot, 0.5 hour after the electrode immersed into the electrolyte. 80°C, 0.53 bar CO <sub>2</sub> , 1 wt.% NaCl, stagnant, pH 7.1. ....	78
Figure 48. Comparison of the Nyquist plots during the test. 80°C, 0.53 bar CO <sub>2</sub> , 1 wt.% NaCl, stagnant, pH 7.1. ....	79
Figure 49. Comparison of the Nyquist plots during the test in a zoomed in region. 80°C, 0.53 bar CO <sub>2</sub> , 1 wt.% NaCl, stagnant, pH 7.1. ....	79
Figure 50. SEM image of X65 flat sample after long term test. 80°C, 0.53 bar CO <sub>2</sub> , 1 wt.% NaCl, stagnant, pH 7.1. ....	80
Figure 51. GIXRD pattern of X65 flat sample after long term test. ....	81
Figure 52. SEM image of TEM sample cutting area after long term test. 80°C, 0.53 bar CO <sub>2</sub> , 1 wt.% NaCl, stagnant, pH 7.1. ....	82
Figure 53. Top view of TEM sample cutting area shown in Figure 52. ....	83
Figure 54. Side view of TEM sample cutting area with 55° tilt angle. ....	83
Figure 55. Side view of prepared TEM sample. ....	84

Figure 56. Specific locations analyzed by TEM-EDS.....	84
Figure 57. Location 1 shown in Figure 56 analyzed by TEM-EDS. ....	85
Figure 58. Line pattern EDS scan result of location 1 shown in Figure 57.....	85
Figure 59. TEM analysis areas of location 2 shown in Figure 56 and point A. ....	86
Figure 60. Zoomed in image of TEM analysis area at location 2 shown in Figure 59...	86
Figure 61. Line pattern EDS scan result of location 2 shown in Figure 59.....	87
Figure 62. Point pattern EDS result of Point A shown in Figure 59. ....	87
Figure 63. TEM analysis area of location 3 shown in Figure 56.....	88
Figure 64. Line pattern EDS scan result of location 3 shown in Figure 63.....	88
Figure 65. TEM analysis area of location 5 shown in Figure 56.....	89
Figure 66. Zoomed in image of TEM analysis area at location 5 shown in Figure 56...	89
Figure 67. Line pattern EDS scan result of location 5 shown in Figure 66.....	90
Figure 68. TEM analysis area of location 4 shown in Figure 56.....	90
Figure 69. Point pattern EDS result of location 4 shown in Figure 68.....	91
Figure 70. Anodic potentiodynamic polarization in the end of each test at pH 7.1 for short term, mid-term and long term tests and the corresponding surface morphology. ...	92
Figure 71. Open circuit potential during the test, 80°C, 0.53 bar CO <sub>2</sub> , 1 wt.% NaCl, stagnant, pH 6.6, initial [Fe <sup>2+</sup> ] = 50 ppm. ....	94
Figure 72. LPR corrosion rates during the test, 80°C, 0.53 bar CO <sub>2</sub> , 1 wt.% NaCl, initial [Fe <sup>2+</sup> ] = 50 ppm, stagnant, pH 6.6. ....	94
Figure 73. Comparison of the Nyquist plots during the test. 80°C, 0.53 bar CO <sub>2</sub> , 1 wt.% NaCl, stagnant, pH 6.6, initial [Fe <sup>2+</sup> ] = 50 ppm.....	95
Figure 74. SEM image of X65 flat sample after test, 80°C, 0.53 bar CO <sub>2</sub> , 1 wt.% NaCl, stagnant, pH 6.6, initial [Fe <sup>2+</sup> ] = 50 ppm. ....	95
Figure 75. SEM-EDS result of X65 flat sample after test. 80°C, 0.53 bar CO <sub>2</sub> , 1 wt.% NaCl, stagnant, pH 6.6, initial [Fe <sup>2+</sup> ] = 50 ppm.....	96
Figure 76. Variations of open circuit potential and corrosion rate with time. 80°C, 0.53 bar CO <sub>2</sub> , 1 wt.% NaCl, stagnant, pH 6.0, initial [Fe <sup>2+</sup> ] = 100 ppm. ....	98
Figure 77. Comparison of the Nyquist plots during the test. 80°C, 0.53 bar CO <sub>2</sub> , 1 wt.% NaCl, stagnant, pH 6.0, initial [Fe <sup>2+</sup> ] = 100 ppm.....	98
Figure 78. SEM images of X65 flat sample. 80°C, 0.53 bar CO <sub>2</sub> , 1 wt.% NaCl, stagnant, pH 6.0, initial [Fe <sup>2+</sup> ] = 100 ppm. Left: 6 days of test; right: 8 days of the test. ....	100
Figure 79. SEM-EDS data, X65 flat sample, 6 days of the test. 80°C, 0.53 bar CO <sub>2</sub> , 1 wt.% NaCl, stagnant, pH 6.0, initial [Fe <sup>2+</sup> ] = 100 ppm.....	100

Figure 80. SEM image, X65 cylindrical sample. 80°C, 0.53 bar CO <sub>2</sub> , 1 wt.% NaCl, stagnant, pH 6.0, initial [Fe <sup>2+</sup> ] = 100 ppm, 10 days of the test. ....	101
Figure 81. SEM images of X65 cylindrical sample cross-section. 80°C, 0.53 bar CO <sub>2</sub> , 1 wt.% NaCl, stagnant, pH 6.0, initial [Fe <sup>2+</sup> ] = 100 ppm, 10 days of the test. ....	101
Figure 82. SEM-EDS data of Fe substrate, X65 sample, 80°C, 0.53 bar CO <sub>2</sub> , 1 wt.% NaCl, stagnant, pH 6.0, initial [Fe <sup>2+</sup> ] = 100 ppm, 10 days of the test.....	102
Figure 83. SEM-EDS data of FeCO <sub>3</sub> layer, X65 sample, 80°C, 0.53 bar CO <sub>2</sub> , 1 wt.% NaCl, stagnant, pH 6.0, initial [Fe <sup>2+</sup> ] = 100 ppm, 10 days of the test.....	102
Figure 84. SEM-EDS data of epoxy layer. ....	103
Figure 85. XRD pattern of X65 flat sample, day 8 of test. 80°C, 0.53 bar CO <sub>2</sub> , 1 wt.% NaCl, stagnant, pH 6.0, initial [Fe <sup>2+</sup> ] = 100 ppm.....	103
Figure 86. Variations of open circuit potential and corrosion rate with time. 80°C, 0.53 bar CO <sub>2</sub> , 1 wt.% NaCl, stagnant, pH 5.6, initial [Fe <sup>2+</sup> ] = 1000 ppm. ....	105
Figure 87. [Fe <sup>2+</sup> ] variations with time. 80°C, 0.53 bar CO <sub>2</sub> , 1 wt.% NaCl, stagnant, pH 5.6, initial [Fe <sup>2+</sup> ] = 1000 ppm. ....	106
Figure 88. FeCO <sub>3</sub> saturation value variations with time. 80°C, 0.53 bar CO <sub>2</sub> , 1 wt.% NaCl, stagnant, pH 5.6, initial [Fe <sup>2+</sup> ] = 1000 ppm.....	106
Figure 89. Picture of test cell taken after 22 days of the test. 80°C, 0.53 bar CO <sub>2</sub> , 1 wt.% NaCl, stagnant, pH 5.6, initial [Fe <sup>2+</sup> ] = 1000 ppm.....	107
Figure 90. SEM images of X65 cylindrical sample. 80°C, 0.53 bar CO <sub>2</sub> , 1 wt.% NaCl, stagnant, pH 5.6, initial [Fe <sup>2+</sup> ] = 1000 ppm, 22 days of the test. ....	108
Figure 91. SEM images of X65 cylindrical sample cross-section. 80°C, 0.53 bar CO <sub>2</sub> , 1 wt.% NaCl, stagnant, pH 5.6, initial [Fe <sup>2+</sup> ] = 1000 ppm, 22 days of the test. ....	108
Figure 92. SEM-EDS data of epoxy, X65 cylindrical sample cross-section.....	109
Figure 93. SEM-EDS data of Fe substrate, X65 cylindrical sample cross-section.....	109
Figure 94. SEM-EDS data of FeCO <sub>3</sub> , X65 cylindrical sample cross-section.....	110
Figure 95. XRD pattern of X65 flat sample, day 22 of test. 80°C, 0.53 bar CO <sub>2</sub> , 1 wt.% NaCl, stagnant, pH 5.6, initial [Fe <sup>2+</sup> ] = 1000 ppm.....	110

## CHAPTER 1: INTRODUCTION

Corrosion is a big problem in society and industry. The direct corrosion cost in the U.S. was estimated to be \$276 billion annually, approximately 3.1% of the gross domestic product in 1998 [1]. Corrosion problems are more severe in the oil and gas industry as carbon steels are widely selected as the primary fabrication material for transport pipelines and facilities such as offshore structures [2]. Carbon steel is more readily available and much less expensive than alloy steel. However, it is more vulnerable to corrosion failure due to the corrosive operating environment which may contain high concentrations of corrosive species (e.g.,  $H_2S$ ,  $CO_2$ ) in transportation pipelines and field equipment [3].

To ensure a much safer and more efficient operation, understanding corrosion mechanisms and finding preventive measures are imperative missions for engineers.

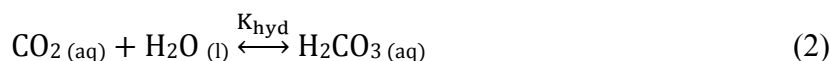
### 1.1 $CO_2$ Corrosion

$CO_2$  corrosion is one of the most well known forms of corrosion in the oil and gas industry, especially in upstream oil and gas production lines. In recent decades, extensive research concerning factors that affect  $CO_2$  corrosion, as well as the mechanisms involved, have been conducted [4-16]. Several factors such as  $CO_2$  partial pressure, temperature, pH, flow and salt concentration have been studied [14, 17]. An understanding of the mechanisms associated with uniform  $CO_2$  corrosion has become well developed over the past few decades. De Waard and Milliams first published their semi-empirical model of  $CO_2$  corrosion in the 1970s [4]. In the following decades, many

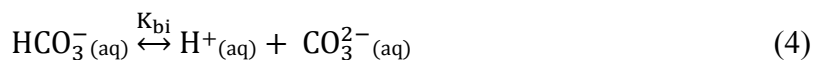
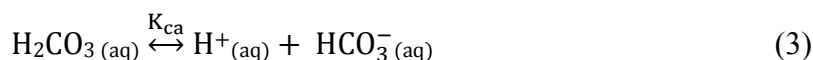
researchers have made great efforts on developing CO<sub>2</sub> corrosion models. Among them, Gray's and Nešić's mechanistic models have a profound effect on the understanding of CO<sub>2</sub> corrosion mechanisms. Gray, *et al.*, developed their electrochemical model in the late 1980s and early 1990s [7, 8]. Nešić, *et al.*, then improved Gray's model by proposing their electrochemical CO<sub>2</sub> corrosion mechanism which covers a confined range of selected corrosion parameters relating to pH, temperature, CO<sub>2</sub> partial pressure and flow velocity in the 1990s [9], further developing mechanistic models of CO<sub>2</sub> corrosion in the last decade [10-12]. With continuous improvement, the uniform CO<sub>2</sub> corrosion mechanism is now well understood. A number of chemical and electrochemical processes are involved in CO<sub>2</sub> corrosion; these are briefly shown below based on Shrier's book [18].

Several chemical reactions are involved in CO<sub>2</sub> corrosion.

First, CO<sub>2</sub> dissolves in water and forms carbonic acid:



Then, H<sub>2</sub>CO<sub>3</sub> partially dissociates in water and produces H<sup>+</sup>, HCO<sub>3</sub><sup>-</sup>, and CO<sub>3</sub><sup>2-</sup>:



In CO<sub>2</sub> corrosion of carbon steel, the anodic reaction is the electrochemical dissolution of iron in an aqueous solution:



The cathodic reactions, resulting in the evolution of hydrogen, can involve the reduction of  $H^+$ ,  $H_2CO_3$ ,  $HCO_3^-$  and/or  $H_2O$ :



In addition, water dissociation needs to be taken into account in an aqueous solution:



Consequently, the overall  $CO_2$  corrosion reaction can be written as:



Based on these reactions, the water chemistry of  $CO_2$  corrosion system can be calculated; the equilibrium constants and their individual expressions, adapted from literature, are listed in Table 1.

It can be seen that  $CO_2$  corrosion principally involves two electrochemical reactions, iron dissolution and hydrogen evolution. In a corrosion process, charge transfer (electron transport) or mass transfer (transport of reacting species) can be the rate determining step; in some cases, both steps can influence the overall process (mixed control). Factors such as  $CO_2$  partial pressure, temperature, pH, flow, etc. can affect this process.

Table 1. Selected equilibrium constants for CO<sub>2</sub> corrosion water chemistry from literature [19-22]

Equilibrium constants expression	Equilibrium constants value
$K_{sol} = \frac{[CO_2]}{P_{CO_2}}$	$K_{sol} = \frac{14.5}{1.00258} \times 10^{-(2.27 + 5.65 \times 10^{-3} T_f - 8.06 \times 10^{-6} T_f^2 + 0.0751)}$
$K_{hyd} = \frac{[H_2CO_3]}{[CO_2]}$	$K_{hyd} = 2.58 \times 10^{-3}$
$K_{ca} = \frac{[H^+][HCO_3^-]}{[H_2CO_3]}$	$K_{ca} = 387.6 \times 10^{-(6.41 - 1.594 \times 10^{-3} T_f + 8.52 \times 10^{-6} T_f^2 - 3.07 \times 10^{-5} p - 0.4772I^{0.5} + 0.118I)}$
$K_{bi} = \frac{[H^+][CO_3^{2-}]}{[HCO_3^-]}$	$K_{bi} = 10^{-(10.61 - 4.97 \times 10^{-3} T_f + 1.331 \times 10^{-5} T_f^2 - 2.624 \times 10^{-5} p - 1.166I^{0.5} + 0.3466I)}$
$K_{wa} = [H^+][OH^-]$	$K_{wa} = 10^{-(29.3868 - 0.0737549 \times T_K + 7.47881 \times 10^{-5} T_K^2)}$
$K_{sp} = [Fe^{2+}][CO_3^{2-}]$	$K_{sp} = 10^{-(59.3498 - 0.041377 T_K - \left(\frac{2.1963}{T_K}\right) + 24.5724 \log T_K + 2.518I^{0.5} - 0.6571I)}$

Where  $T_f$  is temperature in Fahrenheit,  $I$  is ionic strength,  $p$  is pressure in psi,  $T_k$  is temperature in Kelvin.

## 1.2 CO<sub>2</sub> Corrosion Product Layer

The role of product layer in CO<sub>2</sub> corrosion is poorly understood. The most commonly observed CO<sub>2</sub> corrosion product is iron carbonate (FeCO<sub>3</sub>). This can precipitate on the steel surface when the solution is saturated with respect to ferrous ion and carbonate species. The major criterion for FeCO<sub>3</sub> precipitation can be defined as supersaturation(SS) [11]. It is the ratio of the product of  $[Fe^{2+}]$  and  $[CO_3^{2-}]$  over the FeCO<sub>3</sub> solubility limit ( $K_{sp}$ ). This can be described in the following equation:

$$SS_{(FeCO_3)} = \frac{[Fe^{2+}] \times [CO_3^{2-}]}{K_{sp}} \quad (12)$$

When  $SS(\text{FeCO}_3) \geq 1$ ,  $\text{FeCO}_3$  is saturated in the solution and precipitation can occur anywhere in the solution, but precipitation and deposition will, in usual, preferably occur on the steel surface because of heterogeneous precipitation aided by the increased concentration of ferrous ions near the steel surface due to metal dissolution process. On the other hand, when  $SS(\text{FeCO}_3) < 1$  no stable layer is expected to form on the metal surface.

The effect of  $\text{CO}_2$  corrosion product layer on  $\text{CO}_2$  corrosion and influencing factors remains unclear [14, 23]. It has been reported that  $\text{FeCO}_3$  layer can serve as a mass transfer barrier [15] and have a surface coverage effect on  $\text{CO}_2$  corrosion, which provides protection to steel against corrosion. Han, *et al.*, observed significant increase of open circuit potential with a dramatic decrease in corrosion rate at pH 8.0 when the metal surface was covered by  $\text{FeCO}_3$  layer with trace amount of  $\text{Fe}_3\text{O}_4$ . They also explained that this phenomenon is due to the formation of pseudo-passive layer [24].

On the other hand, a gray zone [25], which describes a corrosion system with  $SS(\text{FeCO}_3)$  around 1, is considered as a highly dangerous corrosion scenario. The corrosion system in the gray zone reportedly results in incomplete  $\text{FeCO}_3$  layer surface coverage leading to the initiation and propagation of localized corrosion. According to the galvanic mechanism of Han, *et al.*, the potential difference between a bare steel surface and an  $\text{FeCO}_3$  covered surface can result in a galvanic cell being established leading to localized corrosion attack [16]. The factors that influence  $\text{FeCO}_3$  layer formation and stability are under investigation.

### 1.3 Electrochemical Techniques for Corrosion Study

Electrochemical methods are widely used in many areas of corrosion science such as in mechanistic studies and for *in-situ* corrosion measurements. Electrochemical techniques, by recording electrical signals such as potential, current and frequencies associated with the corrosion process can provide essential mechanistic and quantitative information of studied corrosion systems. Due to the development of related areas such as electrical engineering and computer science, instruments in electrochemistry have undergone tremendous improvement. Consequently, electrochemical techniques have become an important tool for corrosion research. In order to have a better understanding of electrochemical applications in corrosion studies, principles of electrochemistry in corrosion are briefly introduced in the following section.

#### *1.3.1 Principles of Electrochemical Techniques*

##### *1.3.1.1 Faraday's law of electrolysis*

One of the most important relationships in electrochemistry is Faraday's law of electrolysis. Faraday's law describes the quantitative relationship between the mass change of an electrode and current in an electrochemical reaction discovered by Michael Faraday in 1834 [26].

For a given electrochemical reaction:  $M^{z+} + ze^- \leftrightarrow M$ , a quantitative form of this law can be summarized by the following equation [27, 28]:

$$m = \frac{QM_w}{ZF} = \frac{ItM_w}{ZF} \quad (13)$$

Where:

$m$  is the mass of the substance altered

Q is the total electric charge passed through

$M_w$  is the atomic or molecular weight

Z is the number of electrons involved in the electrode reaction

F is the Faraday constant (96,485 C mol<sup>-1</sup>)

I is the current

t is the total time

Faraday's law is considered a fundamental principle of electrochemistry and corrosion science. Kelly stated "these empirical laws of electrolysis law are critical to corrosion as they allow electrical quantities to be related to mass changes and material loss rate" [29]. This law makes predicting corrosion rate with electrochemical measurements feasible.

### 1.3.1.2 Butler-Volmer equation

Another fundamental relationship in electrochemistry is the Butler-Volmer equation which had been developed based on the research of Butler and Volmer, from the 1920s to 1940s [30-32]. A corrosion process involves many steps. The Butler-Volmer equation assumes that the electrochemical process (charge transfer) is the slowest step. Thus, this is the rate determining step. Based on this assumption, for the electrochemical reaction:  $M^{z+} + ze^- \leftrightarrow M$ , after writing down the rate expressions for the anodic and cathodic reactions and conducting several mathematical manipulations, the final version of the Butler-Volmer equation can be written as:

$$i = |i_a - i_c| = i_0 \left[ \exp\left(\frac{(1-\alpha)ZF\eta}{RT}\right) - \exp\left(-\frac{\alpha ZF\eta}{RT}\right) \right] \quad (14)$$

Where:

$i$  is the overall current for an electrode

$i_a$  is the current for the anodic reaction

$i_c$  is the current for the cathodic reaction

$i_0$  is the exchange current density

$\eta$  is the overpotential,  $\eta = E_{(c/a)} - E_{eq}$

$\alpha$  is the charge transfer coefficient which is related to the activation energies of the electrochemical reactions (value of  $\alpha$  is between 0 and 1)

$Z$  is the number of electrons involved in the electrode reaction

$F$  is the Faraday constant ( $96,485 \text{ C mol}^{-1}$ )

$T$  is the absolute temperature (in K)

$R$  is the universal gas constant

The detailed derivation of Butler-Volmer equation can be found in Bard and Faulker's book [33]. In this equation, the approximate relationship of current density and overpotential in a corrosion process is described. It is the basis of many electrochemical techniques which measure the potential and current signals of a corrosion system. The Tafel and Stern-Geary equations, which are widely applied in corrosion research, are derived from the Butler-Volmer equation.

### 1.3.1.3 Tafel equations

Amongst the most important derivations of the Butler-Volmer equation are the Tafel equations [34]. When a large magnitude of anodic or cathodic overpotential ( $\eta$ ) is applied to an electrode, the Butler-Volmer equation can be simplified mathematically as shown in equation (15) and (16), respectively, for each scenario.

$$i = i_0 \exp\left(\frac{(1-\alpha)ZF\eta}{RT}\right) \quad (15)$$

$$i = i_0 \exp\left(-\frac{\alpha ZF\eta}{RT}\right) \quad (16)$$

Rewriting equations (15) and (16) gives:

$$\eta = b_a \log\left(\frac{i}{i_0}\right) \quad (17)$$

$$\eta = -b_c \log\left(\frac{i}{i_0}\right) \quad (18)$$

Where:

$$b_a = \frac{2.303RT}{(1-\alpha)ZF}$$

and:

$$b_c = \frac{2.303RT}{\alpha ZF}$$

Equations (17) and (18) are called Tafel equations for the anodic reaction and cathodic reaction, respectively. The parameters  $b_a$  and  $b_c$  are called Tafel slopes due to the linear relationship between the overpotential and the logarithm of the current density. These two equations provide a theoretical basis for the potentiodynamic polarization technique, which is widely used for evaluating Tafel slopes.

#### 1.3.1.4 Stern-Geary equation

Another derivation of the Butler-Volmer equation that is extensively applied in corrosion monitoring techniques is the Stern-Geary equation. Rewriting of equation (14) of a corrosion system gives:

$$i = i_{\text{corr}} \left[ \exp\left(\frac{\eta}{\beta_a}\right) - \exp\left(-\frac{\eta}{\beta_c}\right) \right] \quad (19)$$

Where:

$$\beta_a = \frac{RT}{(1-\alpha)ZF}$$

and:

$$\beta_c = \frac{RT}{\alpha ZF}$$

Mathematically, the exponential terms can be expanded in a power series, *i.e.*,  $e^x = 1+x + x^2/2 + x^3/6 + \dots$ . If  $x$  is small enough, then  $e^x$  is approximately equal to  $1+x$ . Hence, if a small overpotential is applied to the corrosion system, the exponential terms  $\exp\left(\frac{\eta}{\beta_a}\right)$  and  $\exp\left(-\frac{\eta}{\beta_c}\right)$  in equation (19) can be simplified as  $1 + \frac{\eta}{\beta_a}$  and  $1 + \left(-\frac{\eta}{\beta_c}\right)$ , respectively. Then, equation (19) can be rewritten as:

$$i = i_{\text{corr}} \frac{(\beta_a + \beta_c)}{\beta_a \beta_c} \eta \quad (20)$$

Note that:

$$b_a = \frac{2.303RT}{(1-\alpha)ZF}, b_c = \frac{2.303RT}{\alpha ZF}$$

and:

$$\beta_a = \frac{RT}{(1-\alpha)ZF}, \beta_c = \frac{RT}{\alpha ZF}.$$

Therefore:

$$\beta_a = \frac{b_a}{\ln 10} \text{ and } \beta_c = \frac{b_c}{\ln 10}.$$

Thus, equation (20) can be rearranged as:

$$i = i_{\text{corr}} \frac{2.303(b_a + b_c)}{b_a b_c} \eta \quad (21)$$

A linear relationship between the overpotential and the current density at small values of overpotentials is obtained in equation (21). By rewriting this equation, the corrosion current at equilibrium,  $i_{\text{corr}}$ , can be determined by:

$$i_{\text{corr}} = \frac{b_a b_c}{2.303(b_a + b_c)} \cdot \frac{1}{R_p} \quad (22)$$

This equation is called the Stern-Geary equation.  $R_p$  is the polarization resistance, which is defined as  $R_p = \frac{\Delta \eta}{\Delta i} |_{\eta=0}$  [35]. It can be obtained by measuring the slope of the current density-potential curve. Once the  $R_p$  is determined, the  $i_{\text{corr}}$  can be calculated based on this equation with known Tafel slopes. The Stern-Geary equation provides a method to calculate the corrosion current, and hence the corrosion rate, by measuring the polarization resistance. Consequently, an important application of this equation in electrochemical measurement is the linear polarization resistance technique.

### 1.3.2 Electrochemical Techniques for Corrosion Study

#### 1.3.2.1 Potentiodynamic polarization

Potentiodynamic polarization techniques can be used to determine the Tafel slopes, corrosion current and corrosion rate. This technique is based on the Tafel equations that there is a linear relationship between the potential and the logarithm of the current density at large values of overpotentials, which is shown in equations (17) and (18) in the previous section. Experimentally, the measurement is conducted by polarizing the electrode with a wide potential range *versus* corrosion potential, and monitoring the current response. The Tafel slopes can be obtained by measuring the slopes of polarization curves at high overpotentials. Corrosion current can be obtained from the intersection of the extrapolated Tafel slopes at original corrosion potential [36]. The determination of corrosion current and Tafel slopes are illustrated in Figure 1.

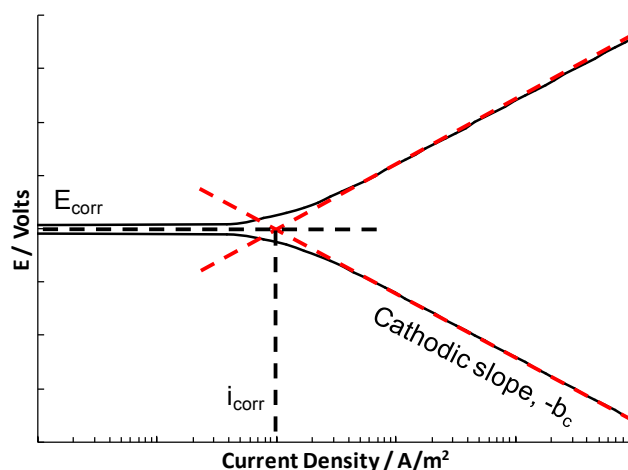


Figure 1. Illustration of corrosion current and Tafel slopes determination by polarization curves.

The main advantage of this technique is the experimental determination of the Tafel slopes as well as the corrosion current. Potentiodynamic polarization also provides mechanistic information of the corrosion process such as limiting current and passivation region within the corrosion system by analysis of the polarization curves.

Although potentiodynamic polarization has many advantages, there are some obvious disadvantages. Since this technique needs to scan the electrode with a wide potential range, the measurement is usually time-consuming. By applying a large value of overpotential, the studied electrode surface is dramatically changed as well. Thus, this technique itself it is not useful for continuous corrosion monitoring.

#### *1.3.2.2 Linear polarization resistance*

The linear polarization resistance (LPR) technique is widely used for instantaneous determination of corrosion rates in laboratory experiments and industrial applications. From the Stern-Geary equation, a linear relationship between small overpotential and current density is obtained. The polarization resistance is defined as  $R_p = \frac{\Delta\eta}{\Delta i} |_{\eta=0}$ , assuming that Ohm's law is applicable in this corrosion system. Experimentally, the measurement is conducted by polarizing the electrode with a small overpotential (usually less than 20 mV), and monitoring the current response. The polarization resistance can be obtained by measuring the slopes of the polarization curve at corrosion potential ( $E_{\text{corr}}$ ). The corrosion current can be calculated by the Stern-Geary equation, given that the Tafel slopes  $b_a$ ,  $b_c$  are known.

Because the small overpotential scan range significantly reduces the measurement duration, the most valuable benefit of LPR is to instantaneously determine the corrosion

rate. In addition, LPR is a non-destructive technique due to the small applied potential perturbation, which only has a negligible influence on the studied electrode surface. Because of these advantages, linear polarization is highly suitable for continuous corrosion monitoring.

On the other hand, linear polarization measurement only provides polarization resistance information. No mechanistic information can be obtained from this technique. Besides, in order to calculate the corrosion rate, the Tafel slopes need to be predetermined. Last but not least, the linear polarization technique assumes that polarization resistance is solely the full ohmic resistance of the electrode. However, in reality, the measured polarization resistance may contain other ohmic or non-ohmic resistances from the electrolyte, corrosion product layer, *etc.*, which may influence the validity of the measurement. Callow, *et al.*, thoroughly examined the factors leading to errors in LPR measurements such as “appreciable IR drops” and “electrode perturbation” [37].

#### *1.3.2.3 Electrochemical frequency modulation*

Harmonic analysis (HA) and its derivative, electrochemical frequency modulation (EFM), have been reportedly successfully used for corrosion rate and Tafel slopes determination [38-41]. The detailed mathematical description of the EFM technique can be found in Bosch *et al.*'s paper [40] (see Appendix). Traditional electrochemical techniques such as linear polarization resistance (LPR) and electrochemical impedance spectroscopy (EIS) are widely used for estimating the corrosion rate. LPR is a fast, non-destructive technique since a very small overpotential is applied to the corrosion system.

EIS can provide mechanistic information for the system and associated corrosion rate, it is also non-destructive due to the small overpotential applied. However, the EIS technique can be time consuming; it can take hours to complete a measurement. In addition, in order to calculate the corrosion rate, the anodic and cathodic Tafel slopes, termed  $b_a$  and  $b_c$ , respectively, need to be determined for both of these techniques. Tafel slopes can be obtained from potentiodynamic polarization measurements at high overpotentials. However, this technique can be time consuming and often impractical as the applied high overpotentials can significantly change the characteristics of the electrode surface.

EFM provides the same advantages as LPR. It is fast and non-destructive. But in addition, the Tafel slopes are determined. This means that mechanistic changes can be detected by monitoring change in the anodic and/or cathodic Tafel slopes with EFM, which is unavailable with the LPR or EIS techniques.

#### *1.3.2.4 Other electrochemical techniques in corrosion study*

Besides the techniques introduced here, many more electrochemical techniques have been employed in recent corrosion studies. Electrochemical impedance spectroscopy (EIS) can provide “wealth mechanistic and kinetic information” of the studied electrochemical system [28]. It is widely used in evaluation of inhibitor performance, coatings performance and metal passivation in corrosion system. Electrochemical quartz-crystal microbalance (EQCM) is a useful tool for investigating metal film deposition and dissolution [42]. All these techniques investigate specific

electrochemical aspects of corrosion processes, and help us understand the electrochemical nature of corrosion phenomena.

## CHAPTER 2: RESEARCH OBJECTIVES

Based on the information presented in Chapter 1, it can be seen that CO<sub>2</sub> corrosion under scaling condition is not fully understood. Investigation of the effect of FeCO<sub>3</sub> layer on CO<sub>2</sub> corrosion may be critical for understanding the mechanism of corrosion layer protection and the initiation of localized CO<sub>2</sub> corrosion. Han previously reported a phenomenon that corrosion rate decreases concurrently with an increase in open circuit potential under scaling condition at elevated pH and temperature[43]. They proposed a hypothesis of pseudo-passivation mechanism to describe this phenomenon where the actively corroded steel surface becomes passivated due to the presence of Fe<sub>3</sub>O<sub>4</sub> in the FeCO<sub>3</sub> layer [24]. Understanding this phenomenon is important because a partial degradation of the passivated surface is expected to develop a galvanic cell and initiate localized corrosion.

Among factors that affect the formation of such a pseudo-passive layer, pH is most critical due to the fact that the FeCO<sub>3</sub> precipitation process can be significantly retarded or reversed by lowering the pH due to the resultant smaller FeCO<sub>3</sub> saturation value from such a perturbation. Few tests of this pseudo-passive layer at a lower pH range, conditions that are more commonly observed in upstream pipelines for the oil and gas industry, have been conducted.

Validation of the findings at high pH and expansion of this pseudo-passivation research to cover a wider pH range could be important for understanding CO<sub>2</sub> corrosion under scaling conditions. Consequently, the main objective of this work is to investigate the formation of pseudo-passive layer with electrochemical techniques, characterize this

layer with surface analysis methods and propose a mechanism for this pseudo-passive phenomenon over a wide pH range.

## CHAPTER 3: EVALUATION OF THE ELECTROCHEMICAL FREQUENCY MODULATION TECHNIQUE IN CO<sub>2</sub> CORROSION SYSTEMS

### 3.1 Introduction

It has been introduced in section 1.3.2.3 that EFM is fast and non-destructive technique featuring instant corrosion rate and Tafel slopes determination. With this advantage, EFM is an ideal method to investigate corrosion systems with any mechanistic changes. In the study of pseudo-passive layer formation, a mechanistic change can be assumed to occur when the layer forms. Hence, EFM technique could be used in this system to detect any transition. Due to the potential advantages of EFM in research specific to pseudo-passive layer formation, a study evaluating the EFM technique in CO<sub>2</sub> corrosion systems has been conducted.

### 3.2 Experimental

#### *3.2.1 Experimental Setup and Instrumentation*

The experiments were conducted in a 2 L glass cell, using a three electrode system. This system was used for conducting all electrochemical tests. The experimental setup is plotted in Figure 2. The reference electrode was Ag/AgCl (saturated KCl was used as filling solution), a semi-circular shaped platinum wire was used as counter electrode, and the working electrode was a cylindrical X-65 carbon steel sample with a 5.4 cm<sup>2</sup> surface area. Pictures of the working electrode and chemical composition of the X-65 carbon steel are presented in Figure 3 and Table 2, respectively.

A Gamry Reference 600 Potentiostat/Galvanostat/ZRA was used for conducting electrochemical measurements such as electrochemical impedance spectroscopy (EIS), electrochemical frequency modulation (EFM) and potentiodynamic polarization (PP). The weight loss (WL) technique was also used to measure the corrosion rate.

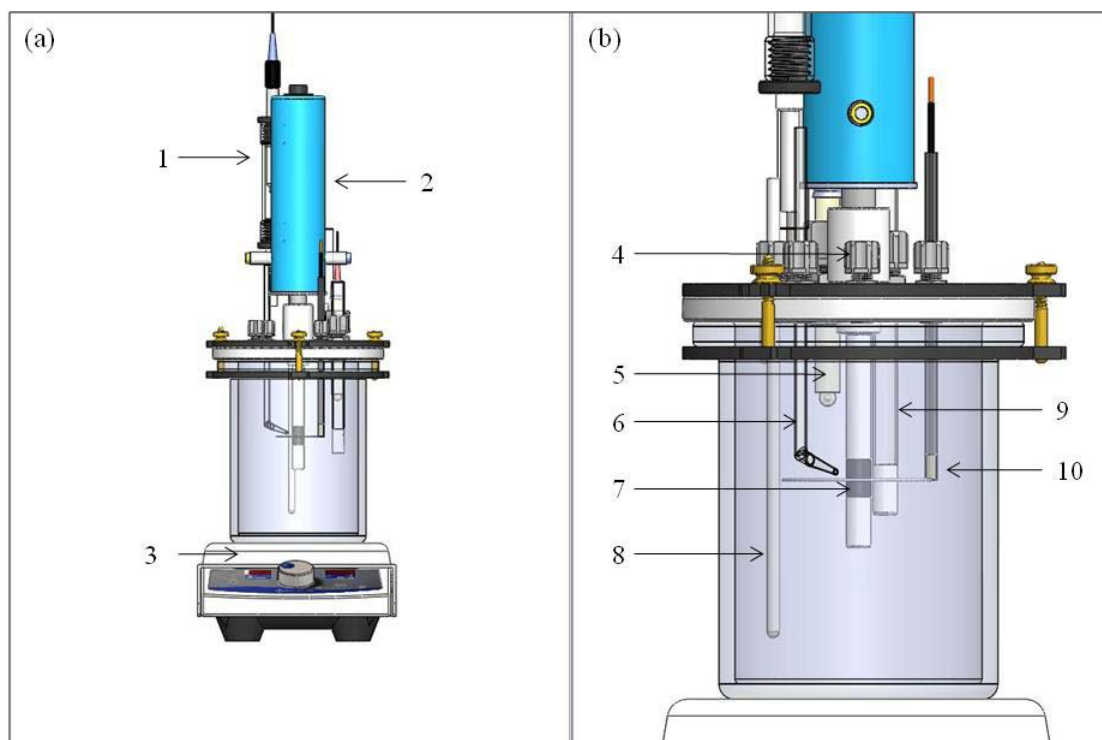


Figure 2. Schematic of glass cell setup: (a) front view and (b) side view. (Courtesy of Cody Shafer, research engineer, ICMT, Ohio University)

- |                                |                      |                     |
|--------------------------------|----------------------|---------------------|
| 1. Reference electrode         | 2. Rotator motor     | 3. Hot plate        |
| 4. Gas outlet                  | 5. pH probe          | 6. Luggin capillary |
| 7. Rotating cylinder electrode | 8. Temperature probe | 9. Gas inlet tubing |
| 10. Counter electrode          |                      |                     |

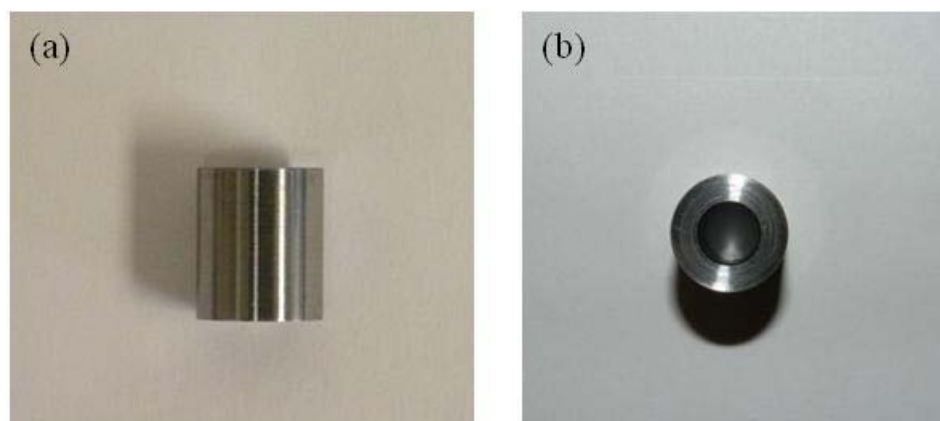


Figure 3. Images of the cylindrical X-65 carbon steel sample: (a) side view and (b) top view.  
(Outer diameter: 12mm; length: 14.4mm)

Table 2. Chemical composition of X-65 carbon steel (wt.%) [44]

<b>Al</b>	<b>As</b>	<b>B</b>	<b>C</b>	<b>Ca</b>	<b>Co</b>	<b>Cr</b>	<b>Mn</b>
0.032	0.008	0.001	0.13	0.002	0.007	0.14	1.16
<b>Mo</b>	<b>Nb</b>	<b>Ni</b>	<b>P</b>	<b>S</b>	<b>Sb</b>	<b>Si</b>	<b>Sn</b>
0.16	0.017	0.36	0.009	0.009	0.009	0.26	0.007
<b>V</b>	<b>Cu</b>	<b>Fe</b>					
0.047	0.131	balance					

### 3.2.2 Test Matrix

For the study of the EFM technique, four test systems were investigated.

Application of EFM at 5°C, 25°C and two inhibition systems at 25°C were studied. The test matrix is listed (Table 3). For inhibition systems, the active chemical compositions of tested inhibitors are listed in Table 4.

Table 3. Test matrix for evaluation of EFM technique in CO<sub>2</sub> corrosion systems

	<b>System 1</b>	<b>System 2</b>	<b>System 3</b>	<b>System 4</b>
Carbon steel type	X-65	X-65	X-65	X-65
Temperature (°C)	5	25	25	25
pH	6.0	4.0	4.0	4.0
Electrolyte	3 wt% NaCl	3 wt% NaCl	3 wt% NaCl	3 wt% NaCl
CO <sub>2</sub> partial pressure (bar)	1	1	1	1
Flow velocity (rpm)	1000	1000	1000	1000
Inhibitor name	--	--	K2	K1
Inhibitor concentration	0	0	1041 ppm, 208 ppm	50 ppm
Experimental techniques	EFM, EIS, PP, WL	EFM, EIS, PP, WL	EFM, EIS, PP	EFM, EIS, PP

Table 4. Active chemical components of K1 and K2 inhibitors

Inhibitor product name	Active chemical components (wt.%)
K1	24% TOFA/EDTA imidazolium
K2	24% C <sub>12</sub> -C <sub>16</sub> coco quaternary ammonium

### 3.2.3 Procedure

3 wt.% NaCl electrolyte was prepared in the glass cell and purged with continuous CO<sub>2</sub> gas flow in order to deaerate the electrolyte and maintain test environment. The temperature was adjusted to the required level by a hot plate with temperature control function. For experiments at 5°C, the glass cell setup was placed in a refrigerator in order to achieve the desired temperature. When the electrolyte was deaerated and saturated (typically 1 to 2 hours), the pH was adjusted to the desired level by addition of buffer reagent such as solid/aqueous of NaHCO<sub>3</sub>, Na<sub>2</sub>CO<sub>3</sub>, NaOH or HCl solution, the latter two having an indirect effect on speciation within the test system. The working electrode (X-65 carbon steel sample) surface was then polished by 400 and 600 grit silicon carbide paper sequentially. During the polishing process, the sample was flushed with isopropanol which served as a coolant and lubricant. After having been polished, the sample was immersed into a beaker with isopropanol and placed in an ultrasonic bath to remove the polishing debris. Finally, the sample was taken out and completely dried by cool air from a blow dryer. It was then immediately mounted on the shaft of the rotating cylinder and immersed into the prepared electrolyte in the glass cell.

Electrochemical measurements were conducted once the system was connected to the computer controlled potentiostat. For weight loss measurements, samples were taken out of the test solution approximately 24 hours after the test began. For tests in a corrosion inhibition system, inhibitors were added into the glass cell sequentially during the test while the electrochemical measurements were being conducted.

### 3.2.4 Parameter Selections of Electrochemical Measurements

The main parameters of electrochemical measurements selected are listed in Table 5 below.

Table 5. Parameter selections of electrochemical measurements

<b>Technique</b>	<b>Parameters</b>
<i>EIS</i>	Initial Frequency: 10000 Hz, Final Frequency: 0.01 Hz. Points per Decade: 5. AC Voltage: 5 mV. DC Voltage: 0 vs. EOC.
<i>Potentiodynamic Polarization</i>	Scan Rate: 0.1667 mV / s. Sample Period: 2s. Anodic overvoltage: 0 ~ 0.2 V (vs. EOC). Cathodic overvoltage: 0 ~ -0.4V (vs. EOC).
<i>EFM</i>	Base Frequency: 0.1Hz. Amplitude: 10 mV. Multiplier A and Multiplier B: 2, 5. I/E Range Mode: Auto. DC Voltage: 0 V vs. EOC. Number of Cycles: 16 or 32. Max Current: 0.1 – 1.0 mA. Corrosion Type: Activation / Diffusion.

### 3.3 Results and Discussion

#### 3.3.1 System 1 (5°C baseline)

EIS, EFM, potentiodynamic polarization and weight loss measurements were conducted in a 5°C baseline system. Carbon steel reportedly has a distinct Tafel behavior at this test condition [45]. Hence, it is a suitable test condition for evaluating the applicability of the EFM technique in this corrosion system by comparing the results of these techniques. Tafel slopes and corrosion current density ( $i_{\text{corr}}$ ) calculated from EFM and potentiodynamic polarization measurements were compared. Charge transfer resistance  $R_{\text{ct}}$  from EFM and EIS measurements were compared as well.  $I_{\text{corr}}$  calculated from EFM was also compared with the average corrosion current density calculated from weight loss measurement based on equation (13). The complete comparison of these techniques is shown in Table 6. From this table, it can be seen that the charge transfer resistances from EFM and EIS have a reasonable agreement. The EFM technique can calculate the corrosion rate and Tafel slopes using any one of its three models: activation, diffusion and passivation model. The cathodic slope of the potentiodynamic polarization curve (Figure 4) indicates the cathodic reaction is under mixed control in this system. Hence, the corrosion rate can be calculated using either the activation or diffusion model of EFM. It is also expected that the actual corrosion rate should be between those values calculated by the activation and diffusion model of EFM. As shown in Table 6, the corrosion rate calculated by potentiodynamic polarization is 0.36 mm/y while the corrosion rates calculated by the activation and diffusion models of EFM is 0.20 and 0.53 mm/y, respectively. These results are in accord with the potentiodynamic polarization

measurements that the reaction is under mixed control. It can be concluded that actual corrosion rate is between 0.2 and 0.5 mm/y calculated from activation and diffusion models of EFM. The weight loss result also verifies this conclusion at corrosion rate of 0.46 mm/y. EFM provides useful corrosion information even in a complicated system that is under mixed control.

Table 6. Result comparisons of experimental techniques. 5°C, pH 6.0, 3 wt.% NaCl, 1 bar CO<sub>2</sub>, rotating speed 1000rpm, X-65 carbon steel, 1 day test.

Techniques	R <sub>ct</sub> ohm	CR mm/y	i <sub>corr</sub> A/m <sup>2</sup>	b <sub>a</sub> mV/decade	b <sub>c</sub> mV/decade
EFM (activation model)	102.8	0.20	0.18	33.0	75.0
EFM (diffusion model)	101.7	0.53	0.46	58.8	infinity
PP		0.36	0.31	57.4	235.3
EIS	90.0				
Weight loss		0.45	0.39		

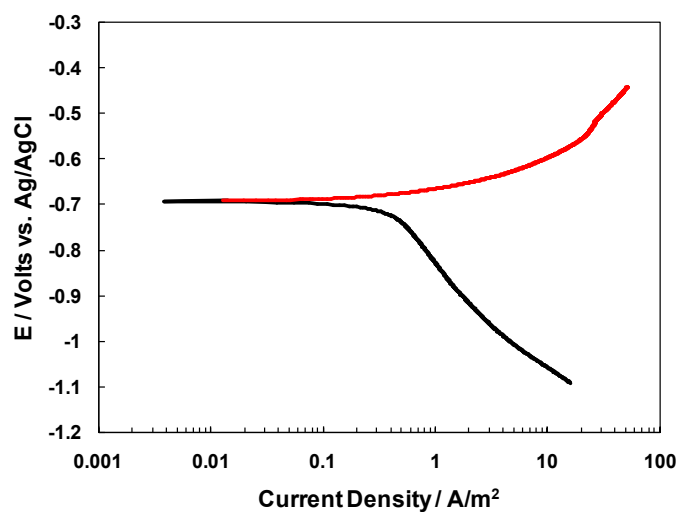


Figure 4. Potentiodynamic polarization curves. 5°C, pH 6.0, 3 wt.% NaCl, 1 bar CO<sub>2</sub>, rotating speed 1000rpm, X-65 carbon steel.

### 3.3.2 System 2 (25°C baseline)

The EFM technique was also evaluated for a 25°C baseline system by comparing obtained results with those from other corrosion techniques. Results from different techniques were compared (Table 7). It can be seen that the charge transfer resistance obtained from EFM and EIS measurements are virtually identical. The cathodic slope from potentiodynamic polarization shows that the cathodic reaction is also under mixed control (Figure 5), which means that the cathodic reaction is not solely controlled by a charge transfer step or mass transfer step. Both mechanisms control the corrosion process in this system. Therefore the actual corrosion rate should be in the range of corrosion rates calculated using the single activation and diffusion control EFM models. As shown in Table 7, the EFM measurements give a corrosion rate between 2.6 and 3.8 mm/y, respectively, for the activation and diffusion control models. The weight loss result of 2.9 mm/y is in a reasonable agreement with these measurements. In this system, the EFM provides reasonable information of the corrosion system compared to other widely used corrosion techniques.

Table 7. Result comparisons of experimental techniques. 25°C, pH 4.0, 3 wt.% NaCl, 1 bar CO<sub>2</sub>, rotating speed 1000rpm, X-65 carbon steel, 1 day test.

Techniques	R <sub>ct</sub> ohm	CR mm/y	i <sub>corr</sub> A/m <sup>2</sup>	b <sub>a</sub> mV/decade	b <sub>c</sub> mV/decade
EFM (activation model)	22.8	2.65	2.29	76.0	428.7
(diffusion model)	22.7	3.80	3.27	92.5	infinity
PP		2.72	2.34	93.4	1072.0
EIS	21.5				
Weight loss		2.95	2.54		

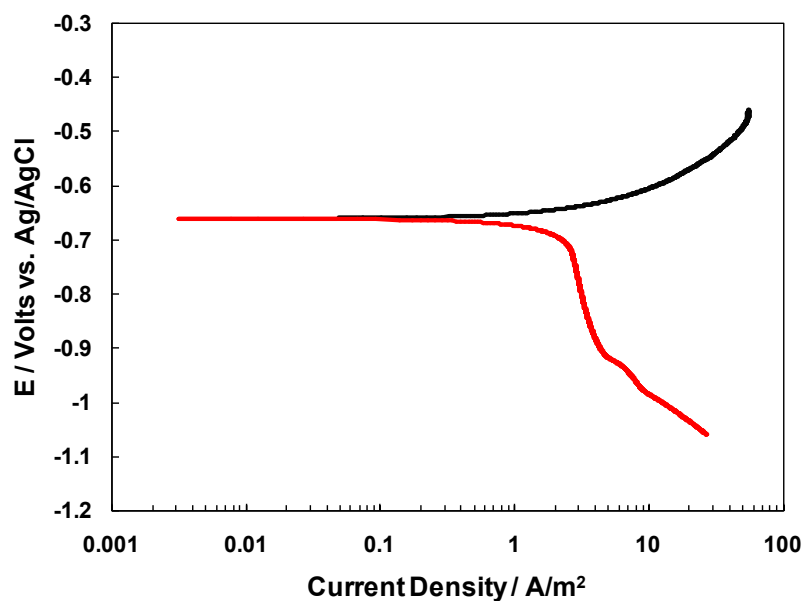


Figure 5. Potentiodynamic polarization curves. 25°C, pH 4.0, 3 wt.% NaCl, 1 bar CO<sub>2</sub>, rotating speed 1000rpm, X-65 carbon steel.

### 3.3.3 System 3 (K2 inhibitor system)

Tests at 25°C in presence of K2 inhibitor (24% Coco quaternary ammonium) were conducted. The carbon steel specimen was pre-corroded for one hour in the glass cell and then the inhibitor was added. EFM was utilized to monitor the corrosion behaviors of the system with time.

#### 3.3.3.1 Single addition of K2 inhibitor result

In this set of tests, 1041ppm K2 inhibitor was injected into the glass cell with a single addition one hour after the working electrode was placed in the system. The corrosion information of the system such as corrosion rate,  $R_{ct}$  value and Tafel slopes were monitored by EFM after the addition of inhibitor. In Figure 6, the corrosion rate decreases from 2.7 mm/y to 1.3 mm/y within 3 hours after an addition of inhibitor. The increase of charge transfer resistance of the sample (Figure 7) also indicates a change of the system. The changes of Tafel slopes were recorded as well (Figure 8 and Figure 9). The anodic reaction is not significantly affected by the inhibitor addition. However, the cathodic slope changes dramatically, from over 500 mV/decade to approximately 200 mV/decade. This change of cathodic slope may indicate that the mechanism of the cathodic reaction has changed. One possible explanation is that the cathodic reaction changed from mixed control to charge transfer control. B value was calculated based on Tafel slope values. From Figure 10, it can be seen that the B value has a noticeable change from 36 to 26 mV. The EFM also introduces causality factors to corroborate the reliability of EFM measurements. According to the principle of the EFM technique [40], the theoretical values of causality factors should be 2 and 3, respectively. The

experimental data can be checked by comparing the experimental values of causality factors to those theoretical values. The causality factors *versus* time are shown in Figure 11. Their values are close to the theoretical values of 2 and 3 throughout the test; this means the collected data is satisfactory.

In this test, EFM was able to respond to the change of the system due to addition of inhibitor by means of recording changes of corrosion information such as Tafel slopes and corrosion rates.

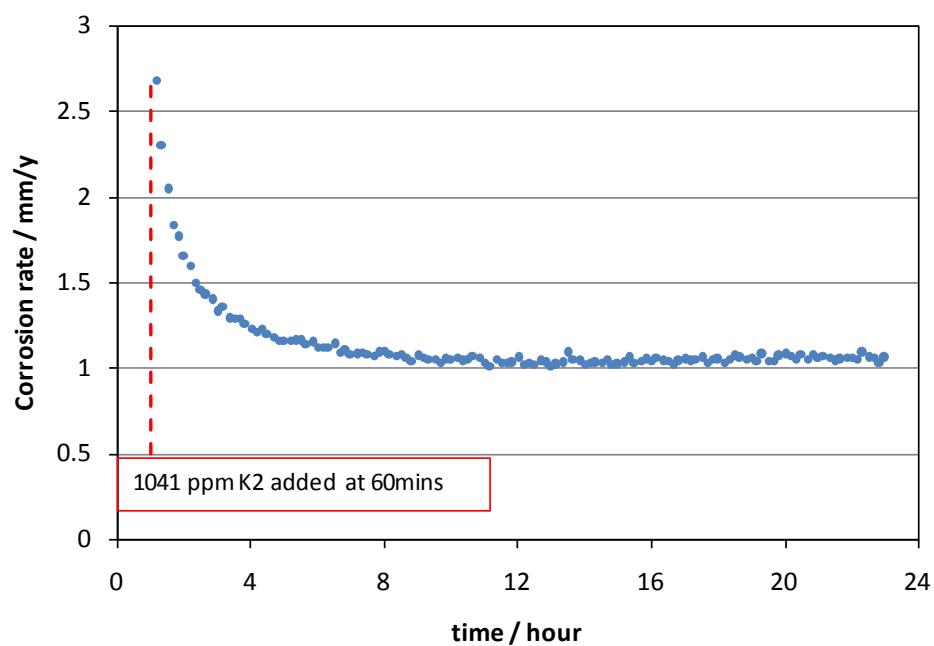


Figure 6. EFM result: corrosion rate vs. elapsed time. 3 wt. % NaCl, 25°C, 1 bar CO<sub>2</sub>, pH 4.0, X-65 carbon steel, electrode rotating speed 1000 rpm, 1041ppm K2 inhibitor.

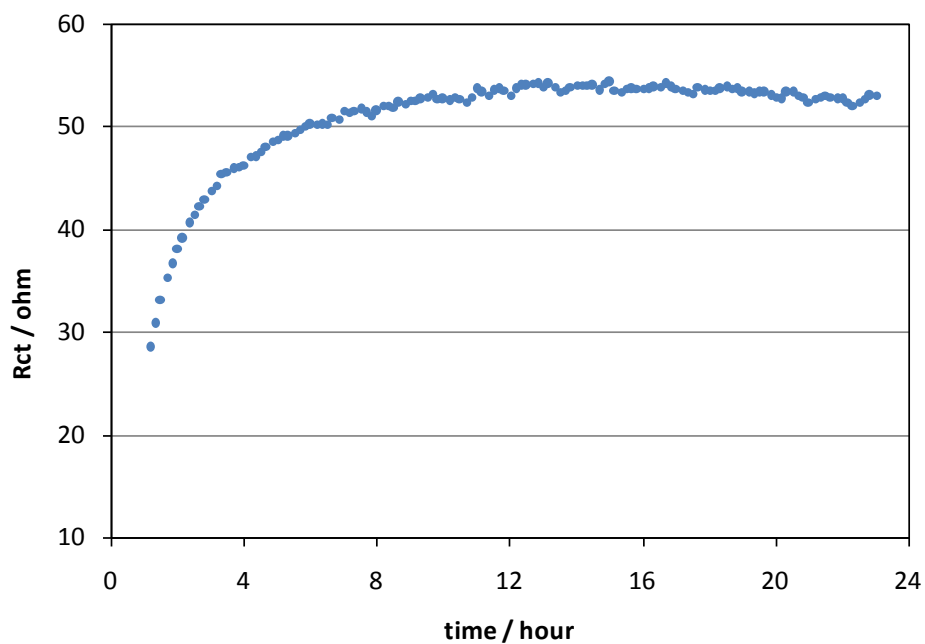


Figure 7. EFM result:  $R_{ct}$  vs. elapsed time. 3 wt. % NaCl, 25°C, 1 bar CO<sub>2</sub>, pH 4.0, X-65 carbon steel, electrode rotating speed 1000 rpm, 1041ppm K2 inhibitor.

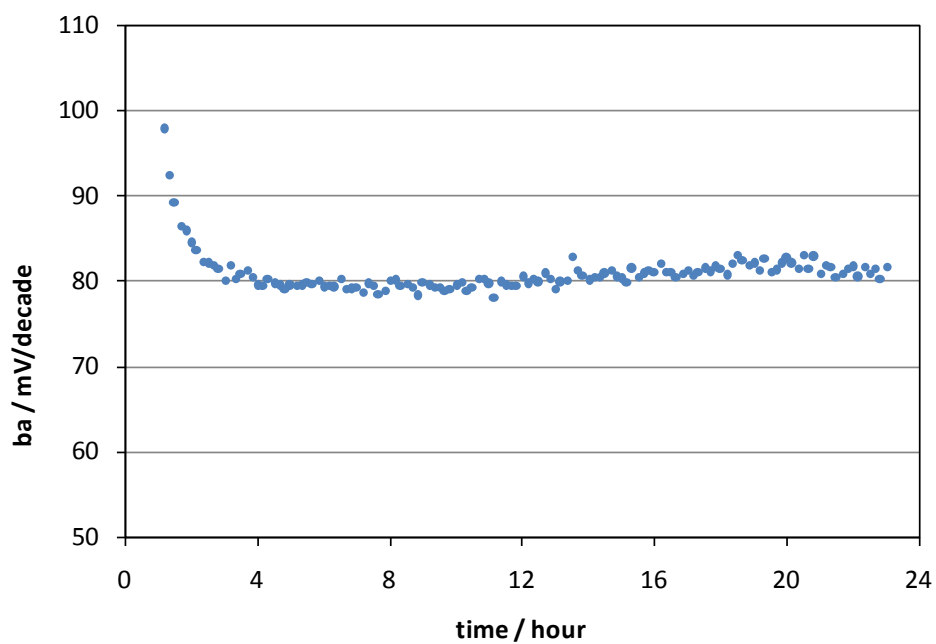


Figure 8. EFM result: anodic slope vs. elapsed time. 3 wt. % NaCl, 25°C, 1 bar CO<sub>2</sub>, pH 4.0, X-65 carbon steel, electrode rotating speed 1000 rpm, 1041ppm K2 inhibitor.

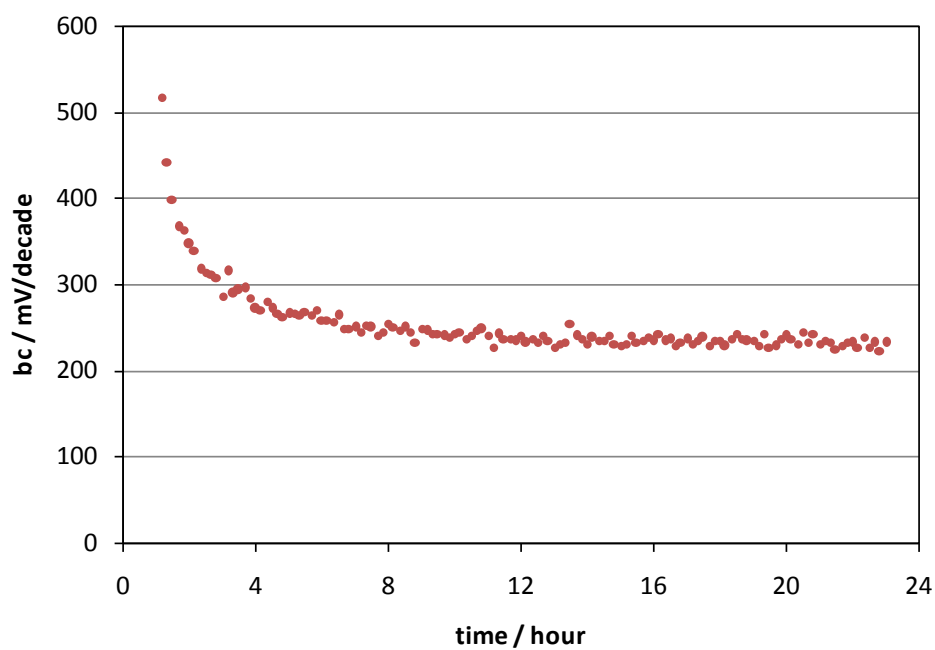


Figure 9. EFM result: cathodic slope vs. elapsed time. 3 wt. % NaCl, 25°C, 1 bar CO<sub>2</sub>, pH 4.0, X-65 carbon steel, electrode rotating speed 1000 rpm, 1041ppm K2 inhibitor.

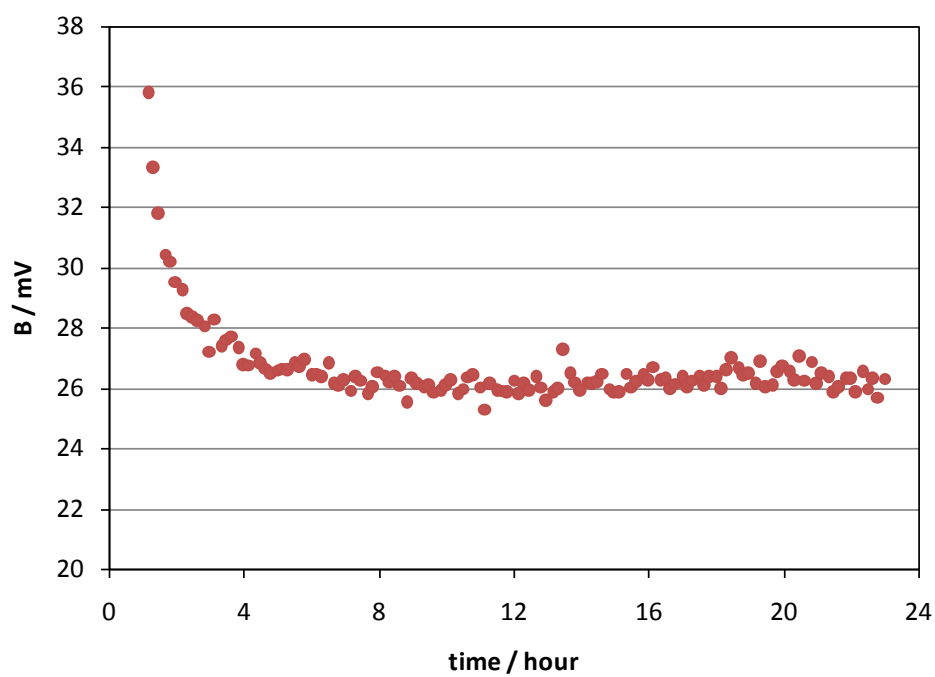


Figure 10. EFM result: B value vs. elapsed time. 3 wt. % NaCl, 25°C, 1 bar CO<sub>2</sub>, pH 4.0, X-65 carbon steel, electrode rotating speed 1000 rpm, 1041ppm K2 inhibitor.

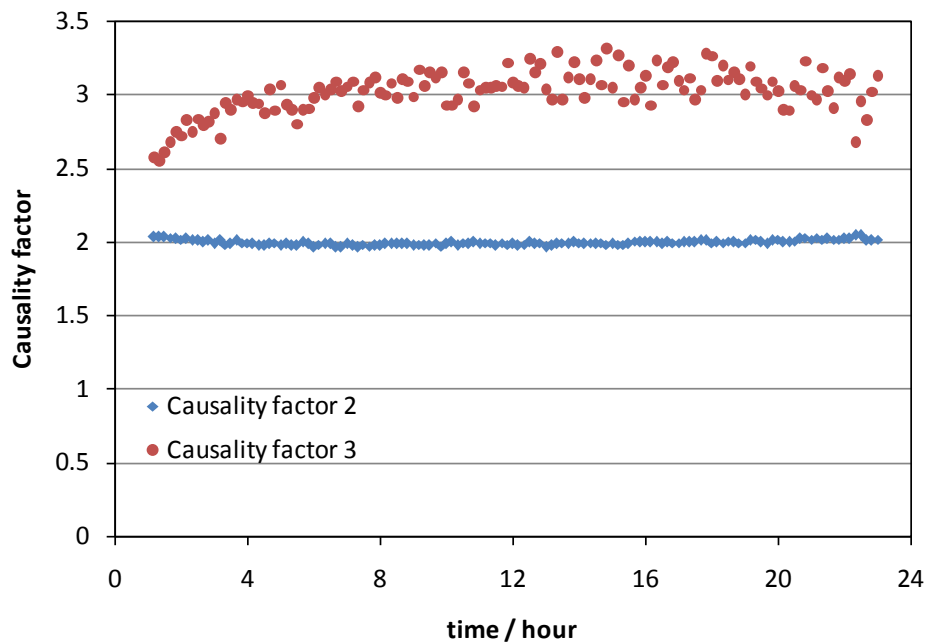


Figure 11. Causality factors *vs.* elapsed time. 3 wt. % NaCl, 25°C, 1 bar CO<sub>2</sub>, pH 4.0, X-65 carbon steel, electrode rotating speed 1000 rpm, 1041ppm K2 inhibitor.

### 3.3.3.2 Sequential addition of K2 inhibitor result

In this test, K2 inhibitor (24% Coco quaternary ammonium) was added sequentially using four additions to increase the concentration from 42 ppm to 208 ppm. It should be noted that the actual concentration of active inhibition chemicals in this test increased from 10 ppm to 50 ppm with respect to the Coco quaternary ammonium. The first addition of inhibitor was 100 minutes after the working electrode was placed in the system. The interval between each addition of inhibitor was approximately 3 hours. The corrosion rate,  $R_{ct}$  value, Tafel slope changes were recorded by EFM in the test. EIS measurements were also conducted during the test to compare the  $R_{ct}$  results with EFM. From the plot of corrosion rate *versus* elapsed time (Figure 12), it can be seen that corrosion rate decreases significantly after the additions of inhibitor, from 3.8 mm/y to

1.5 mm/y. Then the corrosion rate is steady at approximately 1 mm/y. In Figure 13 and Figure 14, the changes of anodic and cathodic slopes are shown, respectively. There is no significant change of anodic slope and the slope is stable at 100 mV /decade after the system reaches equilibrium. Note that cathodic slope responds to the addition of inhibitor. The slope changes from over 2000 mV/decade to 200 mV /decade. This dramatic change of slope may suggest that the mechanism of the cathodic reaction shifts from a more diffusion controlled reaction to a more charge transfer controlled process. The calculated B value with time is shown in Figure 15. In Figure 16, the Nyquist plots gained from EIS measurement at different time during the test are shown. The changes in B values and resistance indicate the shift of reaction mechanism in the system. The charge transfer resistance was also calculated according to these EIS results and compared with the EFM technique. The comparison of  $R_{ct}$  of these two techniques is shown in Figure 17. In this plot,  $R_{ct}$  values gained from these two techniques are in agreement with each other. They also have similar trends of resistance increase responding to the inhibitor additions. This indicates that the EFM technique provides reliable data for an inhibitor system and is able to monitor the mechanistic changes of this system.

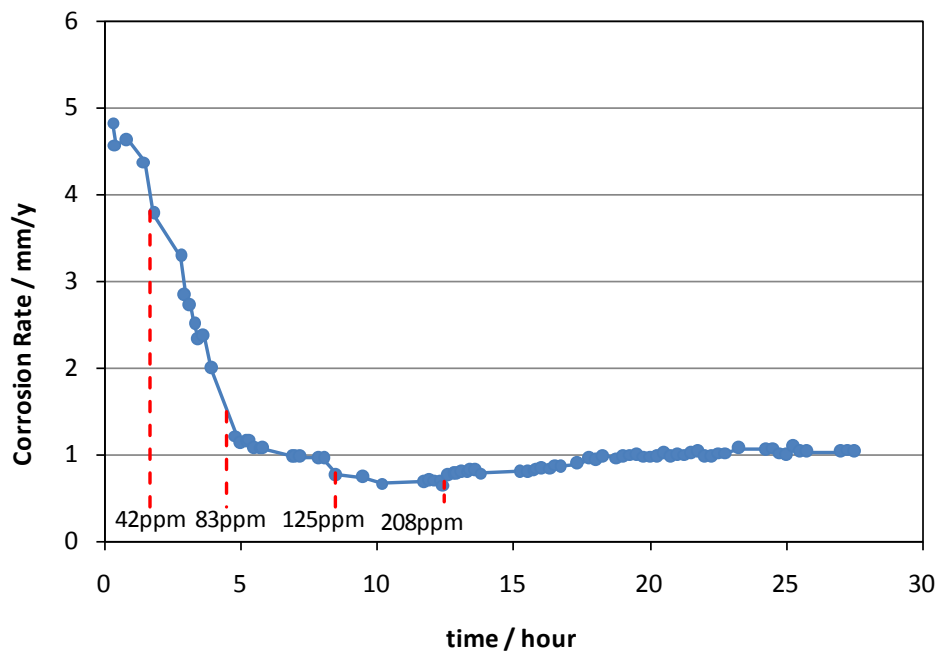


Figure 12. EFM: corrosion rate vs. elapsed time. 3 wt.% NaCl, 25°C, 1 bar CO<sub>2</sub>, pH 4.0, X-65 carbon steel, rotating speed 1000 rpm, sequential addition of K2 inhibitor: 42- 208 ppm.

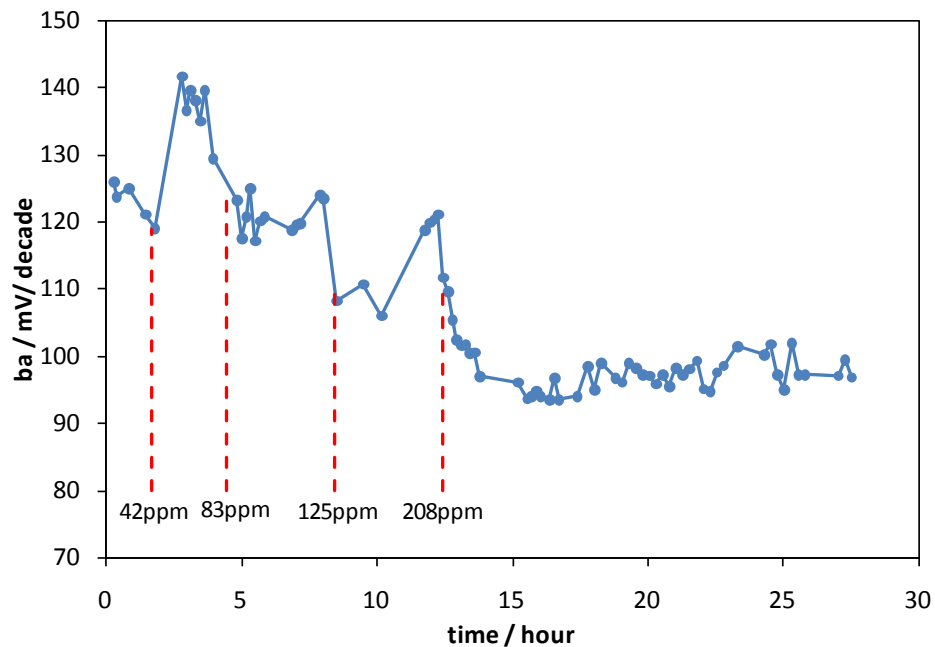


Figure 13. EFM: anodic slope vs. elapsed time. 3 wt.% NaCl, 25°C, 1 bar CO<sub>2</sub>, pH 4.0, X-65 steel, rotating speed 1000 rpm, sequential addition of K2 inhibitor: 42- 208 ppm.

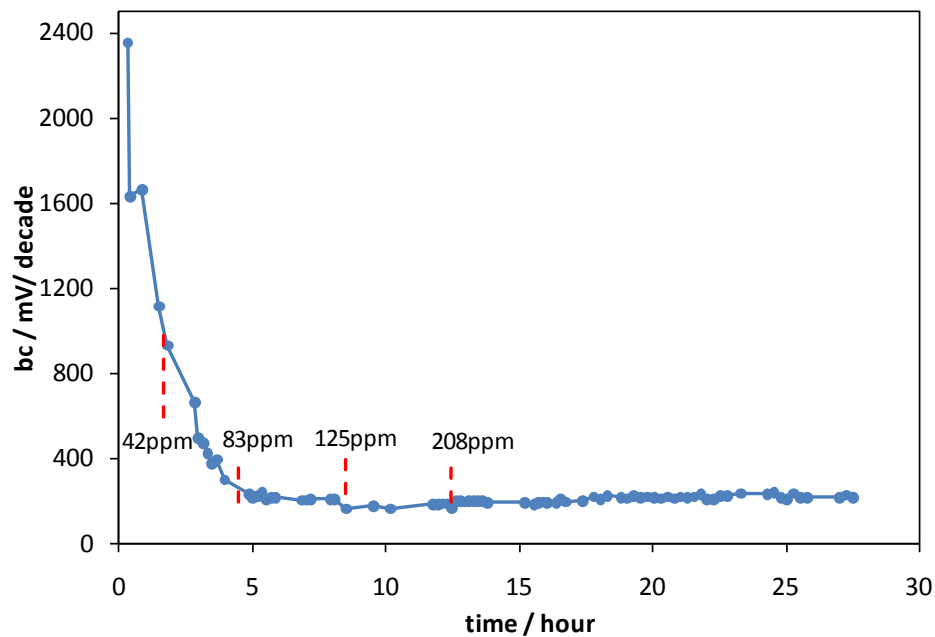


Figure 14. EFM: cathodic slope vs. elapsed time. 3 wt.% NaCl, 25°C, 1 bar CO<sub>2</sub>, pH 4.0, X-65 steel, rotating speed 1000 rpm, sequential addition of K2 inhibitor: 42- 208 ppm.

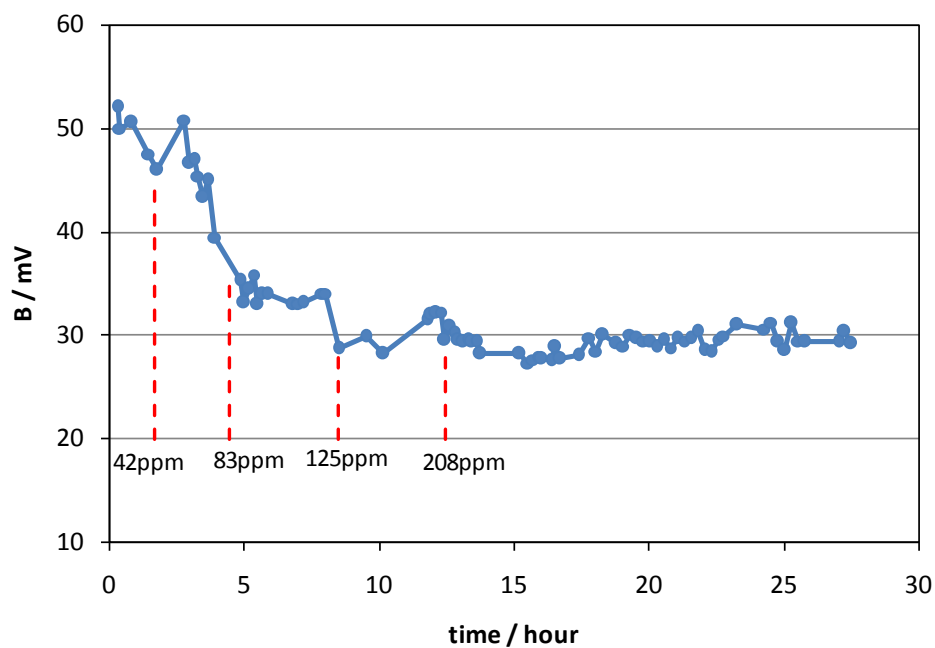


Figure 15. EFM: B value vs. elapsed time. 3 wt.% NaCl, 25°C, 1 bar CO<sub>2</sub>, pH 4.0, X-65 steel, rotating speed 1000 rpm, sequential addition of K2 inhibitor: 42- 208 ppm.

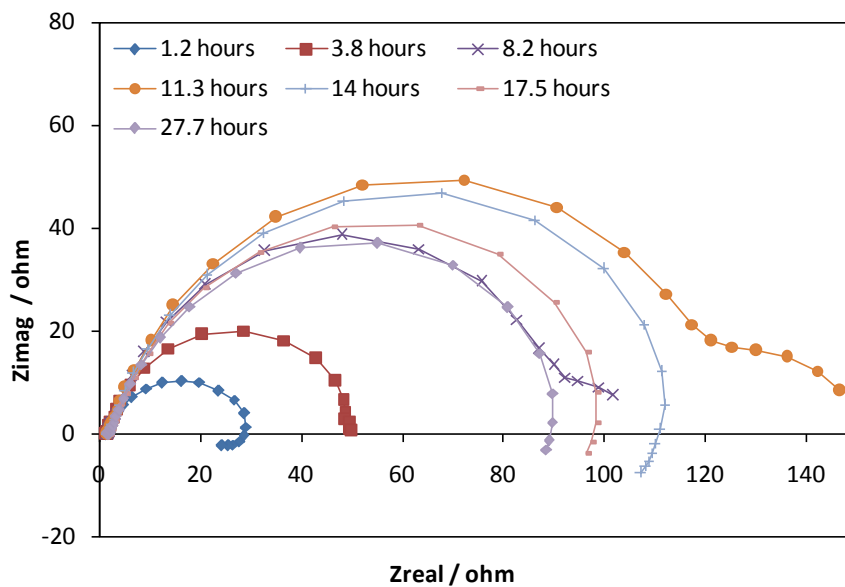


Figure 16. EIS: Nyquist plots at different test time. 3 wt.% NaCl, 25°C, 1 bar CO<sub>2</sub>, pH 4.0, X-65 steel, rotating speed 1000 rpm, sequential addition of K2 inhibitor: 42- 208 ppm.

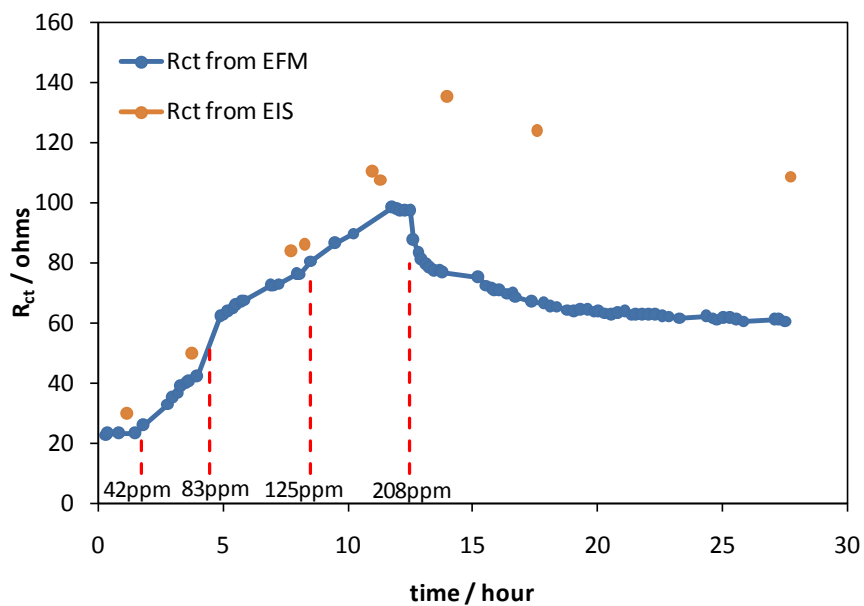


Figure 17. Comparison of  $R_{ct}$  measured by EFM and EIS. 3 wt.% NaCl, 25°C, 1 bar CO<sub>2</sub>, pH 4.0, X-65 steel, rotating speed 1000 rpm, sequential addition of K2 inhibitor: 42- 208 ppm.

### 3.3.4 System 4 (K1 inhibitor system)

Inhibitor test at room temperature of K1 (24%TOFA/DETA imidazolium) was conducted. The steel sample was pre-corroded in the glass cell for approximately 1 hour, and then the inhibitor was added. The inhibitor was added in three increments from 10ppm to 50ppm. The interval between each addition of inhibitor was at least 7 hours in order to maintain equilibrium. EFM and EIS were utilized to monitor the corrosion behavior of the system. The plot of corrosion rate *versus* time monitored by EFM is shown in Figure 18. Corrosion rate decreased from 3.0 mm/y to 0.8 mm/y after the addition of inhibitor K1 within 14 hours. In Figure 19 and Figure 20, the B value and  $R_{ct}$  *versus* elapsed time plots are shown. EFM showed an agreement with EIS in the first 15 hours of the test (Figure 20). After that time, some spurious EFM results were obtained as compared to the simultaneously measured EIS values. After review, these erroneous results may be due to the poor electrical connection of the electrodes to the potentiostat. Because of this observation, EFM was not considered to be able to provide reliable measurements.

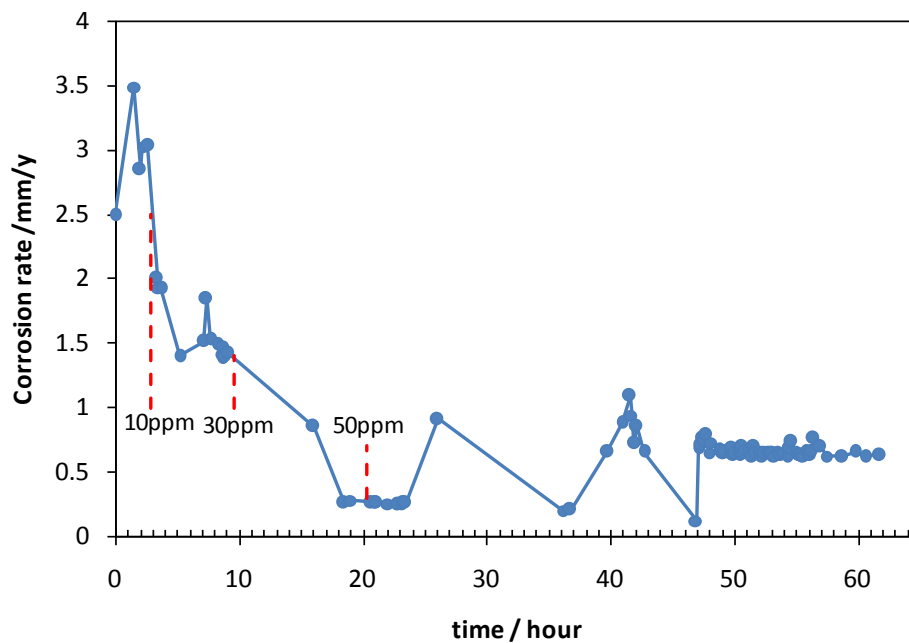


Figure 18. EFM: corrosion rate vs. elapsed time. 3 wt.% NaCl, 25°C, 1 bar CO<sub>2</sub>, pH 4.0, X-65 steel, rotating speed 1000 rpm, sequential addition of K1 inhibitor: 10- 50 ppm.

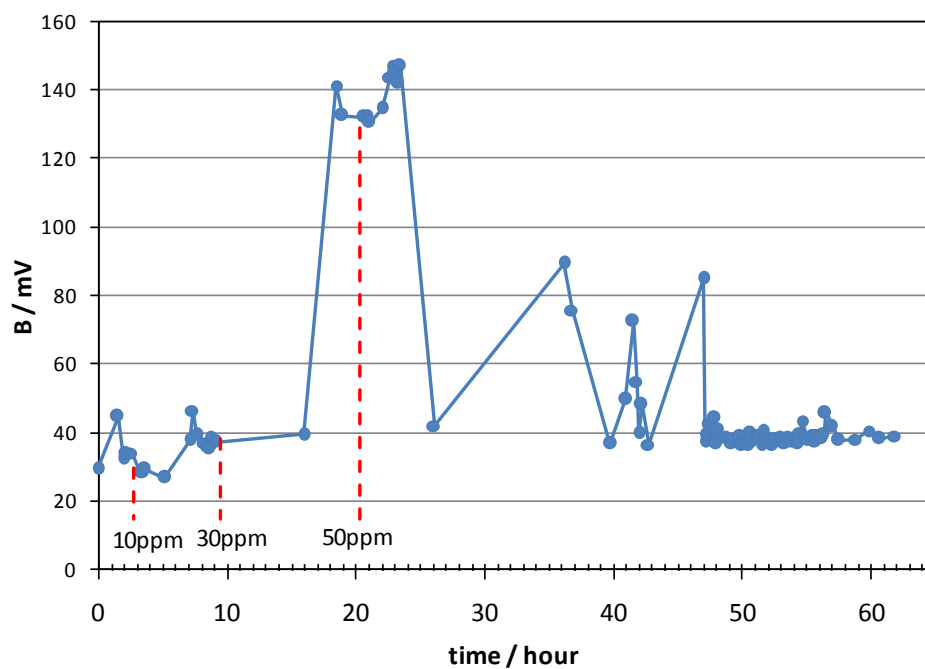


Figure 19. EFM: B value vs. elapsed time. 3 wt.% NaCl, 25°C, 1 bar CO<sub>2</sub>, pH 4.0, X-65 steel, rotating speed 1000 rpm, sequential addition of K1 inhibitor: 10- 50 ppm.

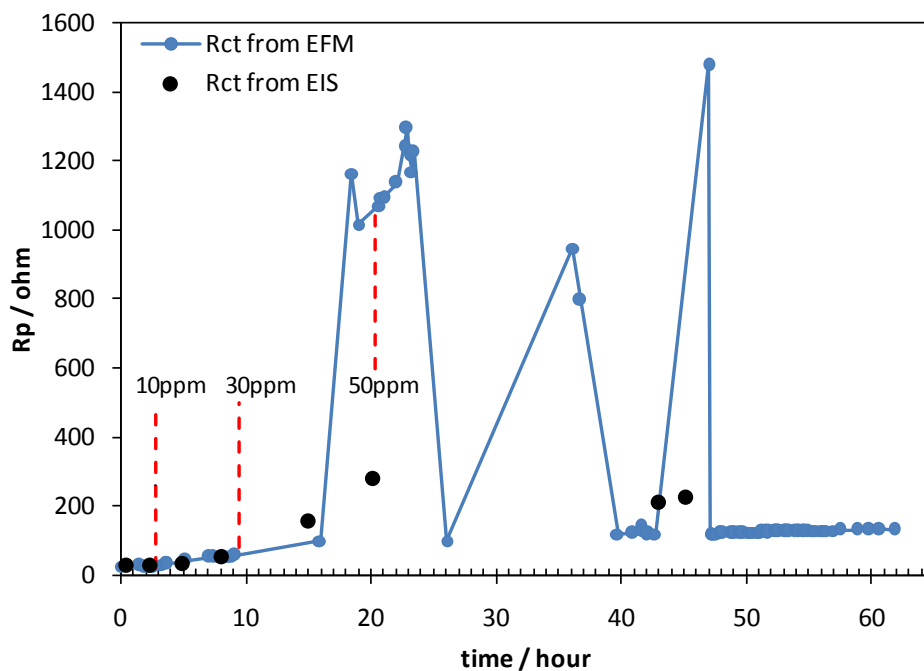


Figure 20. Comparison of  $R_{ct}$  for EFM and EIS. 3 wt.% NaCl, 25°C, 1 bar CO<sub>2</sub>, pH 4.0, X-65 steel, rotating speed 1000 rpm, sequential addition of K1 inhibitor: 10- 50 ppm.

### 3.3.5 Summary & Conclusions

Several corrosion systems were investigated with EFM and other electrochemical techniques. EFM provides instantaneous Tafel slopes and corrosion rate measurements. The EFM uses causality factors to check the reliability of EFM measurements. EFM works well in some mild steel/NaCl CO<sub>2</sub> un-inhibited and inhibited systems and gives reasonable agreement with other electrochemical corrosion monitoring techniques. When the system reaches steady state, which means that time is not an issue, this technique is no better than EIS, weight loss or potentiodynamic polarization. But when the system is changing, EFM can obtain valuable information since the measurement is very fast and provide information on the Tafel slopes, which is not accessible with other techniques.

The most valuable benefit of EFM is to be able to capture the transitional information when the Tafel slopes are changing. The change of Tafel slopes may provide more information on understanding the mechanism occurring in systems under investigation. Thanks to this feature, EFM is a possible technique for investigation of pseudo-passive layer formation.

Though EFM is a promising technique for corrosion research, some obvious drawbacks associated with this method cannot be ignored. EFM may not work well in some complicated inhibitor systems. Esra Kus *et al.*, stated that the EFM technique can be only applicable in few high corrosion rate systems [46]. Besides that, EFM has three built-in models for different corrosion mechanisms which are activation, diffusion and passivation models [40]. This means that in order to calculate corrosion rate and Tafel slopes, the corrosion mechanism of the investigated system needs to be known or predetermined. Caution and verification are necessary when EFM is used in conjunction with predetermined corrosion models.

## CHAPTER 4: INVESTIGATION OF PSEUDO-PASSIVE LAYER FORMATION IN CO<sub>2</sub> CORROSION

### 4.1 Introduction

Concentration of ferrous ion,  $[\text{Fe}^{2+}]$ , and carbonate ion,  $[\text{CO}_3^{2-}]$ , in a corrosion system determine the precipitation of  $\text{FeCO}_3$  which, in turn, is an important step in the formation of a pseudo-passive layer. Based on involved reactions in  $\text{CO}_2$  corrosion,  $[\text{CO}_3^{2-}]$  can be written in term of pH ( $[\text{H}^+]$ ) with a given  $\text{CO}_2$  partial pressure. Therefore, a theoretical calculation of the relationship of  $[\text{Fe}^{2+}]$ , pH and  $\text{FeCO}_3$  solubility can be produced (Figure 21). The water chemistry and equilibrium constants were introduced previously in Section 1.1. In Figure 21, the saturation line is the one with a  $\text{FeCO}_3$  saturation value of 1. On the right hand side of the saturation line,  $\text{FeCO}_3$  is saturated in solution and a low corrosion rate can be expected due to the formation of protective scaling. In contrast, on the left hand side of the saturation line is the region where  $\text{FeCO}_3$  is under saturated and uniform corrosion will occur without any formation of scaling. Two dotted lines with saturation value of 0.5 and 2, respectively, are also plotted. The region between these two lines is called the “gray zone”, representing an unstable  $\text{FeCO}_3$  layer formation area. It is considered a dangerous scenario because of the potential possibility of initiating localized corrosion. Due to the highly competitive dynamic processes of  $\text{FeCO}_3$  precipitation and dissolution in this region, the steel surface may be only partially covered by  $\text{FeCO}_3$ . The potential difference between surface areas covered and uncovered with  $\text{FeCO}_3$  has been reported to propagate localized corrosion by forming galvanic cells [16].

Previous research regarding spontaneous pseudo-passivation has been reported at fairly high bulk pH range (from pH 8 to pH 7.1) [43]. However, questions relating to the formation of this type of layer in oil and gas field operating pipelines which have a lower bulk pH still existed. Therefore this research is focused on investigation of formation of pseudo-passive layer over a wide pH range, especially in the region at lower pH range near the gray zone and determination of the threshold pH required for formation of such a layer. The morphology and chemical composition of this layer is also a major interest.

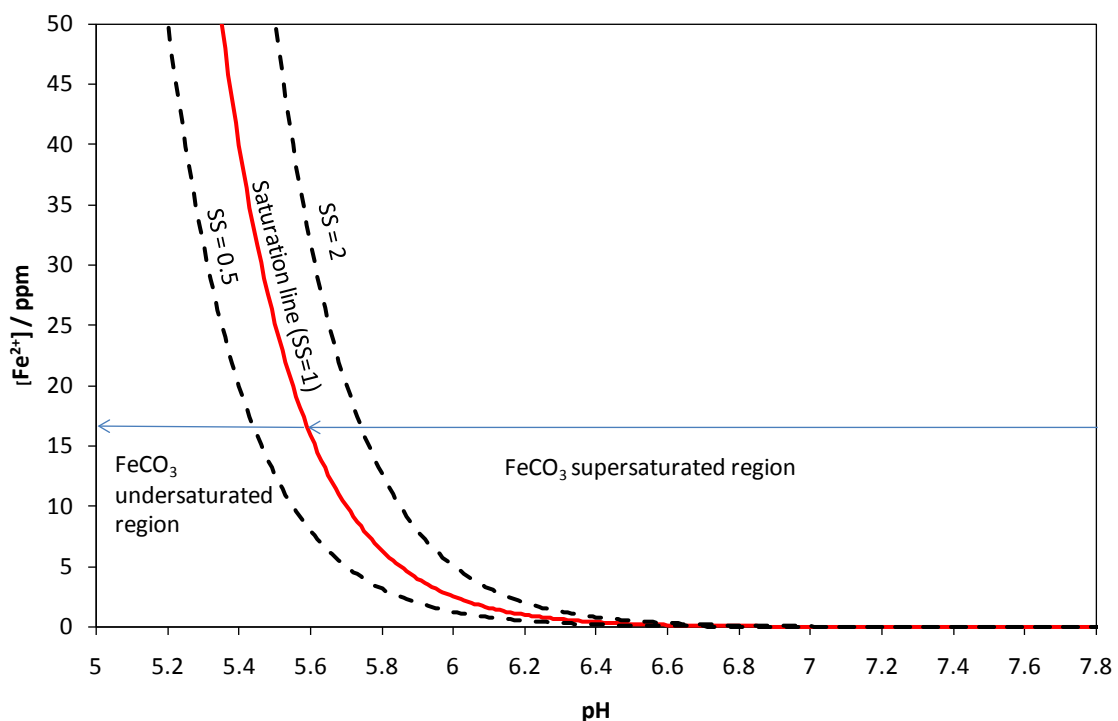


Figure 21. Calculation of the dependency of FeCO<sub>3</sub> solubility on [Fe<sup>2+</sup>] and pH. 80°C, 0.53 bar CO<sub>2</sub>, 1 wt.% NaCl.

## 4.2 Experimental

### 4.2.1 Experimental Setup and Instrumentation

The electrochemical experimental setup with a 2L glass cell is plotted (Figure 22). This setup is similar to the experimental apparatus described in the previous Section 3.2.1. A condenser was used in this setup to minimize loss of water vapor due to the higher temperature in this set of experiments (80°C). The reference electrode was saturated Ag/AgCl and platinum was used as the counter electrode. The working electrode was a cylindrical X-65 carbon steel sample with a 5.4 cm<sup>2</sup> surface area (Outer diameter: 12mm; length: 14.4mm). Flat X-65 carbon steel samples (1cm x 1cm x 0.2cm) were also placed in the glass cell for surface analysis purpose. Pictures of these two kinds of samples are presented in Figure 23.

A Gamry Reference 600 Potentiostat/Galvanostat/ZRA was used for conducting electrochemical measurements such as linear polarization resistance (LPR), electrochemical impedance spectroscopy (EIS), electrochemical frequency modulation (EFM) and potentiodynamic polarization (PP).

When needed, [Fe<sup>2+</sup>] in the glass cell was measured *ex situ* by a Thermo SCIENTIFIC GENESYS 10vis spectrophotometer.

A JEOL JSM-6390LV system was utilized for SEM analysis. Regular XRD and GIXRD analysis were done with a Bruker D8 Discover X-Ray Diffractometer and a Rigaku Ultima IV X-Ray Diffractometer. Samples for TEM analysis were prepared by focused ion beam (FIB) using a FEI Helios 600 system. TEM-EDS analysis was done by a FEI Tecnai F20 system.

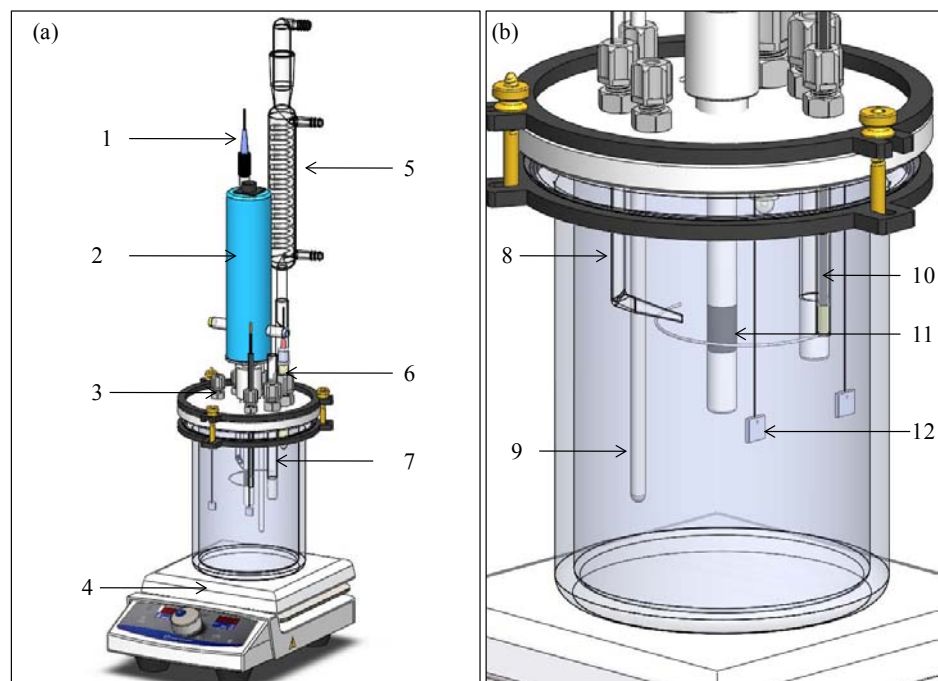


Figure 22. (a) Schematic of glass cell setup; (b) Zoomed in view of glass cell.  
(Courtesy of Cody Shafer, research engineer, ICMT, Ohio University)

- |                        |                                 |                      |
|------------------------|---------------------------------|----------------------|
| 1. Reference electrode | 2. Rotator motor                | 3. Gas outlet        |
| 4. Hot plate           | 5. Condenser                    | 6. pH probe          |
| 7. Gas inlet tubing    | 8. Luggin capillary             | 9. Temperature probe |
| 10. Counter electrode  | 11. Rotating cylinder electrode | 12. Flat sample      |

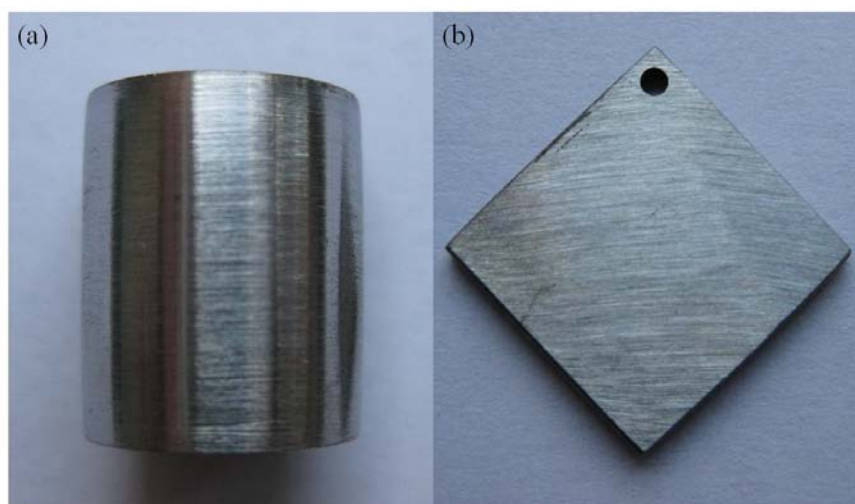


Figure 23. Pictures of (a) cylindrical sample and (b) hanging flat sample.

#### 4.2.2 Test Matrix

The effect of pH on the formation of pseudo-passive layer was studied. Several test systems were investigated. The test matrix is listed (Table 8). The pH of the studied system was lowered gradually from 7.8 to 5.6.

Table 8. Test matrix for pseudo-passive layer study in CO<sub>2</sub> corrosion system

pH	7.8	7.1	6.6	6.0	5.6
Carbon steel type	X-65				
Temperature (°C)	80				
Electrolyte	1 wt% NaCl				
CO <sub>2</sub> partial pressure (bar)	0.53				
Flow velocity (rpm)	0				
Initial [Fe <sup>2+</sup> ] (ppm)	0	0	50	100	1000
Electrochemical techniques	EFM, EIS, PP, LPR				

#### 4.2.3 Procedure

The test electrolyte was a 1 wt% NaCl solution, prepared in the glass cell and purged with a continuous gas flow. Required temperature was achieved by hot plate. The pH was adjusted by addition of NaHCO<sub>3</sub>, Na<sub>2</sub>CO<sub>3</sub>, NaOH or diluted HCl solution. The cylindrical sample was used as the working electrode for electrochemical tests and the hanging flat sample was used for surface analysis techniques. Both samples were polished by abrasive paper with 400 and 600 grit numbers sequentially. After having

been polished, samples were put into an ultrasonic bath with isopropanol then taken out and dried by cool air. Finally, samples were placed in the glass cell for testing.

In tests with pH below 7.1, ferrous ion was added into the glass cell in the form of  $\text{FeCl}_2$  solution in order to increase the ferrous ion concentration and accelerate the comparatively slow  $\text{FeCO}_3$  layer formation process. The  $\text{FeCl}_2$  solution was prepared by placing  $\text{FeCl}_2 \cdot 4\text{H}_2\text{O}$  powder into a beaker with deionized water which had been  $\text{N}_2$  deaerated by continuous  $\text{N}_2$  gas flow.  $[\text{Fe}^{2+}]$  in the glass cell was monitored using spectrophotometric methods.

After each experiment, the samples were carefully handled to minimize oxidation of the corrosion product layer. The flat sample was removed from the glass cell after the layer formed and immediately dipped into  $\text{N}_2$  deaerated deionized water to remove soluble salts on the specimen surface. The sample was then dipped into isopropanol and dried by cool air. After this treatment, sample was stored in a desiccator to maintain its dry and deaerated condition. The cylindrical sample was treated following the same procedure as that of flat samples after each test. For surface analysis, specimens were first characterized by SEM/EDS analysis in order to observe the gross surface features of the pseudo-passive layer. Specimens with pseudo-passive layer formed were then sent for XRD/GIXRD and TEM analysis to confirm the chemistry information and structure of the pseudo-passive layer.

#### 4.2.4 Parameter Selections of Electrochemical Measurements

Electrochemical techniques were used to investigate pseudo-passive layer system. The parameter selections were similar to the selection that has been described previously in Section 3.2.4. Detailed information is listed in Table 9 below.

Table 9. Parameter selections of electrochemical measurements

<b>Technique</b>	<b>Parameters</b>
<i>LPR</i>	Scan Rate: 0.1 mV / s. Sample Period: 1s. Polarization range: $\pm 5$ mV (vs. EOC). Resolution: 0.125 mV B value: 26 mV
<i>EIS</i>	Initial Frequency: 10000 Hz, Final Frequency: 0.001 Hz. Points per Decade: 5. AC Voltage: 5 mV. DC Voltage: 0 vs. EOC.
<i>Potentiodynamic Polarization</i>	Scan Rate: 0.1667 mV / s. Sample Period: 1s. Anodic overvoltage: 0~ 0.5 V (vs. EOC).
<i>EFM</i>	Base Frequency: 0.1Hz. Amplitude: 10 mV. Multiplier A and Multiplier B: 2, 5. I/E Range Mode: Auto. DC Voltage: 0 V vs. EOC. Number of Cycles: 16 or 32. Max Current: 0.1 – 1.0 mA. Corrosion Type: Activation / Diffusion.

### 4.3 Results and Discussion

An open circuit potential increase that occurs concurrently with a corrosion rate decrease is considered a distinctive indication of the achievement of a pseudo-passive layer. Therefore, open circuit potential, corrosion rate and Tafel slopes were followed during the tests.

#### *4.3.1 Tests at pH 7.8*

A test at a comparatively high pH was conducted in order to verify the validity and repeatability of previous work done by other researchers [24]. The variation of open circuit potential with time is shown in Figure 24 for each repeated test. From this graph, an open circuit potential increase of at least 100 mV was observed. This shift of open circuit potential shows that the pseudo-passive layer had formed. The results were also compared with previous work done by Han [43], and they have a good agreement. The appearances of the plots for these tests are slightly different due to the use of different pH adjusters ( $\text{NaHCO}_3$ /  $\text{Na}_2\text{CO}_3$ /  $\text{NaOH}$ ). However, in all cases there is a significant open circuit potential increase at the end.

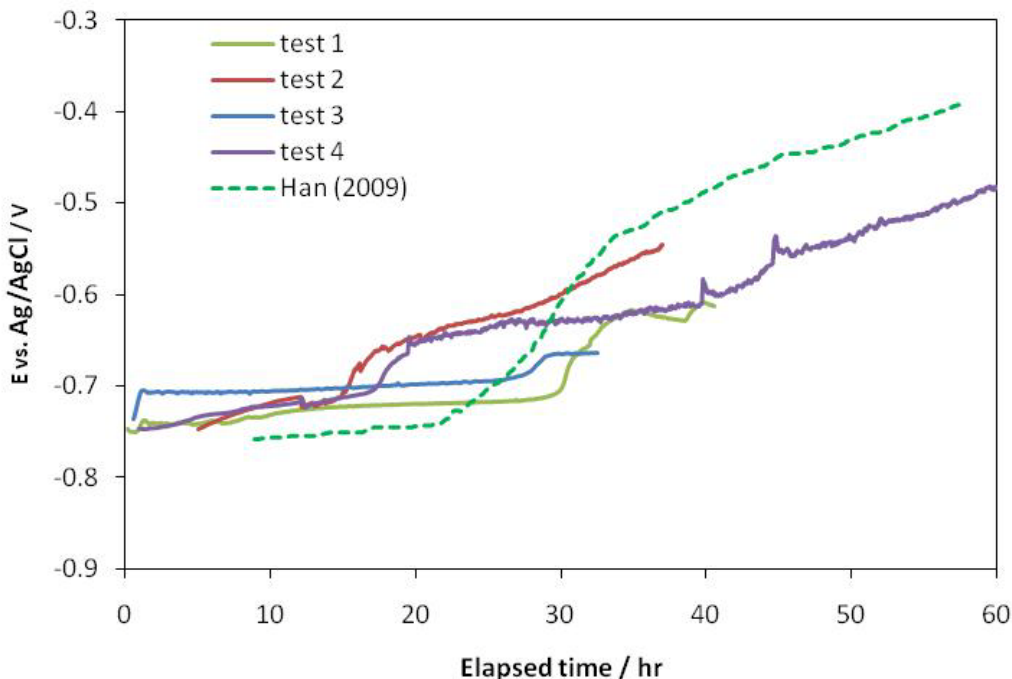


Figure 24. Comparison of open circuit potential during the test. 80°C, 0.53 bar CO<sub>2</sub>, stagnant, 1 wt.% NaCl, pH 7.8, X-65 carbon steel. (SEM images of the samples are shown in Figure 34 and Figure 36)

The LPR technique was used to monitor the pseudo-passivation process by following the corrosion rate during the test. Along with an open circuit potential increase, the corrosion rate decreased significantly which indicated a formation of the pseudo-passive layer (Figure 25). In this system, the applicability of LPR measurement was checked. The effects of the polarization direction on the measurement and the effect of polarization potential on corroding system were investigated. Two methods of polarization were conducted during the test. One is positive polarization: the electrode was polarized from -5 mV to 5 mV vs. OCP; the other is negative polarization: the electrode was polarized from 5mV to -5 mV vs. OCP. The result (Figure 26) suggests that the polarization direction has no effect on the measurement. The effect of applied

polarization potential on this system was checked by comparing the OCP with corrosion potential. The corrosion potential is the potential at which the polarization current is zero, and if the polarization does not influence the system much, this corrosion potential should be identical with the OCP at that moment. Figure 27 is the comparison of the OCP and corrosion potential. It can be concluded that these potentials are identical, and LPR does not significantly influence the system. Hence, the LPR technique worked well and provided reliable results in this system.

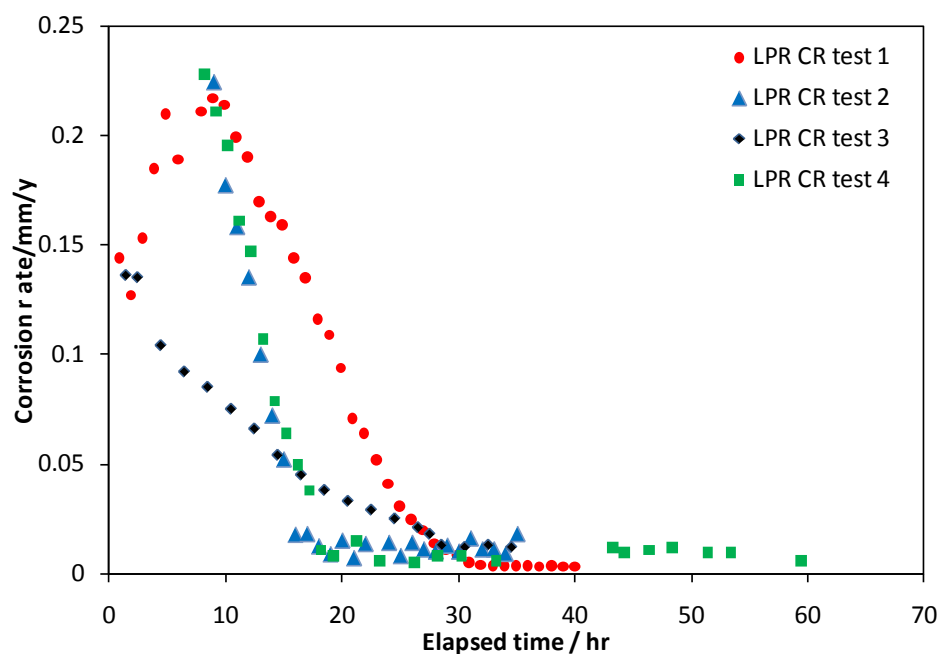


Figure 25. LPR corrosion rates during the formation of pseudo-passive layer. 80°C, pH 7.8, 1 wt.% NaCl, 0.53 bar CO<sub>2</sub>, stagnant flow, X-65 carbon steel. (SEM images of the samples are shown in Figure 34 and Figure 36)

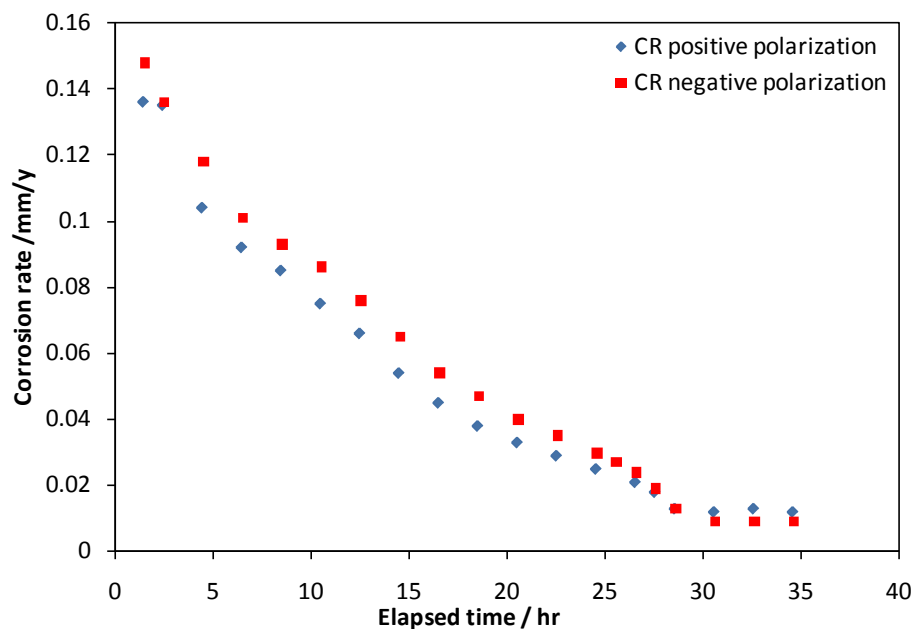


Figure 26. LPR corrosion rates using different polarization directions of test3. 80°C, 0.53 bar CO<sub>2</sub>, 1 wt.% NaCl, stagnant flow, pH 7.8.

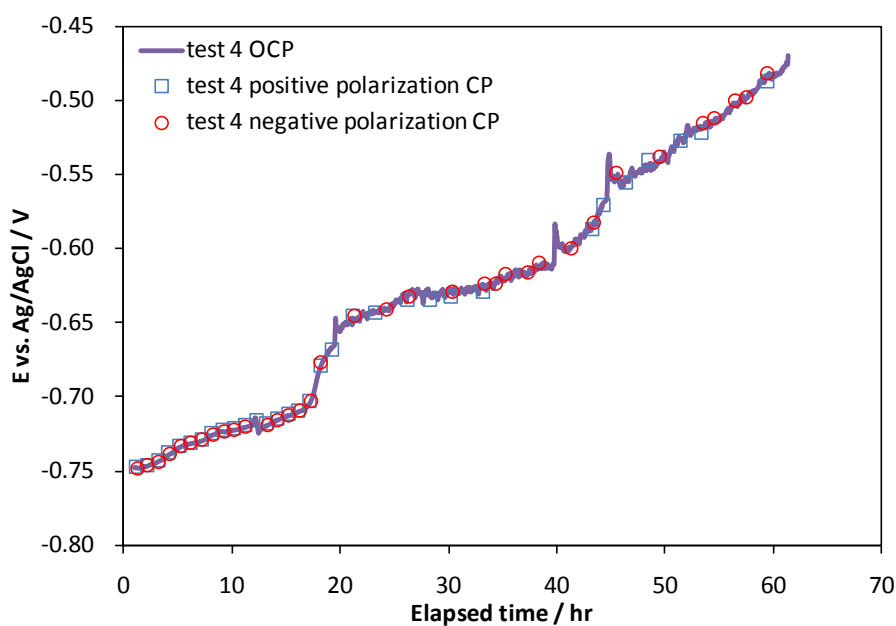


Figure 27. Comparison of open circuit potential and corrosion potential for positive polarization LPR measurements and negative polarization LPR measurements of test4. 80°C, 0.53 bar CO<sub>2</sub>, 1 wt.% NaCl, stagnant flow, pH 7.8. (SEM image of the sample is shown in Figure 36)

The EFM technique was also used in the test and compared with LPR results. EFM worked well when the active model was chosen (Figure 28). However, closer examination of the data from 20 to 60 hours shows a distinct difference between LPR and EFM results for those below 0.1 mm/yr (Figure 29), which may only be related to the measurement technique. The passive model of EFM did not work in this system (Figure 30). This indicates that the application of EFM in this system has many limitations and EFM results were minimally useful.

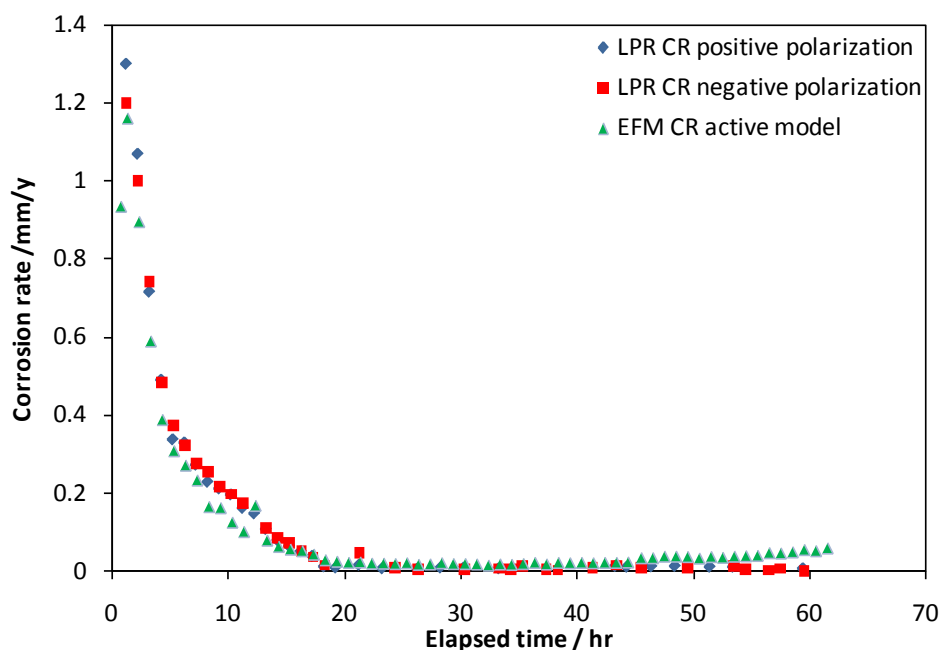


Figure 28. Comparison of EFM (active model) and LPR corrosion rates of test4. 80°C, 0.53 bar CO<sub>2</sub>, 1 wt.% NaCl, stagnant flow, pH 7.8. (SEM image of the sample is shown in Figure 36)

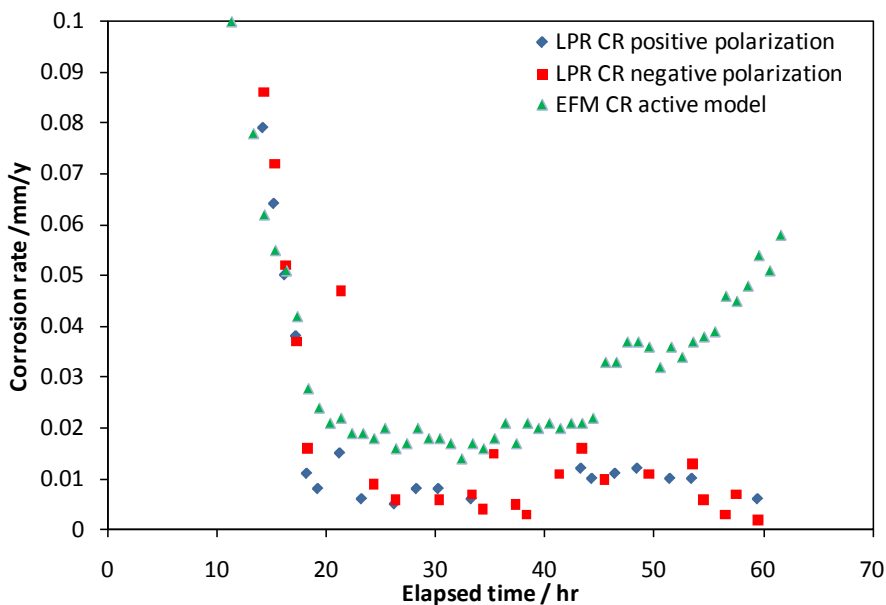


Figure 29. Comparison of EFM (active model) and LPR results of test4 at corrosion rates measured below 0.1 mm/yr. 80°C, 0.53 bar CO<sub>2</sub>, 1 wt.% NaCl, stagnant, pH 7.8. (SEM image of the sample is shown in Figure 36)

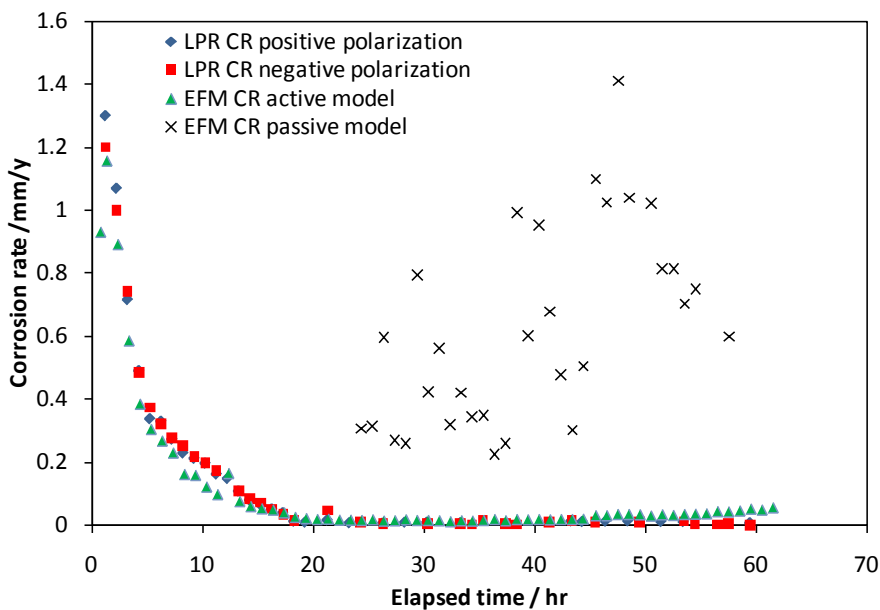


Figure 30. Comparison of EFM (passive model) and LPR corrosion rates of test4. 80°C, 0.53 bar CO<sub>2</sub>, 1 wt.% NaCl, stagnant, pH 7.8. (SEM image of the sample is shown in Figure 36)

EIS measurements were also conducted in this system in order to investigate the formation of pseudo-passive layer. The impedance of the system dramatically increased by the formation of the pseudo-passive layer (Figure 31 and Figure 32). The Nyquist plot of the system after the pseudo-passive layer formed can be compared with that of stainless steel with a passive surface behavior in similar test conditions from the literature (Figure 33) [47]. The similarity of the appearances of these plots suggests that this system with X-65 steel in a CO<sub>2</sub> corrosion environment had developed pseudo-passive behavior.

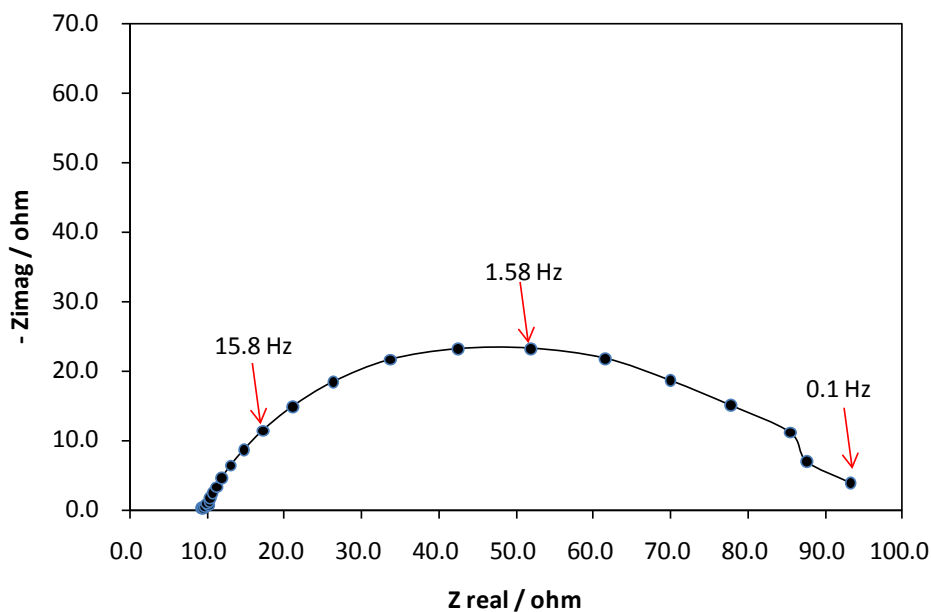


Figure 31. Nyquist plot of test3, 0.2 hour after the electrode immersed into the electrolyte. 80°C, 0.53 bar CO<sub>2</sub>, 1 wt.% NaCl, stagnant, pH 7.8.

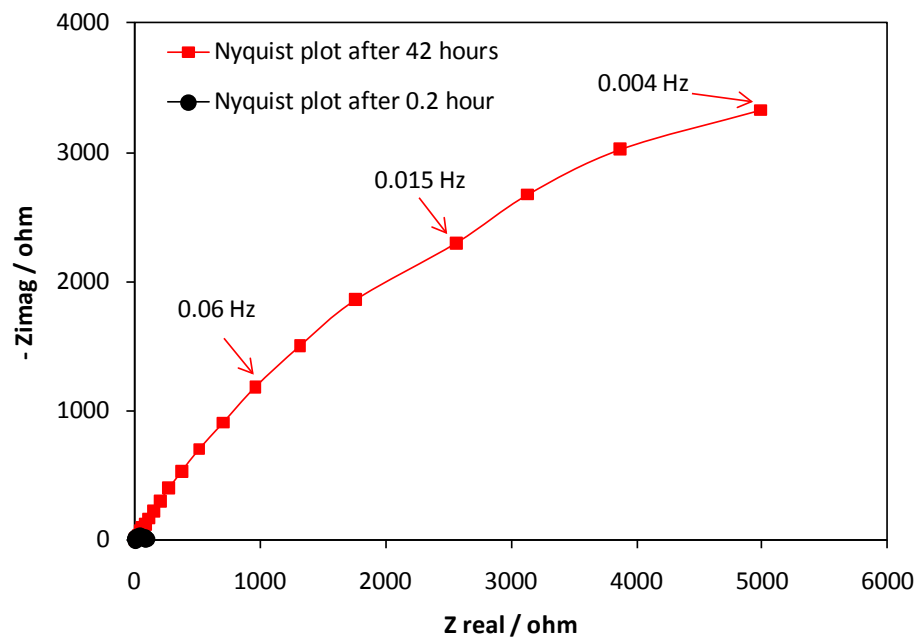


Figure 32. Comparison of the Nyquist plots during test3. 80°C, 0.53 bar CO<sub>2</sub>, 1 wt.% NaCl, stagnant, pH 7.8.

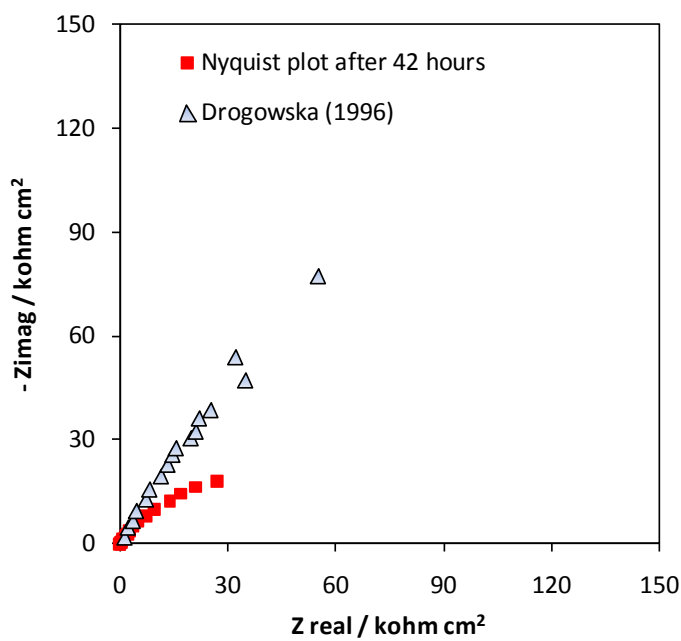


Figure 33. Comparison of Nyquist plots: 42 hour of test3 and result from reference (E=0.5V) [47].

Initial surface analysis was done by the SEM/EDS techniques (Figure 34, Figure 35, Figure 36 and Figure 37). From the SEM/EDS results,  $\text{FeCO}_3$  prisms were identified on the steel surface. In order to confirm the possible presence of other compounds ( $\text{Fe}(\text{OH})_2$  or  $\text{Fe}_3\text{O}_4$ ) within the corrosion product layer, XRD and GIXRD techniques were utilized (work done at Rigaku Inc). Figure 38 shows the regular XRD patterns, and both iron substrate and  $\text{FeCO}_3$  layer can be identified. GIXRD was also employed to eliminate peaks from the iron substrate and to attempt to detect possible trace amounts of passivating iron oxides phases in the  $\text{FeCO}_3$  layer, if present. From the GIXRD patterns (Figure 39), only  $\text{FeCO}_3$  can be identified and no crystalline iron oxides were found. It is possible that iron oxides could be present below the equipment detection limits, were amorphous, or did not exist in this test.

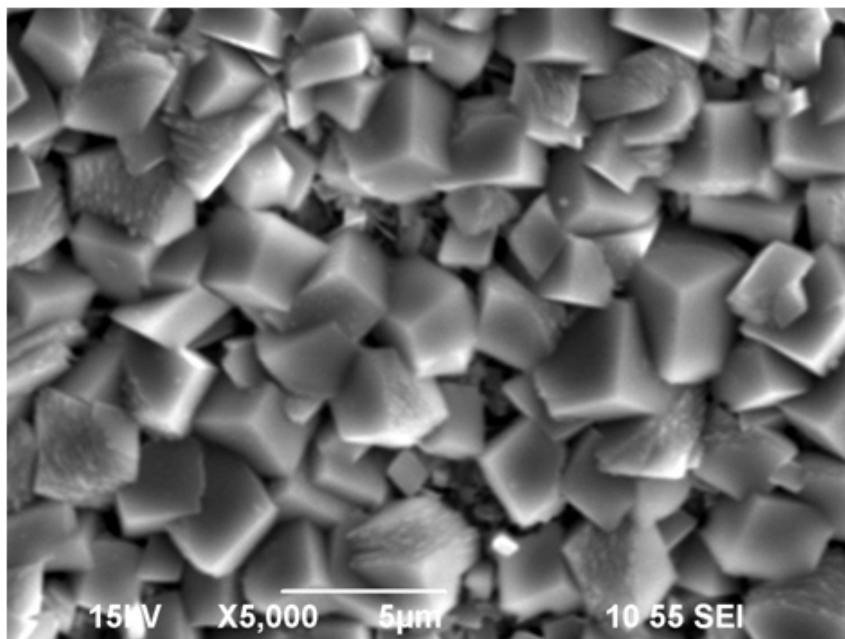


Figure 34. SEM image of X65 flat sample of test2. 80°C, 0.53 bar  $\text{CO}_2$ , 1 wt.% NaCl, stagnant flow, pH 7.8, after 38 hours. (LPR corrosion rate is shown in Figure 25)

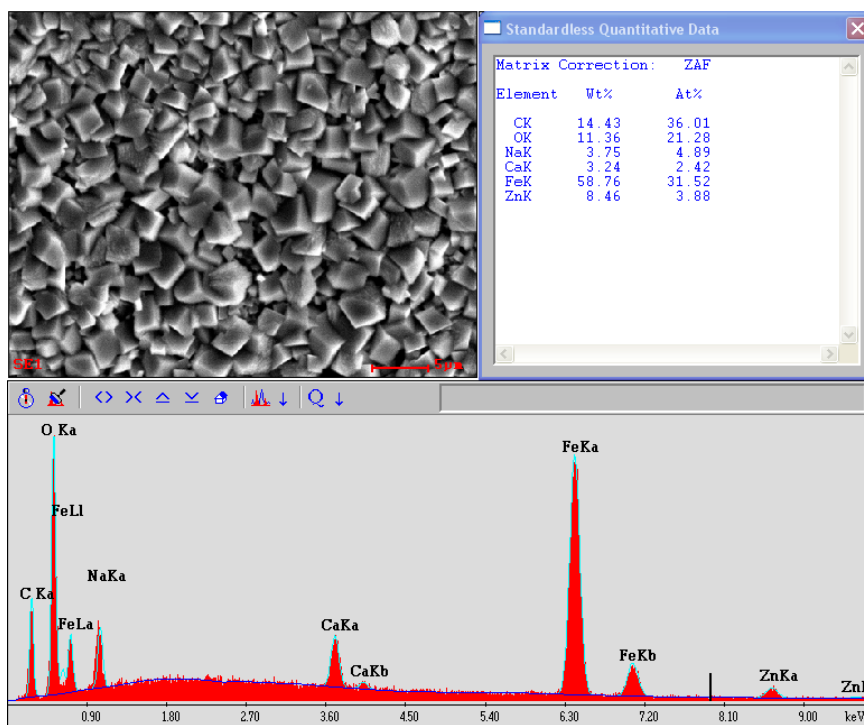


Figure 35. EDS result of X65 flat sample of test2. 80°C, 0.53 bar CO<sub>2</sub>, 1 wt.% NaCl, stagnant, pH 7.8, after 38 hours.  
(LPR corrosion rate is shown in Figure 25)

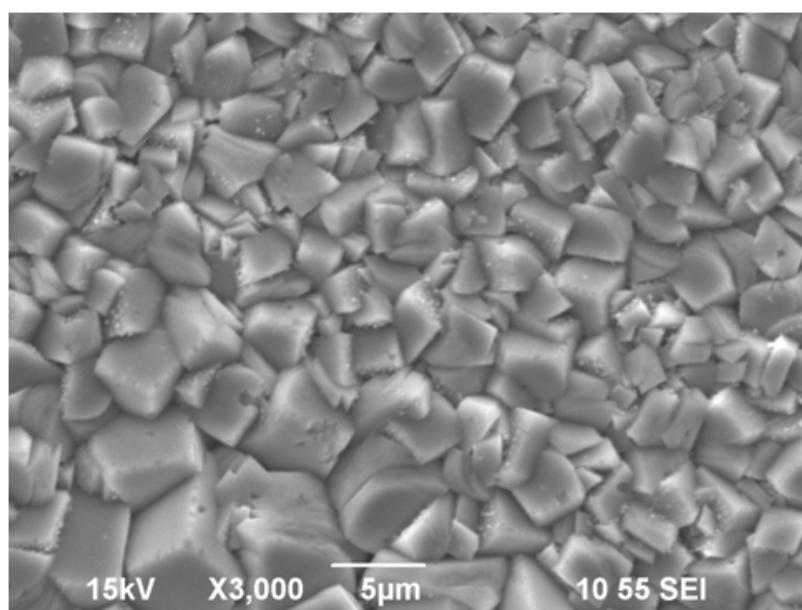


Figure 36. SEM image of X65 flat sample of test4. 80°C, 0.53 bar CO<sub>2</sub>, 1 wt.% NaCl, stagnant flow, pH 7.8, after 60 hours.  
(LPR corrosion rate is shown in Figure 25)

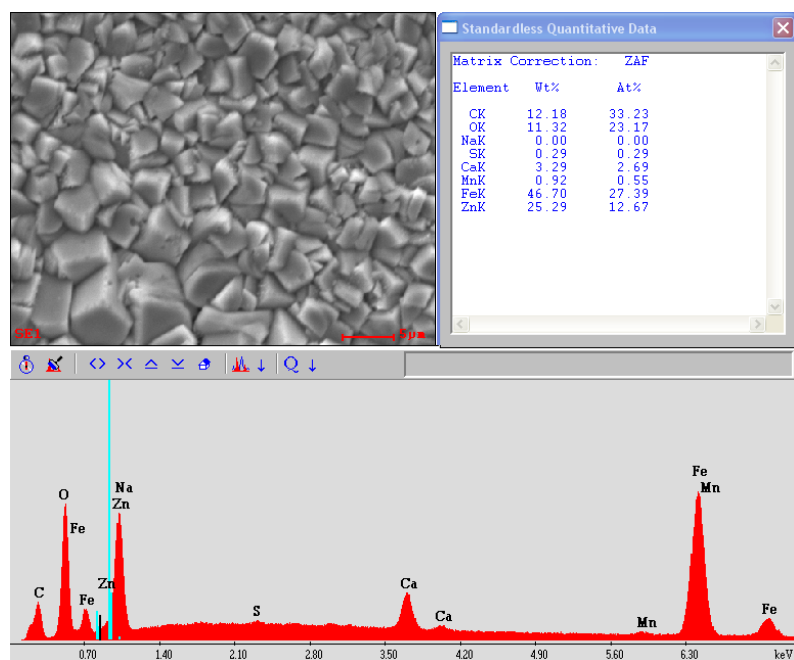


Figure 37. EDS result of X65 flat sample of test4. 80°C, 0.53 bar CO<sub>2</sub>, 1 wt.% NaCl, stagnant, pH 7.8, after 60 hours.  
(LPR corrosion rate is shown in Figure 25)

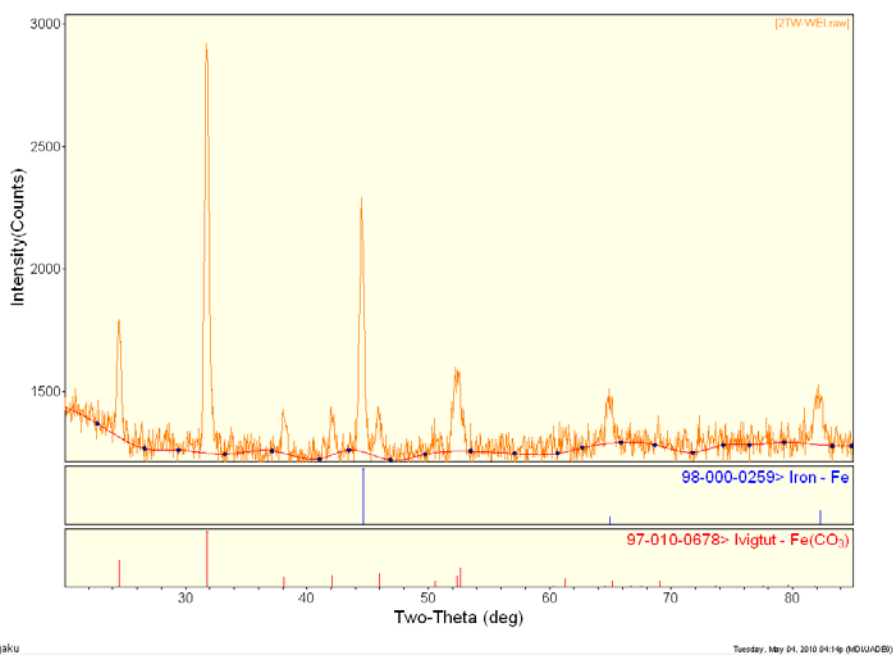


Figure 38. Conventional XRD pattern of X65 flat sample after test4 at pH 7.8.  
(LPR corrosion rate is shown in Figure 25)

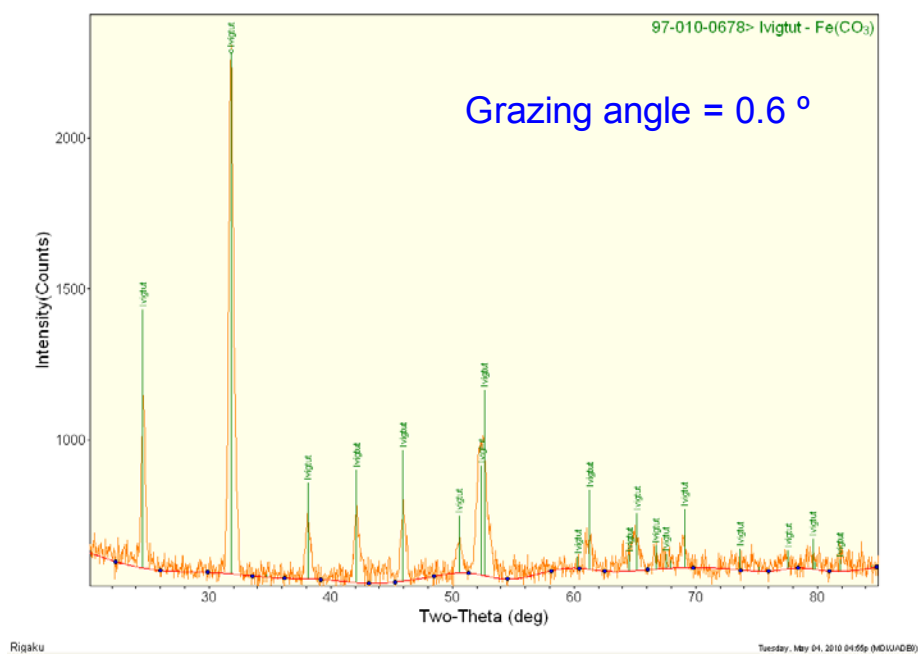


Figure 39. GIXRD pattern of X65 flat sample after test4 at pH 7.8. (LPR corrosion rate is shown in Figure 25)

### 4.3.2 Tests at pH 7.1

At pH 7.1, three different sets of tests were conducted. These tests were called short term, mid-term and long term, corresponding to different durations. The goal was to analyze samples at different stages of the process towards pseudo-passivation. The test matrix is listed (Table 10).

Table 10. Test arrangement at pH 7.1

Test	Test duration
Short term	1 hour
Mid-term	12 hour
Long term	4 days

The short term test was aimed at monitoring the initial stage of the pseudo-passive layer formation. Figure 40 is the variation of open circuit potential with time and no major change is observed, and the corrosion rate was still high, about 1.0 mm/y, which suggests that no passivation was achieved during this time. Further surface analysis by SEM (Figure 41) confirmed the previous suggestion. From the SEM image, it can be seen that part of the surface of the sample was covered by  $\text{FeCO}_3$ . The plate shaped  $\text{FeCO}_3$  is the dominant form of this product layer and few prismatic shaped  $\text{FeCO}_3$  crystals can be

observed. However, since the  $\text{FeCO}_3$  layer was not fully developed, along with the high corrosion rate, it is reasonable to conclude that no pseudo-passivation was achieved.

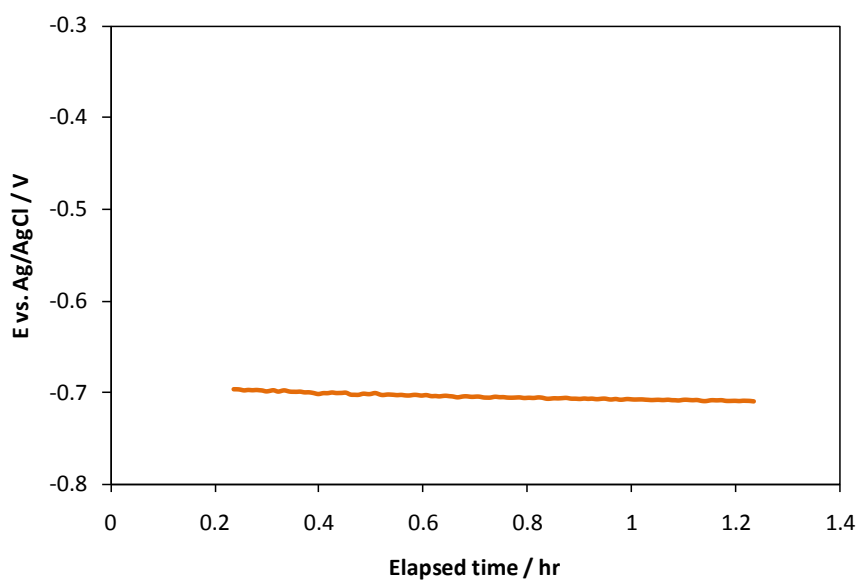


Figure 40. Open circuit potential during the short term test,  $80^\circ\text{C}$ , 0.53 bar  $\text{CO}_2$ , 1 wt.% NaCl, stagnant, pH 7.1.

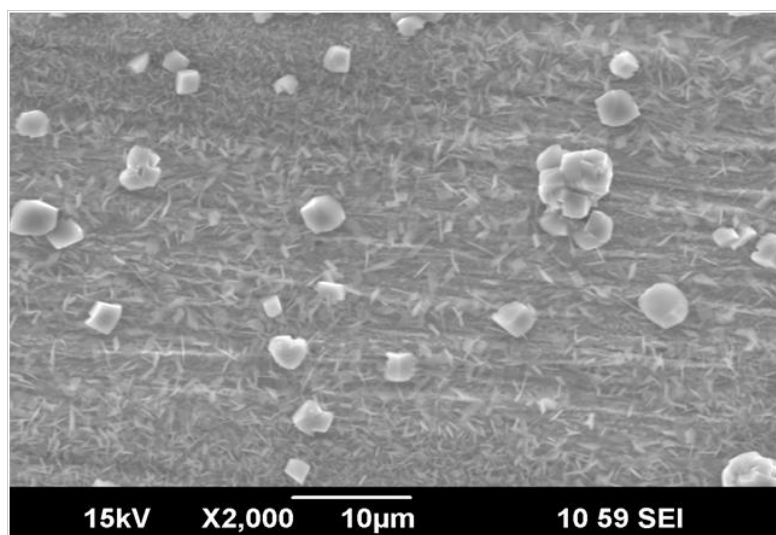


Figure 41. SEM image of X-65 flat sample after short term test.  $80^\circ\text{C}$ , 0.53 bar  $\text{CO}_2$ , 1 wt.% NaCl, stagnant, pH 7.1.  
(OCP during the test is shown in Figure 40)

The mid-term test was an approximately 12 hour test investigating the intermediate stage of the pseudo-passive layer formation. Figure 42 is the variation of open circuit potential with time and no major change is observed, which suggests that no pseudo-passivation was achieved after 12 hours. However, the variation of corrosion rate with time (Figure 43) indicates a trend of corrosion rate decrease. From the SEM image (Figure 44), it can be seen that most of the sample surface was covered by  $\text{FeCO}_3$ . Many prismatic  $\text{FeCO}_3$  crystals along with the plate-like morphology can be observed. Considering the decrease of corrosion rate, this layer, to some extent, provided protection to the steel surface as a surface coverage effect. However, without the increase in potential, pseudo-passivation was still not achieved which could be due to the porous structure of this layer.

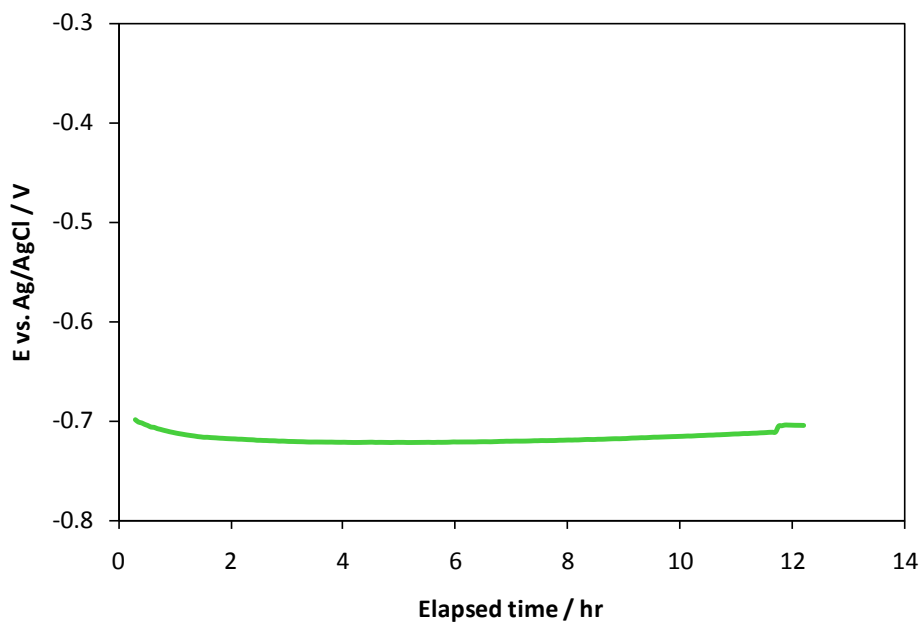


Figure 42. Open circuit potential during the mid-term test,  $80^{\circ}\text{C}$ , 0.53 bar  $\text{CO}_2$ , 1 wt.% NaCl, stagnant, pH 7.1. (SEM image of the sample is shown in Figure 44)

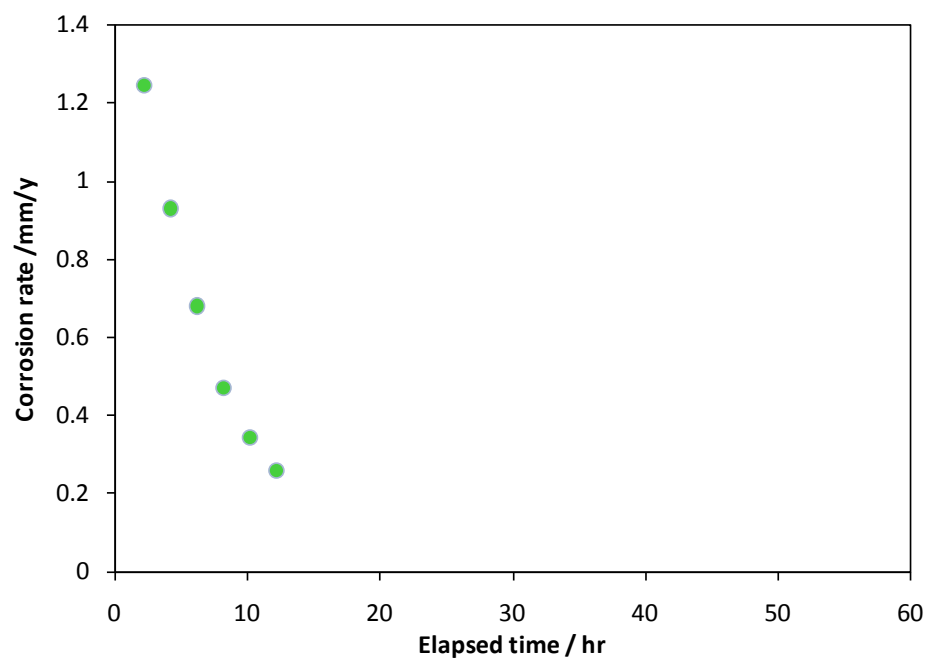


Figure 43. LPR corrosion rate during the mid-term test, 80°C, 0.53 bar CO<sub>2</sub>, 1 wt.% NaCl, stagnant, pH 7.1.

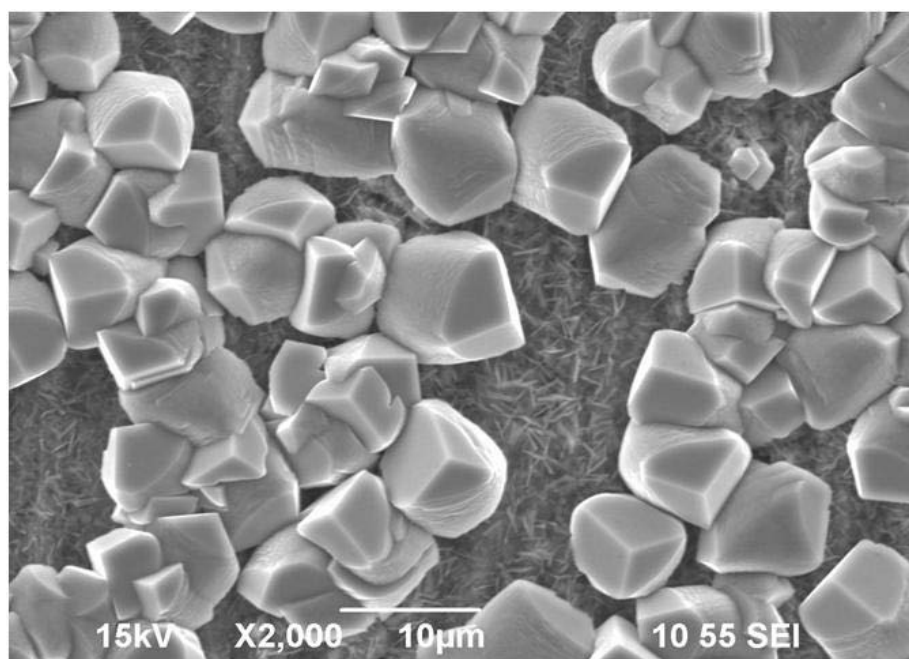


Figure 44. SEM image of X65 flat sample after mid-term test. 80°C, 0.53 bar CO<sub>2</sub>, 1 wt.% NaCl, stagnant, pH 7.1.  
(OCP and corrosion rate are shown in Figure 42 and Figure 43)

The long term test was an approximately 4 days test investigating the final stage when the pseudo-passive layer was achieved. Figure 45 is the variation of open circuit potential with time and a significant potential increase with an approximately 200 mV magnitude can be observed. Along with the decrease of corrosion rate (Figure 46), this change in potential shows that pseudo-passivation was achieved. The impedance change was recorded as well (Figure 47, Figure 48 and Figure 49). From Figure 48, at low frequencies, Warburg impedance can be seen for data taken after 40 hours of the test, which suggests that a diffusion barrier had formed during the 40 hours duration of the test; and this is accompanied by the observed formation of a  $\text{FeCO}_3$  layer. The significant impedance increase also confirms that a protective layer formed on the steel surface due to pseudo-passivation.

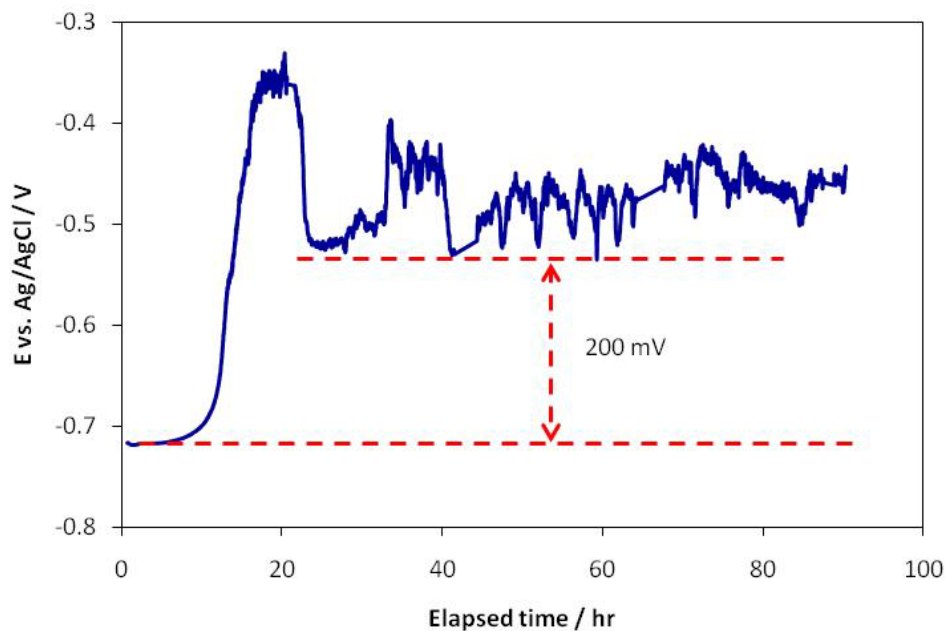


Figure 45. Open circuit potential, long term test, 80°C, 0.53 bar  $\text{CO}_2$ , 1 wt.% NaCl, stagnant, pH 7.1.  
(SEM image of the sample is shown in Figure 50)

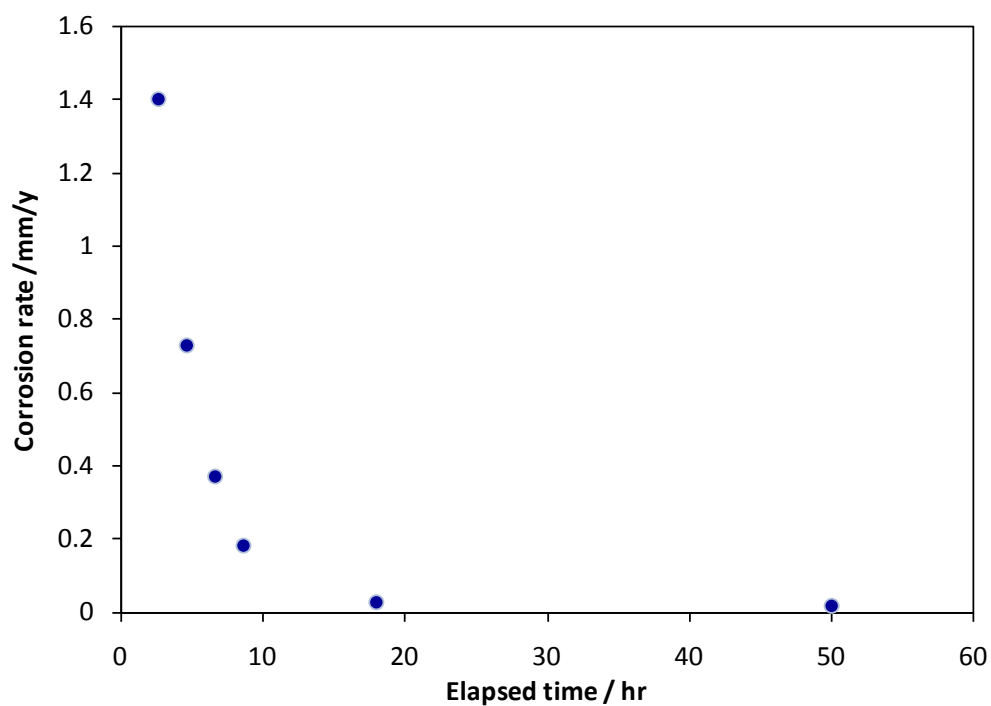


Figure 46. LPR, long term test, 80°C, 0.53 bar CO<sub>2</sub>, 1 wt.% NaCl, stagnant, pH 7.1. (SEM image of the sample is shown in Figure 50)

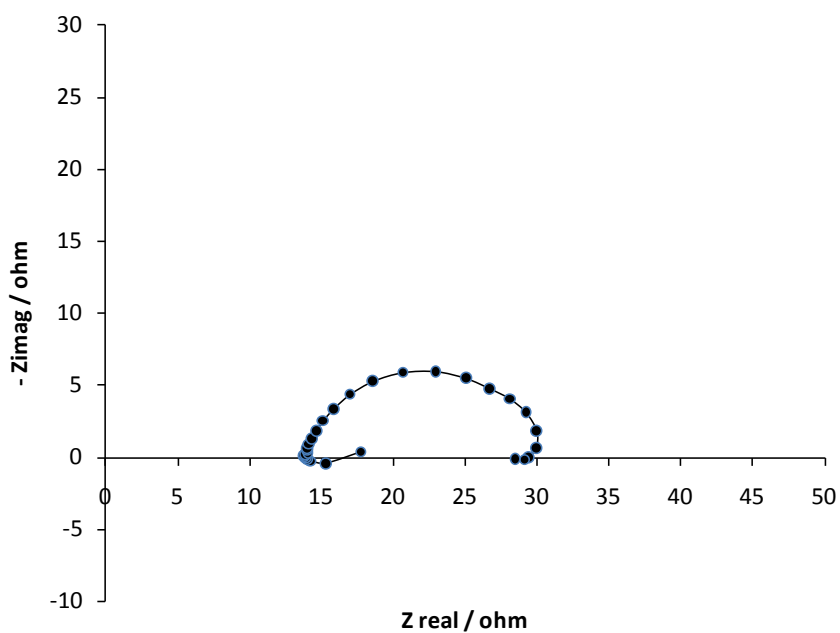


Figure 47. Nyquist plot, 0.5 hour after the electrode immersed into the electrolyte. 80°C, 0.53 bar CO<sub>2</sub>, 1 wt.% NaCl, stagnant, pH 7.1.

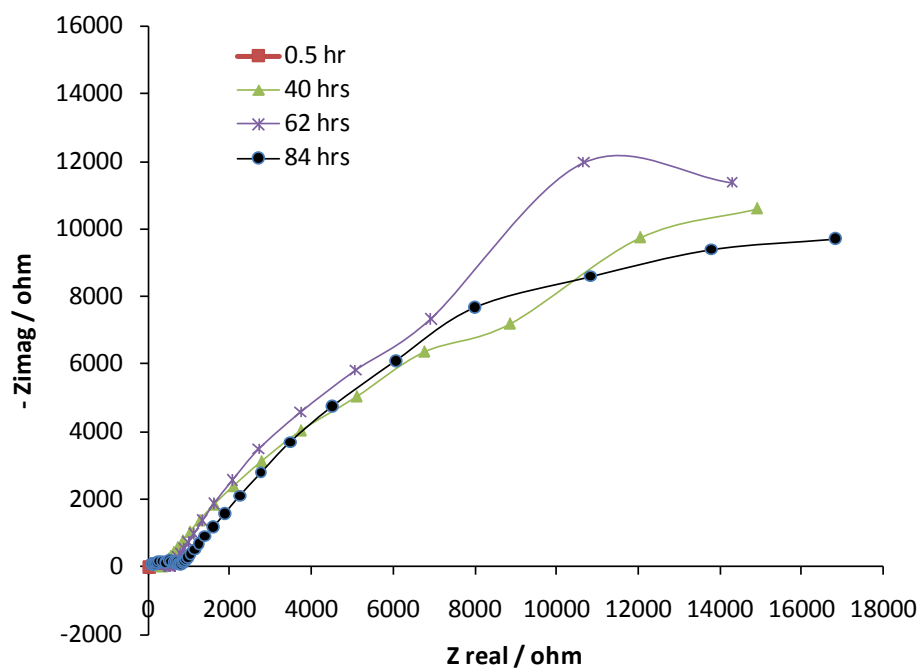


Figure 48. Comparison of the Nyquist plots during the test. 80°C, 0.53 bar CO<sub>2</sub>, 1 wt.% NaCl, stagnant, pH 7.1.

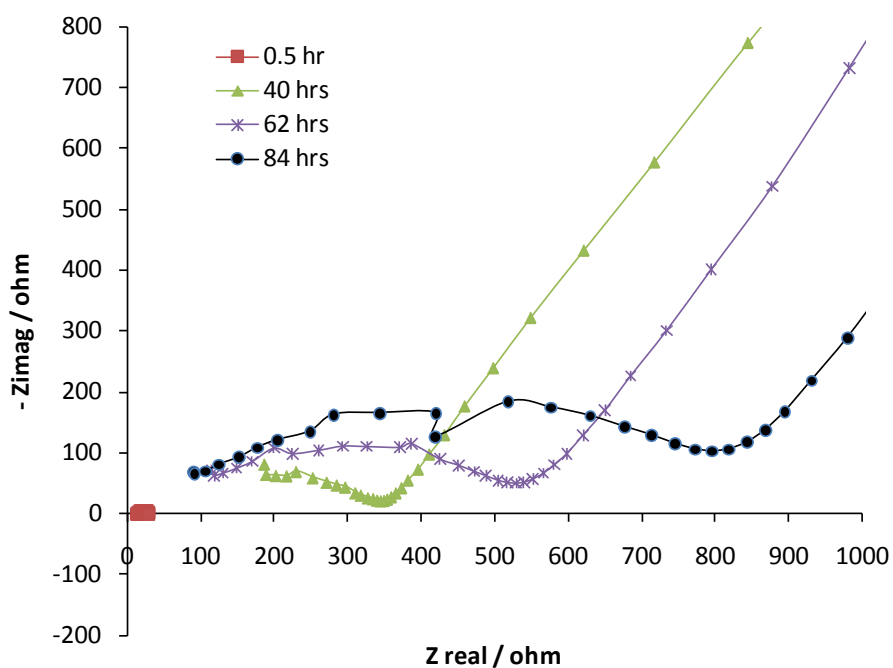


Figure 49. Comparison of the Nyquist plots during the test in a zoomed in region. 80°C, 0.53 bar CO<sub>2</sub>, 1 wt.% NaCl, stagnant, pH 7.1.

SEM image of the sample surface is shown in Figure 50. The majority of the sample surface is covered by  $\text{FeCO}_3$  prisms and the space between these  $\text{FeCO}_3$  prisms is covered by a material which was not immediately identified; note, too, the absence of  $\text{FeCO}_3$  in the plate form. Due to the observation of a pseudo-passive behavior, a thin layer or metal oxides were assumed to exist on the surface. Consequently, a grazing angle XRD (GIXRD) was done in order to investigate the composition of this thin layer. Figure 51 is the GIXRD pattern of the sample surface (work done at the Ohio State University). Only  $\text{FeCO}_3$  can be identified, minor phases might not be detectable due to amorphicity, instrument noise or detection limits.

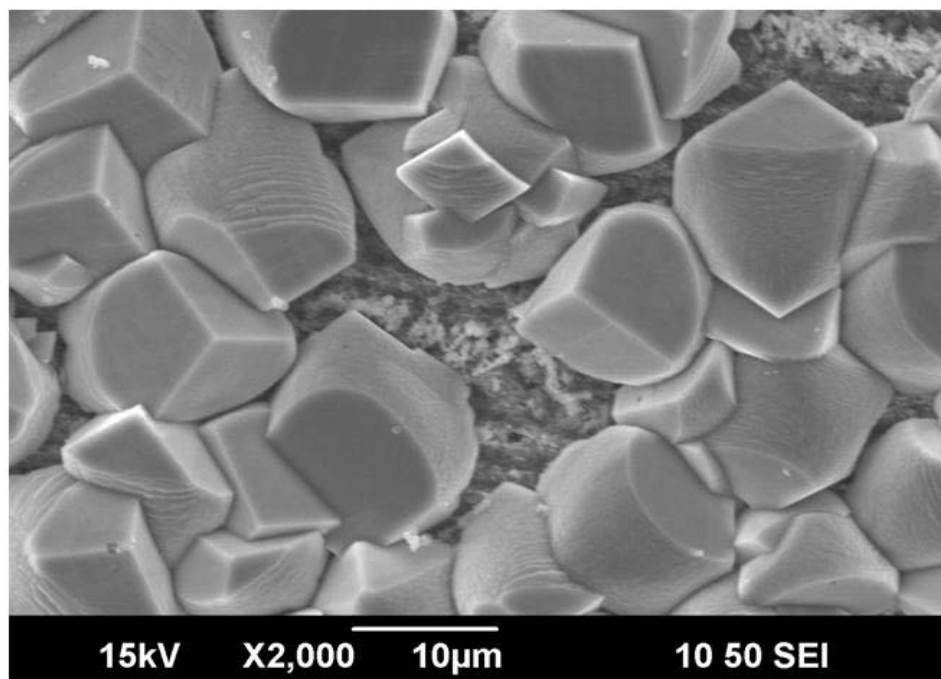


Figure 50. SEM image of X65 flat sample after long term test. 80°C, 0.53 bar  $\text{CO}_2$ , 1 wt.% NaCl, stagnant, pH 7.1. (OCP and corrosion rate are shown in Figure 45 and Figure 46)

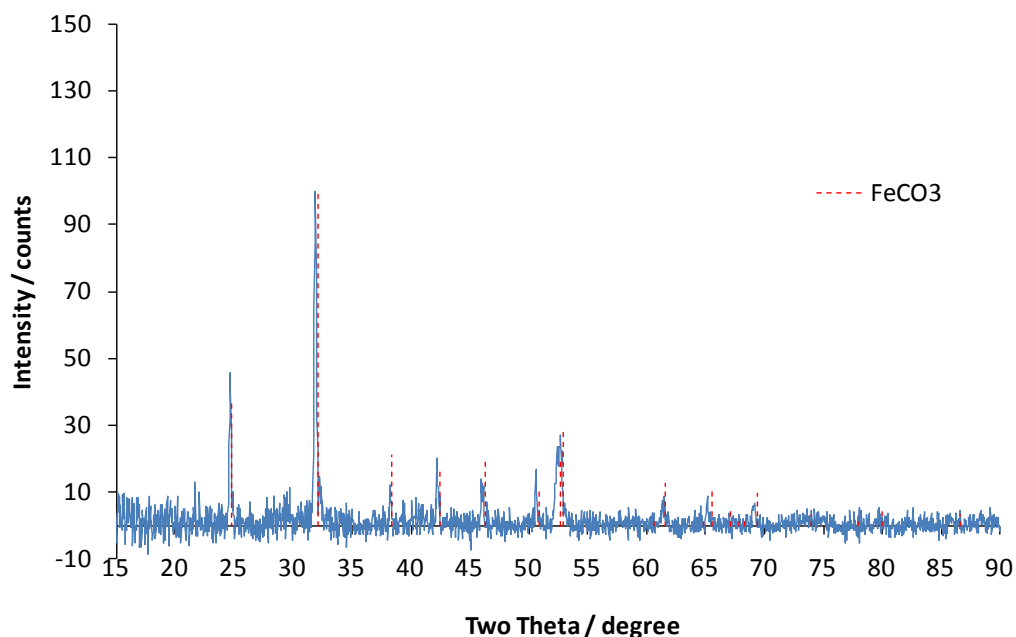


Figure 51. GIXRD pattern of X65 flat sample after long term test. (OCP and corrosion rate are shown in Figure 45 and Figure 46)

In order to investigate the detailed structure of this layer, TEM was employed (work done at the Ohio State University). A TEM sample with  $\text{FeCO}_3$  prisms and their adjacent area was cut as shown in Figure 52. The FIB cutting process is illustrated in Figure 53 and Figure 54. Figure 55 is the actual sample for TEM analysis. A continuous layer can be seen on the steel surface. Five individual areas of this layer (Figure 56) were analyzed by EDS in order to obtain compositional information. Location 1 (Figure 57) is the boundary of two  $\text{FeCO}_3$  prisms. A line pattern EDS scan was performed (Figure 58). The stable chemical composition with scan distance suggests that it is a homogenous phase,  $\text{FeCO}_3$ . Location 2 is the layer beneath Location 1 and is adjacent to the Fe substrate (Figure 59 and Figure 60). A line pattern EDS scan (Figure 61) was performed. This suggests a transition from Fe to  $\text{FeCO}_3$ . In Figure 61, between position of 0.02  $\mu\text{m}$  and

0.06  $\mu\text{m}$ , a transition of the content of Fe, C and O can be observed, which may suggest the possible presence of iron oxides. Due to the absence of electron diffraction, this possibility had not been verified. A point pattern EDS (Figure 62) was carried out at Point A near Location 2. The result confirms the presence of Fe, C and O, suggesting the presence of  $\text{FeCO}_3$ . For Location 3 and 5, line pattern EDS scans were also performed (Figure 63, Figure 64, Figure 65, Figure 66 and Figure 67). The results show the same transition from Fe to  $\text{FeCO}_3$ . For Location 4, some spots with lighter color can be seen and the point pattern EDS shows less oxygen content compared to  $\text{FeCO}_3$  (Figure 68 and Figure 69). This is thought to be iron carbide.

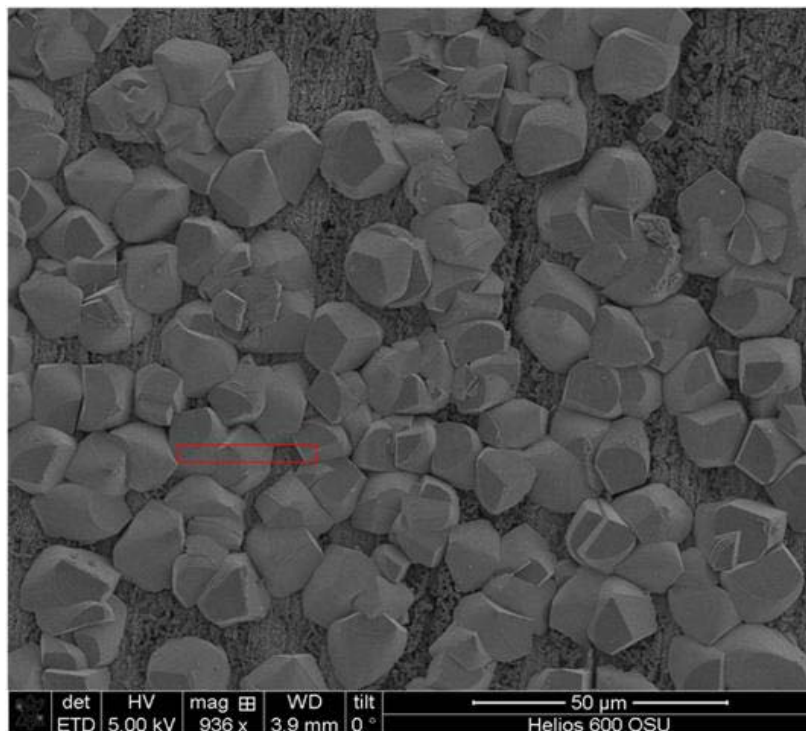


Figure 52. SEM image of TEM sample cutting area after long term test. 80°C, 0.53 bar  $\text{CO}_2$ , 1 wt.% NaCl, stagnant, pH 7.1. (OCP and corrosion rate are shown in Figure 45 and Figure 46)

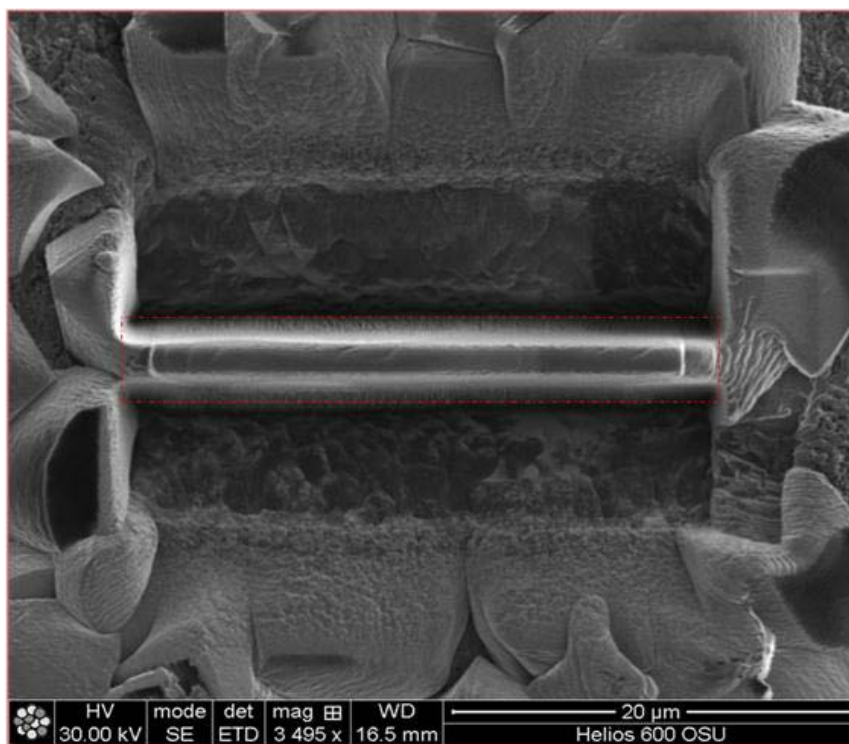


Figure 53. Top view of TEM sample cutting area shown in Figure 52

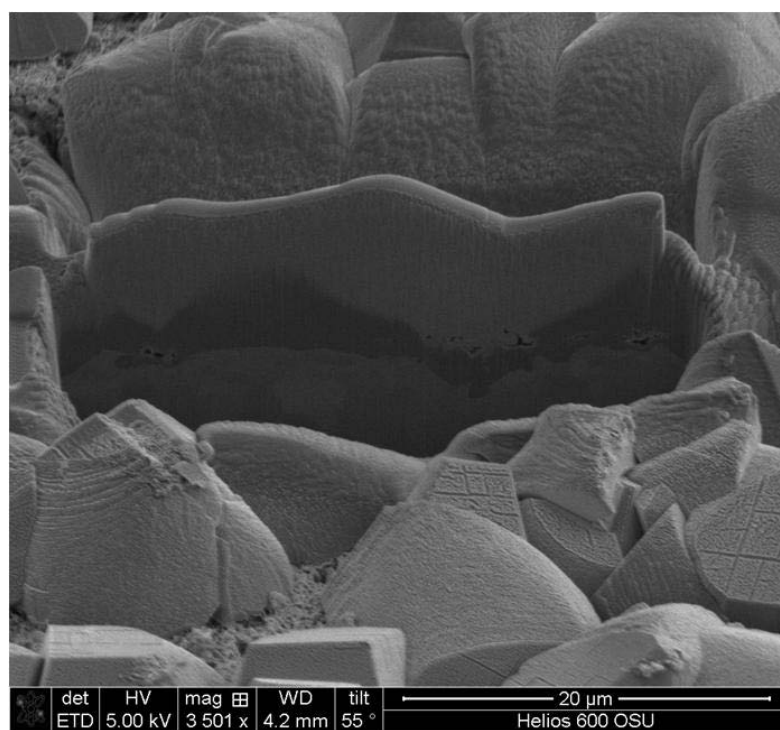


Figure 54. Side view of TEM sample cutting area with 55° tilt angle.

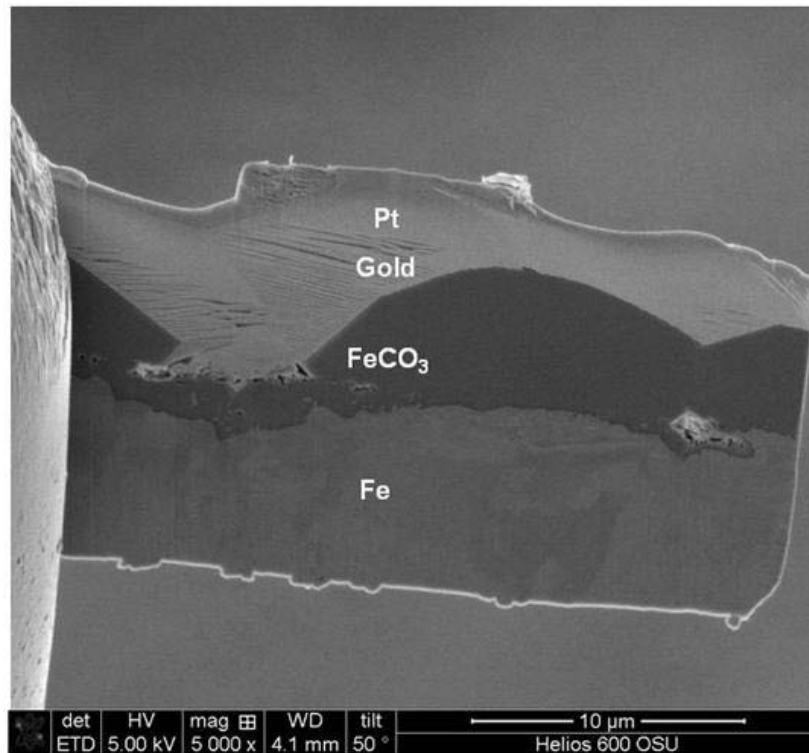


Figure 55. Side view of prepared TEM sample.

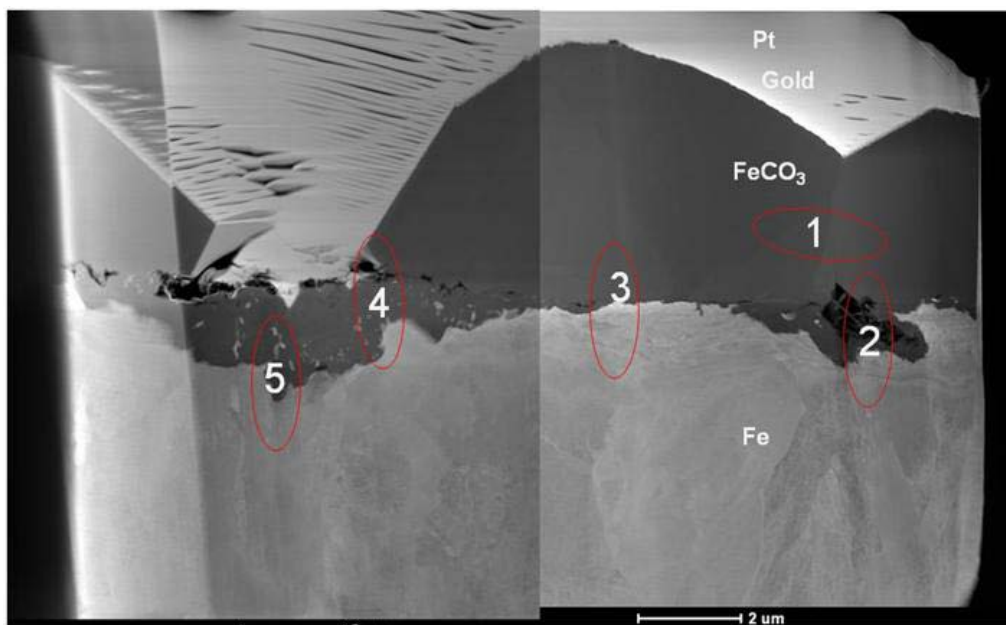


Figure 56. Specific locations analyzed by TEM-EDS.  
(OCP and corrosion rate are shown in Figure 45 and Figure 46)



Figure 57. Location 1 shown in Figure 56 analyzed by TEM-EDS.

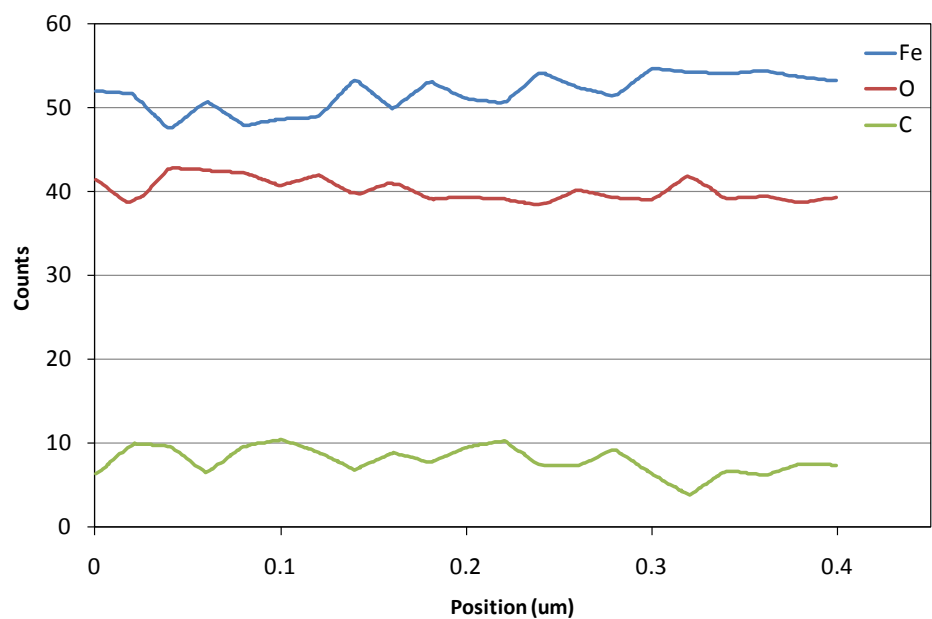


Figure 58. Line pattern EDS scan result of location 1 shown in Figure 57.

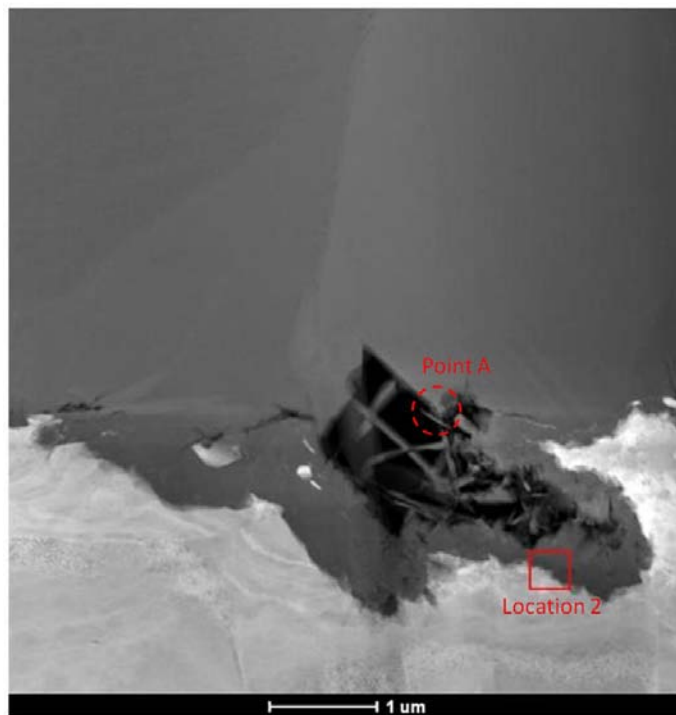


Figure 59. TEM analysis areas of location 2 shown in Figure 56 and point A.

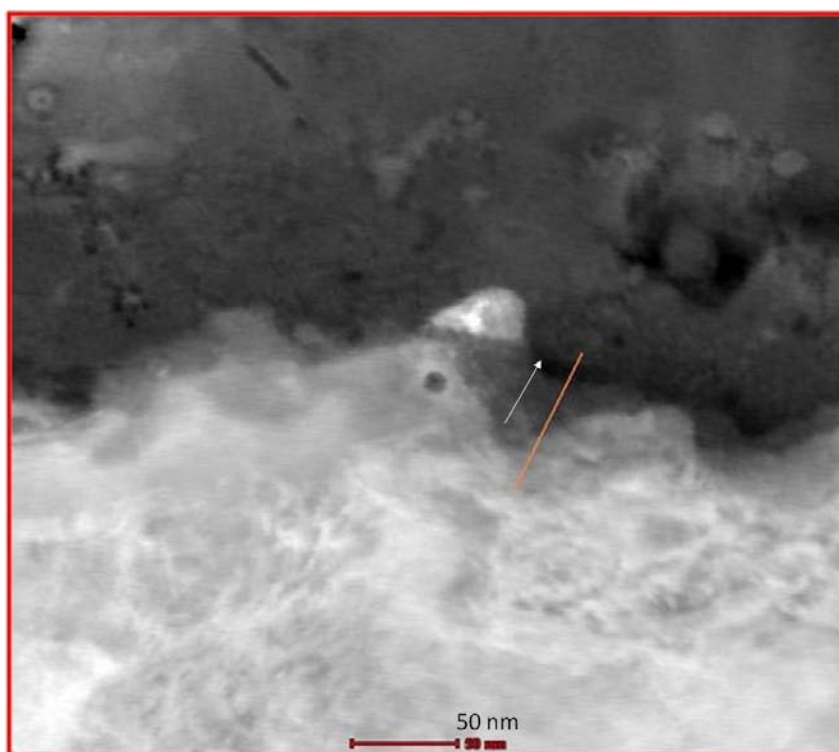


Figure 60. Zoomed in image of TEM analysis area at location 2 shown in Figure 59.

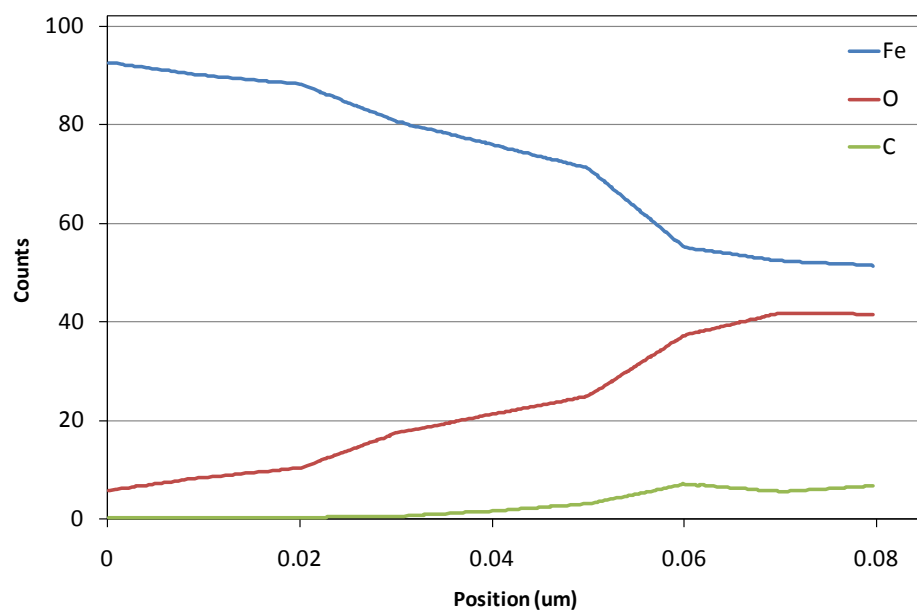


Figure 61. Line pattern EDS scan result of location 2 shown in Figure 59.

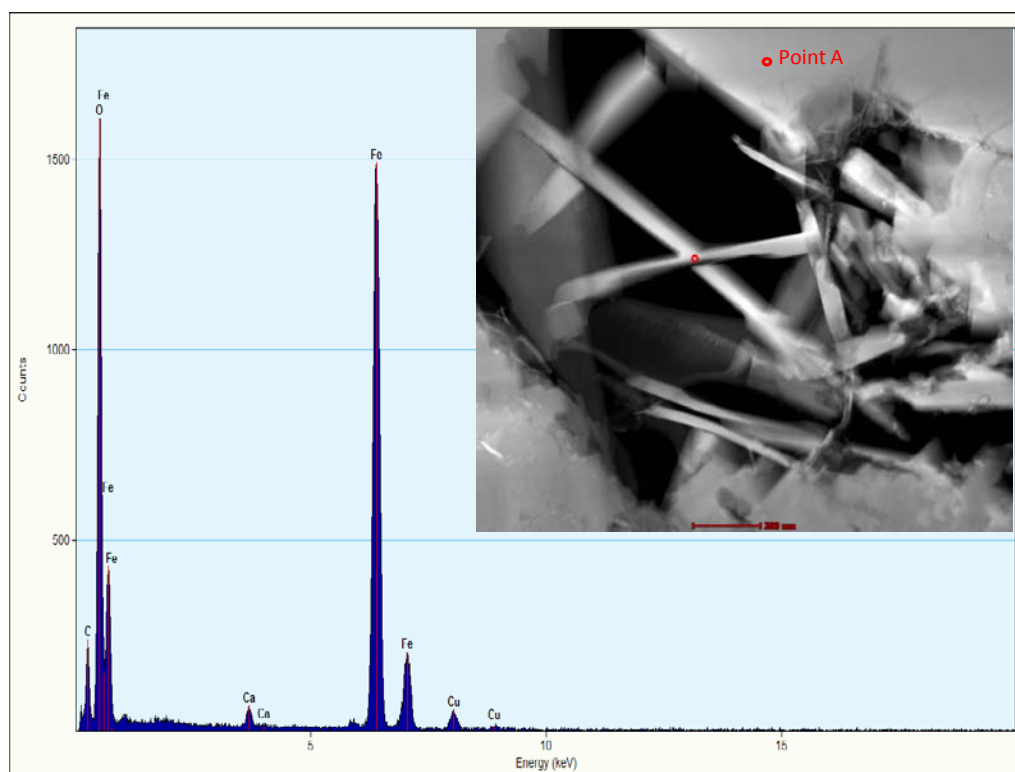


Figure 62. Point pattern EDS result of Point A shown in Figure 59.

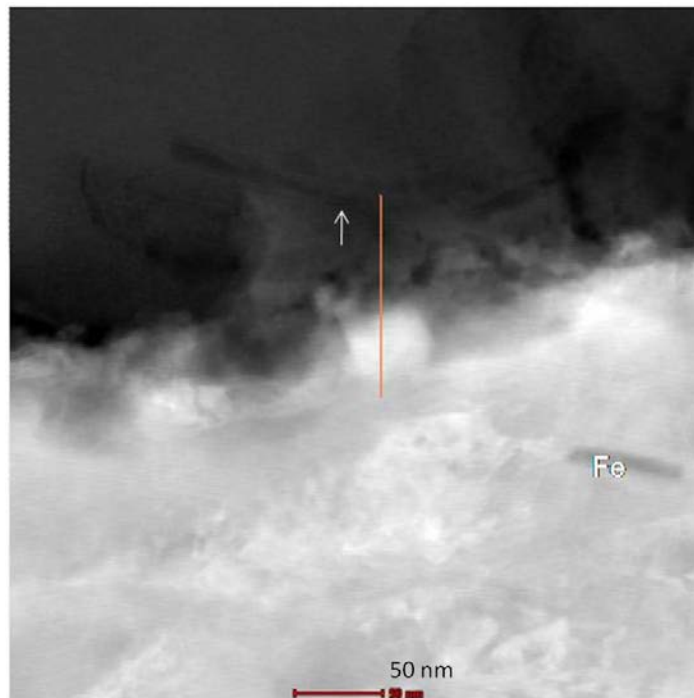


Figure 63. TEM analysis area of location 3 shown in Figure 56.

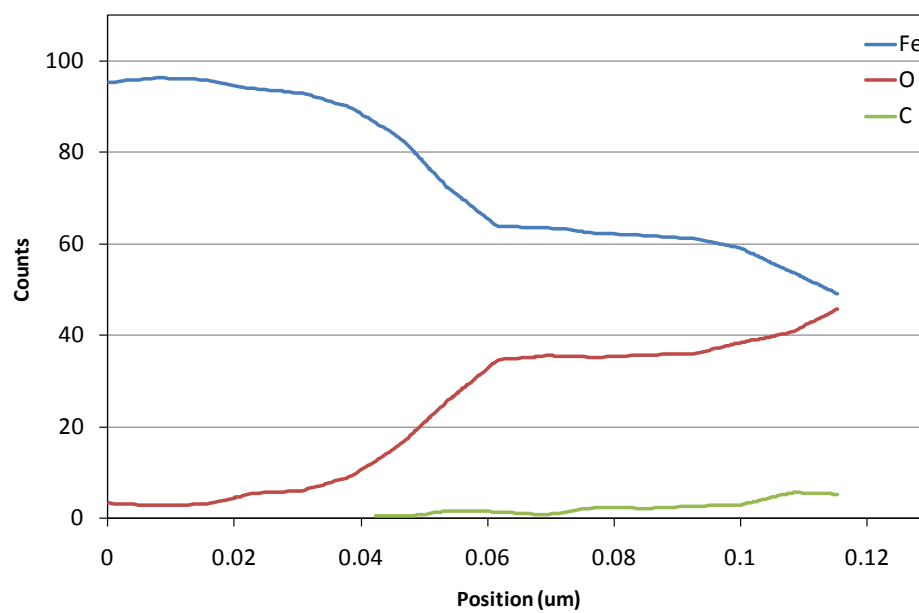


Figure 64. Line pattern EDS scan result of location 3 shown in Figure 63.

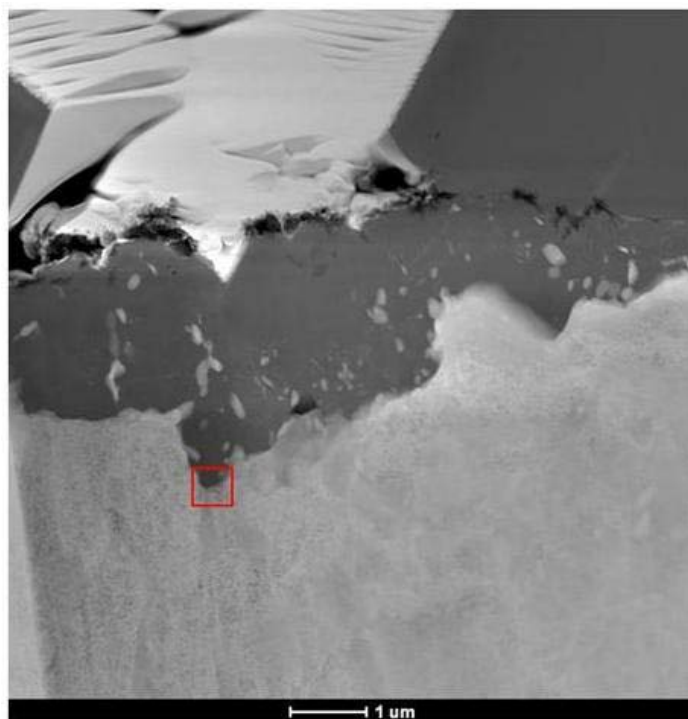


Figure 65. TEM analysis area of location 5 shown in Figure 56.

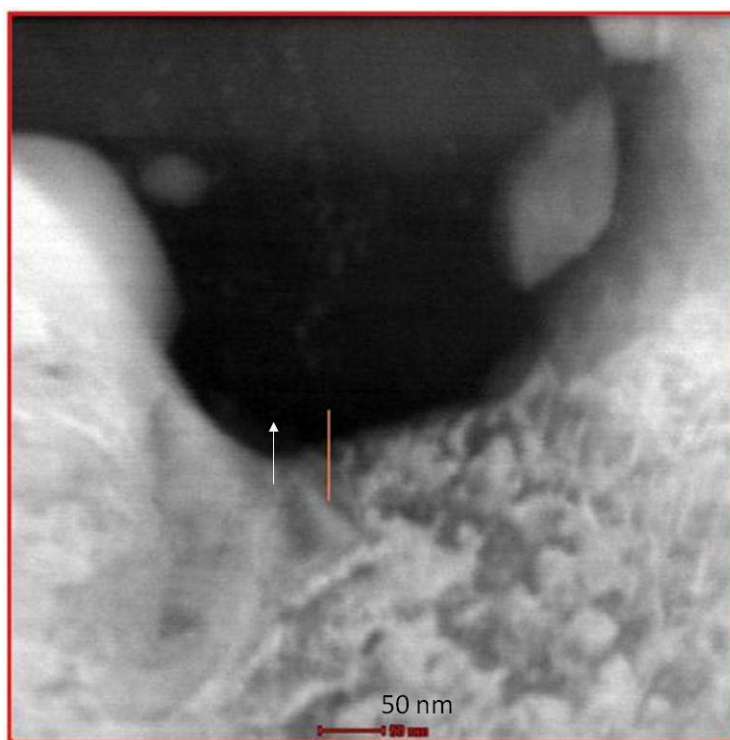


Figure 66. Zoomed in image of TEM analysis area at location 5 shown in Figure 56.

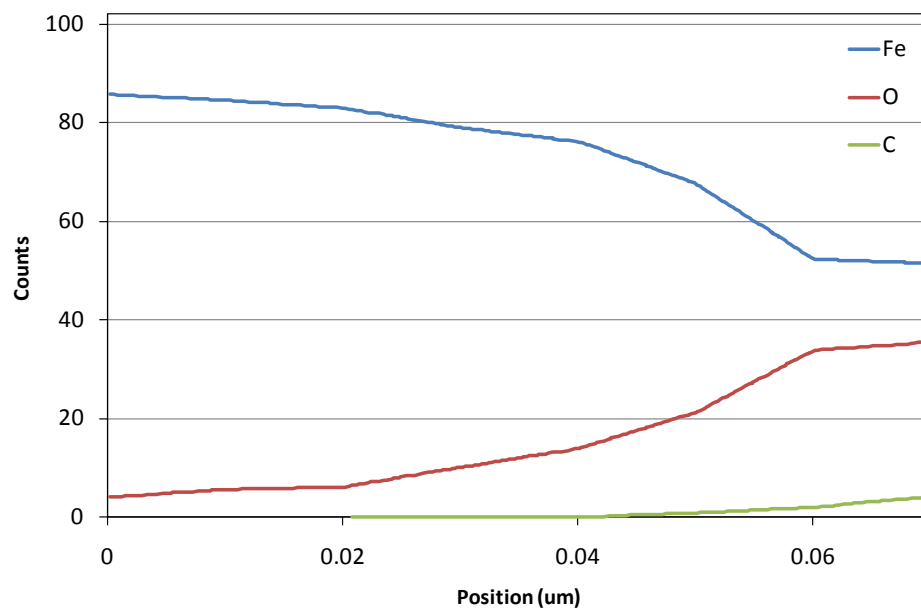


Figure 67. Line pattern EDS scan result of location 5 shown in Figure 66.



Figure 68. TEM analysis area of location 4 shown in Figure 56.

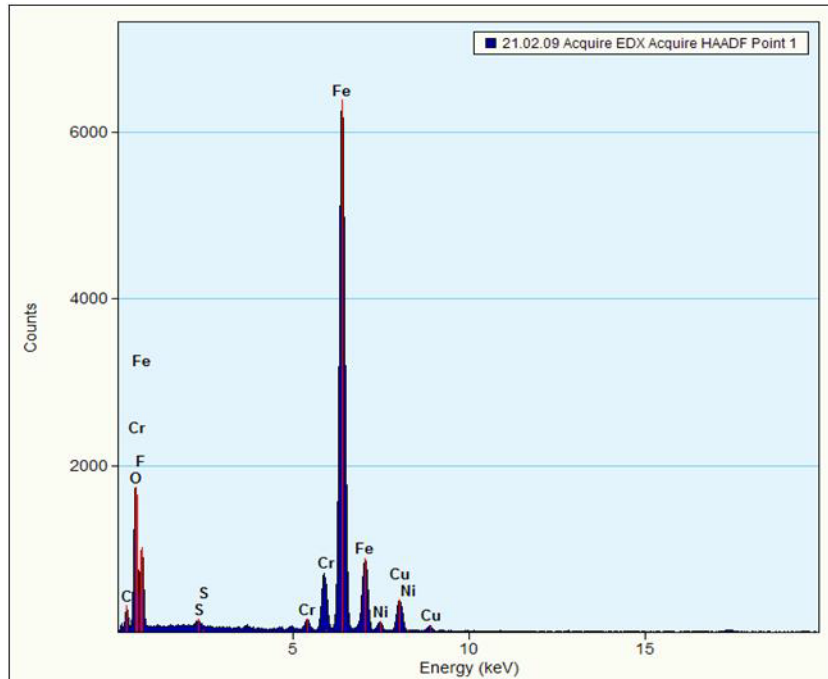


Figure 69. Point pattern EDS result of location 4 shown in Figure 68.

The results of electrochemical measurements and surface analysis indicated that a complete  $\text{FeCO}_3$  inner layer beneath the top layer on the carbon steel surface might be the only necessary component for pseudo-passive behavior. According to the TEM results, a dense and continuous  $\text{FeCO}_3$  formed on the steel surface at pH7.1 for the long term test. The correlation between the surface morphology and pseudo-passivation was also investigated. An anodic potentiodynamic polarization was carried out in the end of each test (short term, mid-term, long term) and the results are compared in Figure 70. From the figure, it clearly shows that with the increase of  $\text{FeCO}_3$  coverage, the layer has more protection effect, noted by significant corrosion current decrease, and, eventually, pseudo-passivation can be achieved. A plausible proposal for these observations is that the complete  $\text{FeCO}_3$  inner layer, along with other possible minor phases (iron oxides),

formed a protective layer on the steel surface, which accounts for this pseudo-passivation behavior.

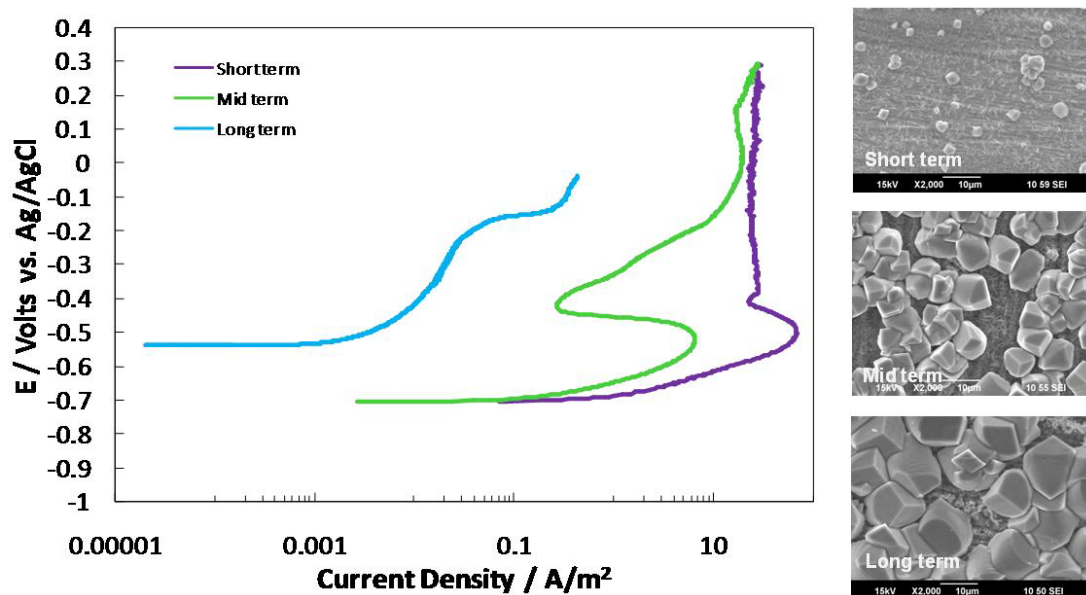


Figure 70. Anodic potentiodynamic polarization in the end of each test at pH 7.1 for short term, mid-term and long term tests and the corresponding surface morphology.

### 4.3.3 Tests at pH 6.6

With the pH lowered to 6.6, the  $\text{FeCO}_3$  saturation value is much smaller. Thus, the  $\text{FeCO}_3$  precipitation process is slowed down. In order to accelerate the formation of pseudo-passive layer, ferrous ions (50 ppm) were added into the test system at the beginning to maintain a high  $\text{FeCO}_3$  saturation value, a driving force of  $\text{FeCO}_3$  precipitation. The test conditions are listed in Table 8.

Figure 71 is the variation of open circuit potential with time and an approximate 50 mV potential increase is monitored. A significant corrosion rate decrease and an impedance increase also suggest pseudo-passivation might have been achieved (Figure 72 and Figure 73). Due to the relatively low  $\text{FeCO}_3$  saturation value, the dynamic process of  $\text{FeCO}_3$  precipitation was slower, which took approximately 3 days in this test before a protective layer formed.

The SEM image shows a different surface morphology compared to those tests previously described. A complete  $\text{FeCO}_3$  layer with the majority present with plate-like morphology (Figure 74) was observed. SEM-EDS confirmed the presence of  $\text{FeCO}_3$  (Figure 75).

In this test,  $\text{FeCO}_3$  was still able to confer good protection to the steel surface and showed a pseudo-passive behavior. At this point, it is assumed that a complete  $\text{FeCO}_3$  coverage accounted for this protection.

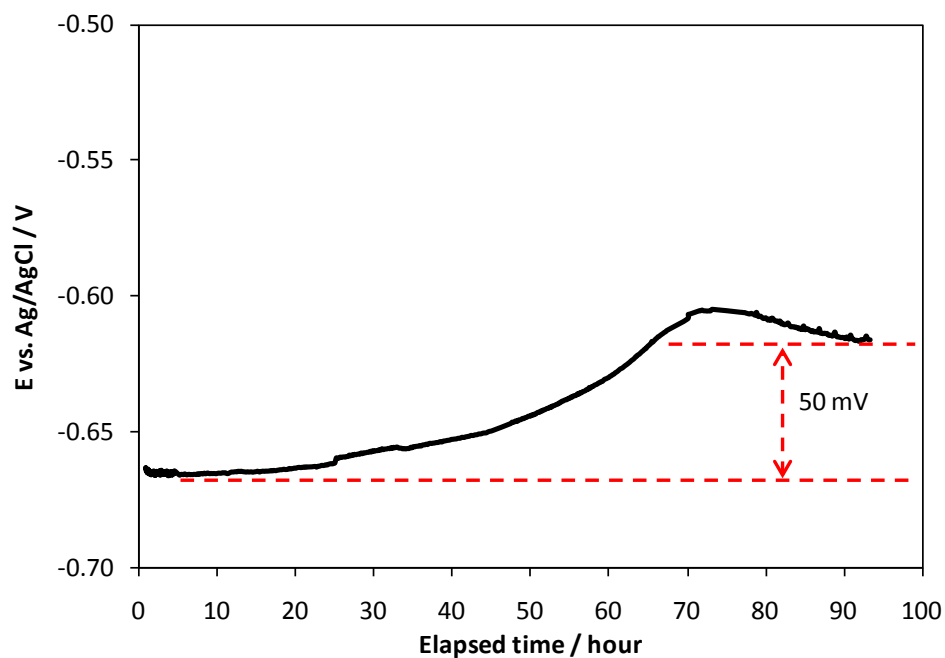


Figure 71. Open circuit potential during the test, 80°C, 0.53 bar CO<sub>2</sub>, 1 wt.% NaCl, stagnant, pH 6.6, initial [Fe<sup>2+</sup>] = 50 ppm. (SEM image of the sample is shown in Figure 74)

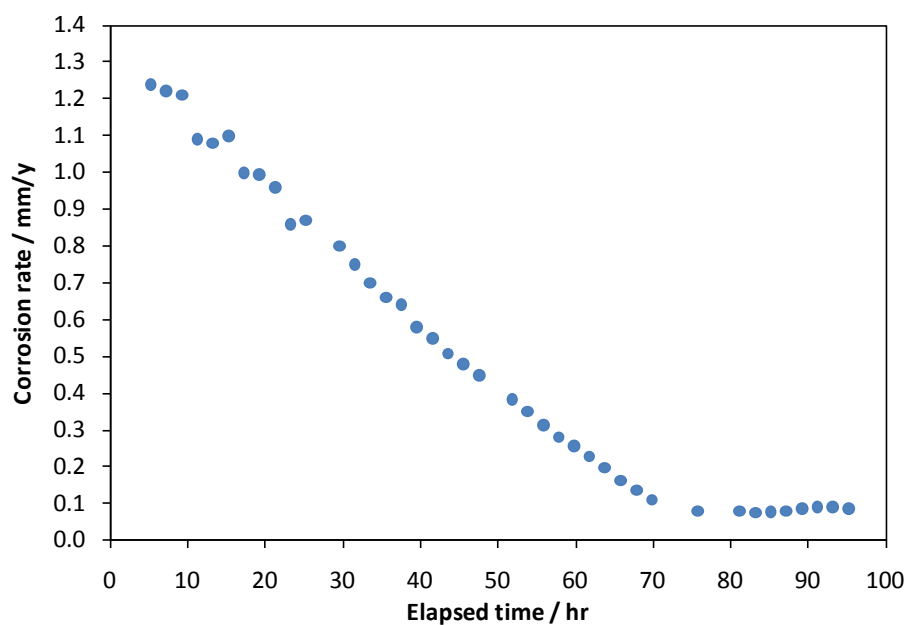


Figure 72. LPR corrosion rates during the test, 80°C, 0.53 bar CO<sub>2</sub>, 1 wt.% NaCl, initial [Fe<sup>2+</sup>] = 50 ppm, stagnant, pH 6.6. (SEM image of the sample is shown in Figure 74)

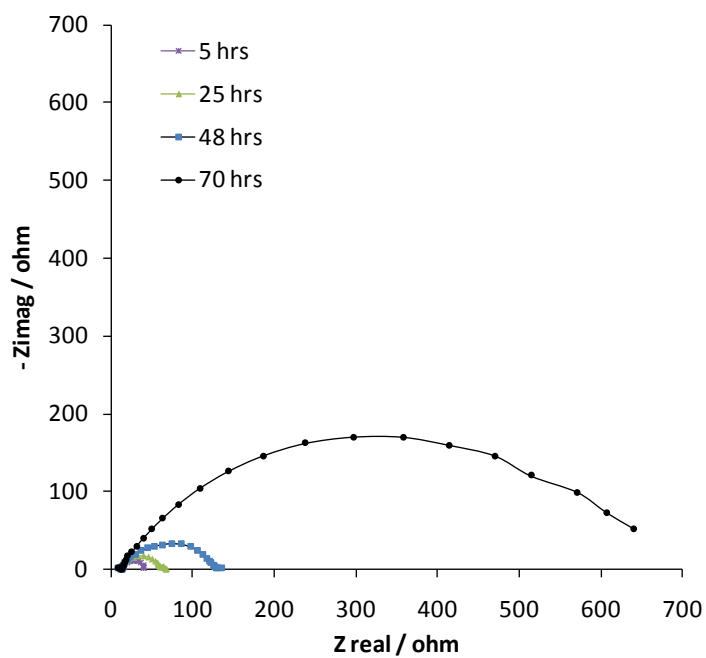


Figure 73. Comparison of the Nyquist plots during the test. 80°C, 0.53 bar CO<sub>2</sub>, 1 wt.% NaCl, stagnant, pH 6.6, initial [Fe<sup>2+</sup>] = 50 ppm.

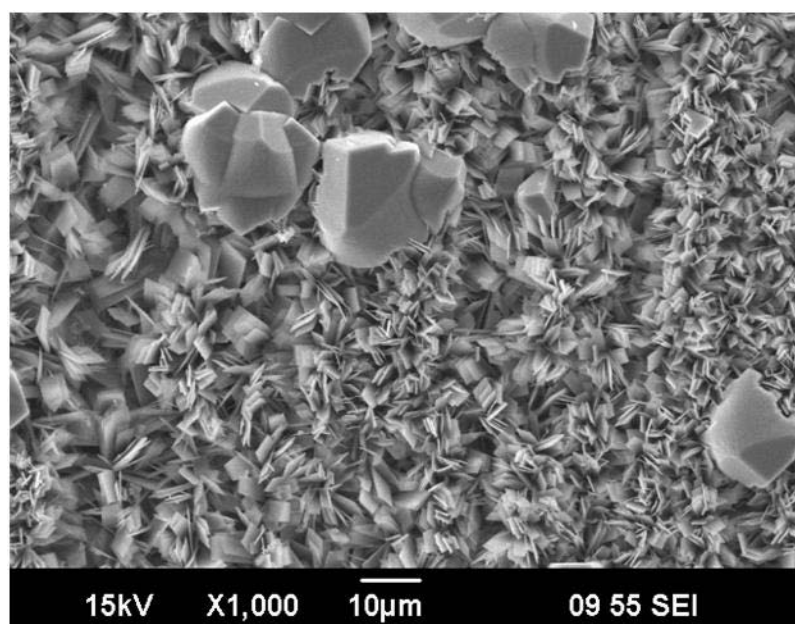


Figure 74. SEM image of X65 flat sample after test, 80°C, 0.53 bar CO<sub>2</sub>, 1 wt.% NaCl, stagnant, pH 6.6, initial [Fe<sup>2+</sup>] = 50 ppm. (LPR corrosion rate is shown in Figure 72)

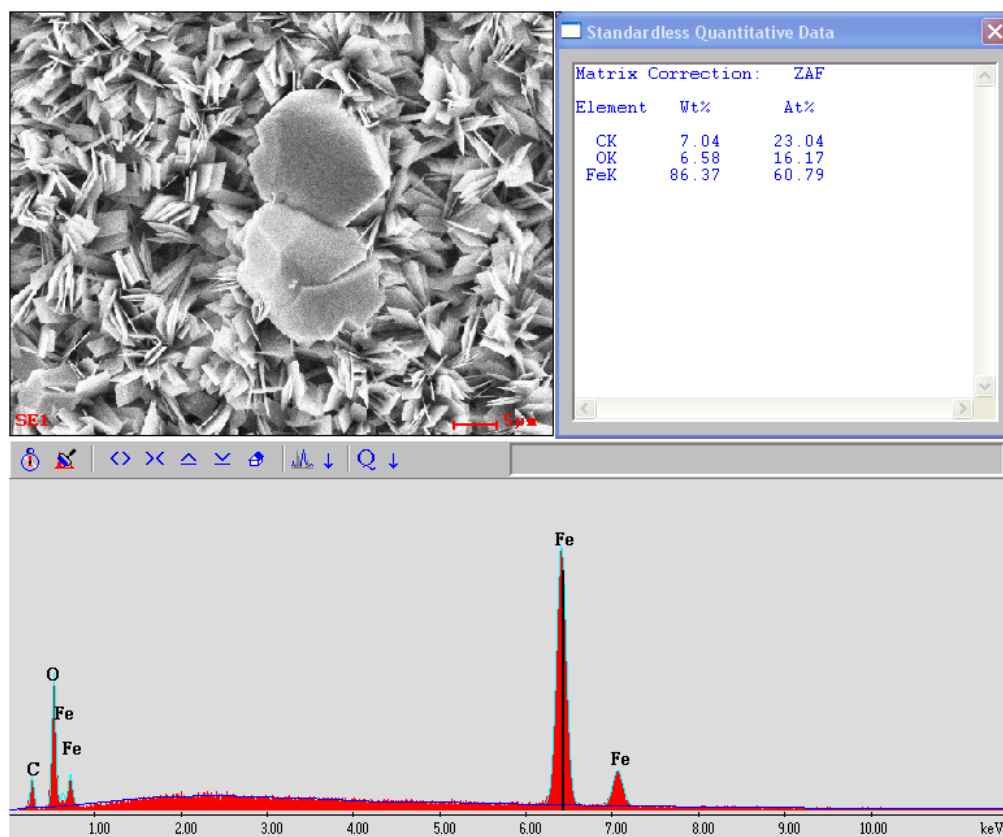


Figure 75. SEM-EDS result of X65 flat sample after test. 80°C, 0.53 bar CO<sub>2</sub>, 1 wt.% NaCl, stagnant, pH 6.6, initial [Fe<sup>2+</sup>] = 50 ppm.  
(LPR corrosion rate is shown in Figure 72)

#### 4.3.4 Tests at pH 6.0

Following the test sequences, pH was lowered to 6.0 for this test. From the saturation calculation, at this pH with no additional ferrous ion source,  $\text{FeCO}_3$  is under saturated. In order to form a  $\text{FeCO}_3$  layer, 100 ppm  $[\text{Fe}^{2+}]$  as  $\text{FeCl}_2$  solution was initially added to achieve saturation. In this test system, maintaining a  $\text{FeCO}_3$  saturated solution value was a key issue, thus  $[\text{Fe}^{2+}]$  was monitored during the entire test.

The variations of open circuit potential and corrosion rate with time are plotted in Figure 76. A notable open circuit potential increase occurs concurrently with corrosion rate decrease after 6 days of this test. A significant impedance increase was monitored by EIS (Figure 77). Warburg impedance can be seen for data taken after 6 days in the Nyquist plot, which indicates a diffusion barrier formed. This is assumed to be a pseudo-passive layer. This is in good agreement with the  $\text{FeCO}_3$  saturation calculation that with lower pH, it takes longer time for the  $\text{FeCO}_3$  precipitation process to occur. From the  $[\text{Fe}^{2+}]$  measurements, a decrease of  $[\text{Fe}^{2+}]$  was observed, which might be due to the consumption of  $[\text{Fe}^{2+}]$  during the  $\text{FeCO}_3$  precipitation.

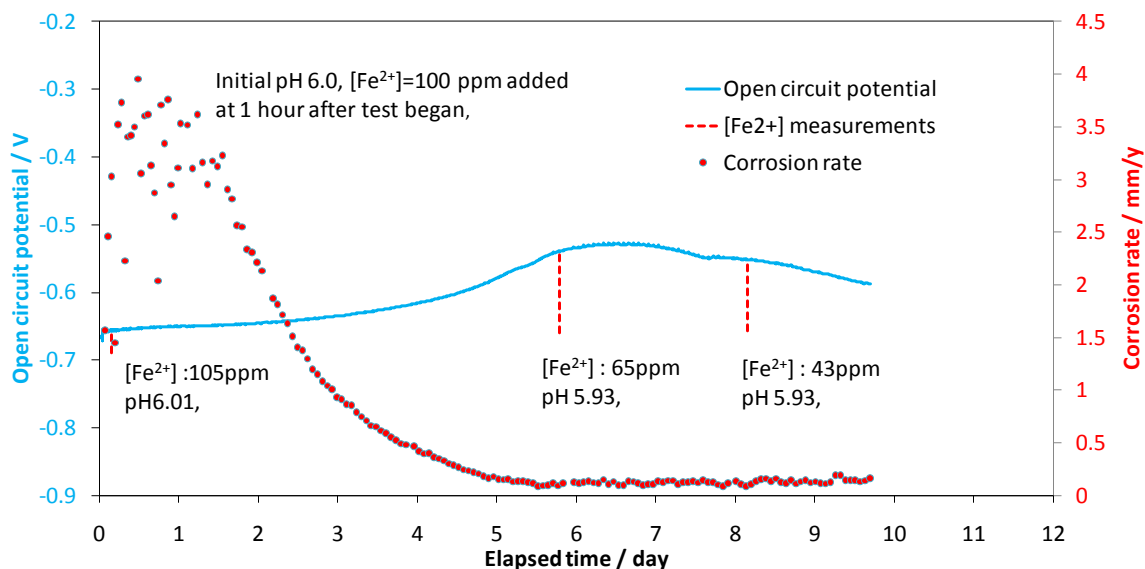


Figure 76. Variations of open circuit potential and corrosion rate with time. 80°C, 0.53 bar CO<sub>2</sub>, 1 wt.% NaCl, stagnant, pH 6.0, initial [Fe<sup>2+</sup>] = 100 ppm. (SEM image of the sample is shown in Figure 78)

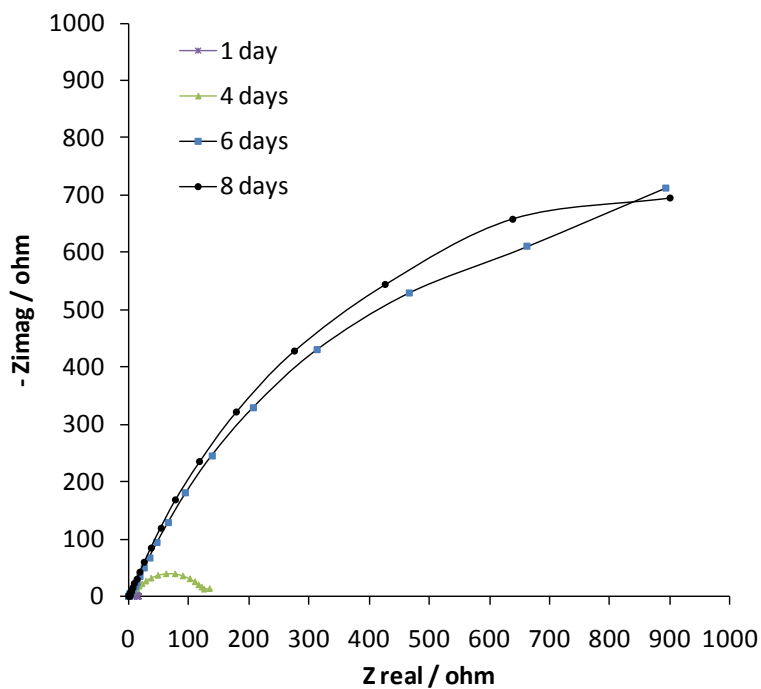


Figure 77. Comparison of the Nyquist plots during the test. 80°C, 0.53 bar CO<sub>2</sub>, 1 wt.% NaCl, stagnant, pH 6.0, initial [Fe<sup>2+</sup>] = 100 ppm.

When the protective layer formed, two flat X-65 samples were taken out from test solution after 6 days and 8 days of the test, respectively, for surface analysis. From Figure 78, the surfaces do not have significant differences. Two distinctive morphologies can be seen in both of these samples. On the surface, some locations were covered with  $\text{FeCO}_3$  and others seemed uncovered with corrosion product. EDS suggests that the surface was covered with  $\text{FeCO}_3$  (Figure 79). The cylindrical sample was taken out after day 10 of this test and was examined by SEM. Figure 80 shows the surface morphology of the cylindrical sample. No significant difference of surface morphology was found between cylindrical sample and flat sample. Due to the protection to the carbon steel, a complete  $\text{FeCO}_3$  layer was expected to exist on the steel surface. A cross-section SEM analysis of this cylindrical sample was carried out in order to verify this assumption. Figure 81 shows the image of this cross-section. Three distinctive phases can be seen in those images. The chemical compositions were identified as Fe,  $\text{FeCO}_3$  and carbon (epoxy) by EDS (Figure 82, Figure 83 and Figure 84). The detection of gold in the EDS spectra is due to the coating of gold in the SEM cross-section sample preparation. XRD was also employed to characterize the materials on the flat samples (work done at Ohio University). From the pattern (Figure 85), Fe,  $\text{FeCO}_3$  and  $\text{Fe}_2\text{CO}_3(\text{OH})_2$  can be identified; and  $\text{FeCO}_3$  is the quantitatively dominant phase on the steel surface. Cross-section and XRD analysis proved the validity of the previous assumption that a complete  $\text{FeCO}_3$  layer (approximately 5-10  $\mu\text{m}$ ) existed and provided protection to the carbon steel surface.

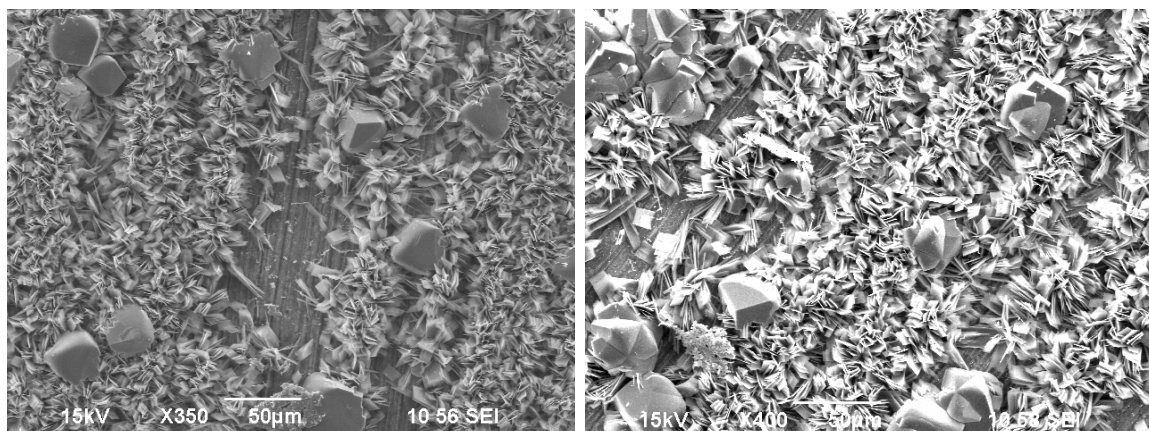


Figure 78. SEM images of X65 flat sample. 80°C, 0.53 bar CO<sub>2</sub>, 1 wt.% NaCl, stagnant, pH 6.0, initial [Fe<sup>2+</sup>] = 100 ppm. Left: 6 days of test; right: 8 days of the test. (LPR corrosion rate is shown in Figure 76)

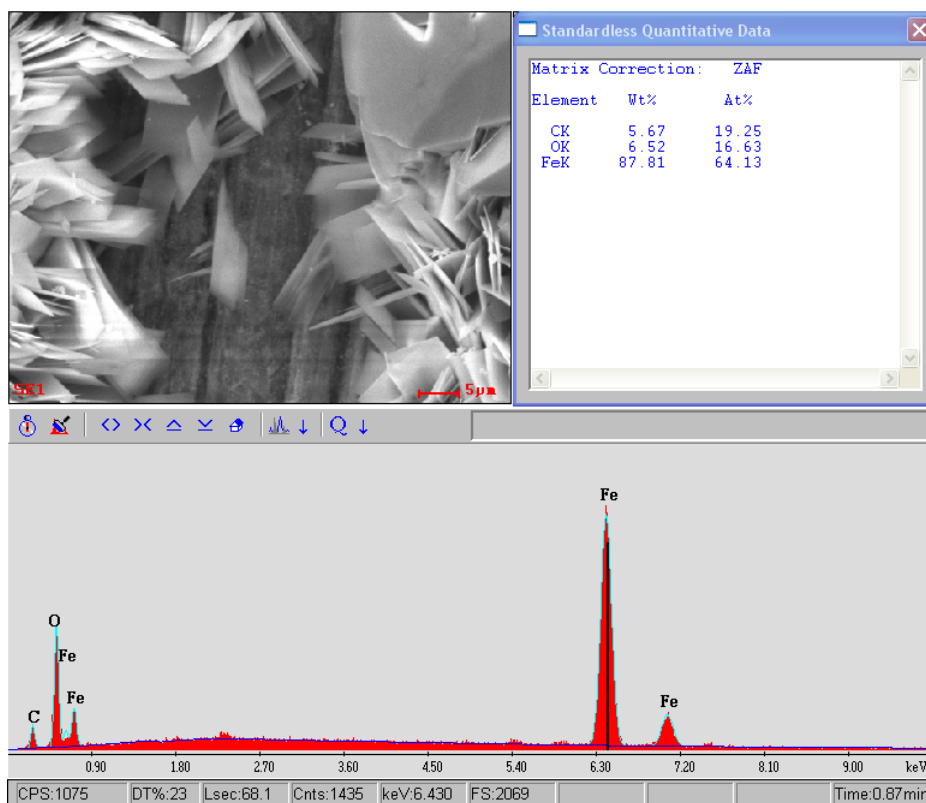


Figure 79. SEM-EDS data, X65 flat sample, 6 days of the test. 80°C, 0.53 bar CO<sub>2</sub>, 1 wt.% NaCl, stagnant, pH 6.0, initial [Fe<sup>2+</sup>] = 100 ppm. (LPR corrosion rate is shown in Figure 76)

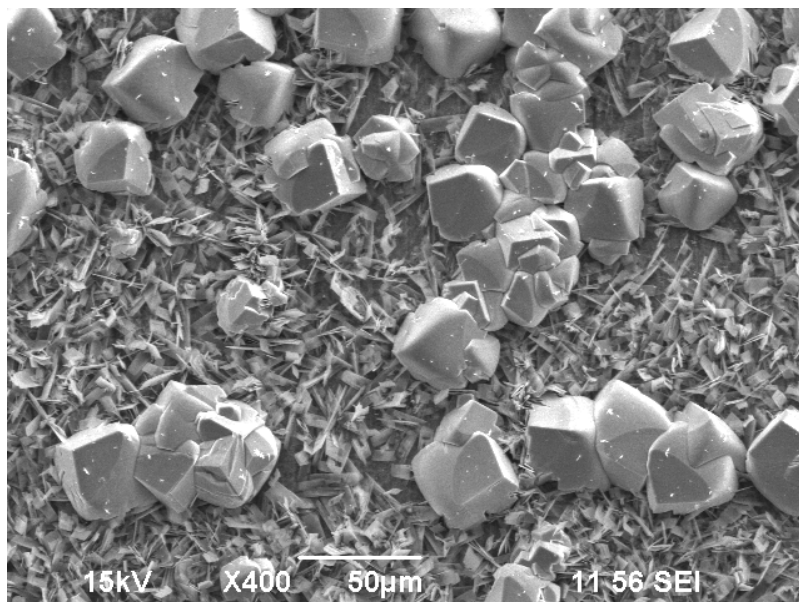


Figure 80. SEM image, X65 cylindrical sample. 80°C, 0.53 bar CO<sub>2</sub>, 1 wt.% NaCl, stagnant, pH 6.0, initial [Fe<sup>2+</sup>] = 100 ppm, 10 days of the test. (LPR corrosion rate is shown in Figure 76)

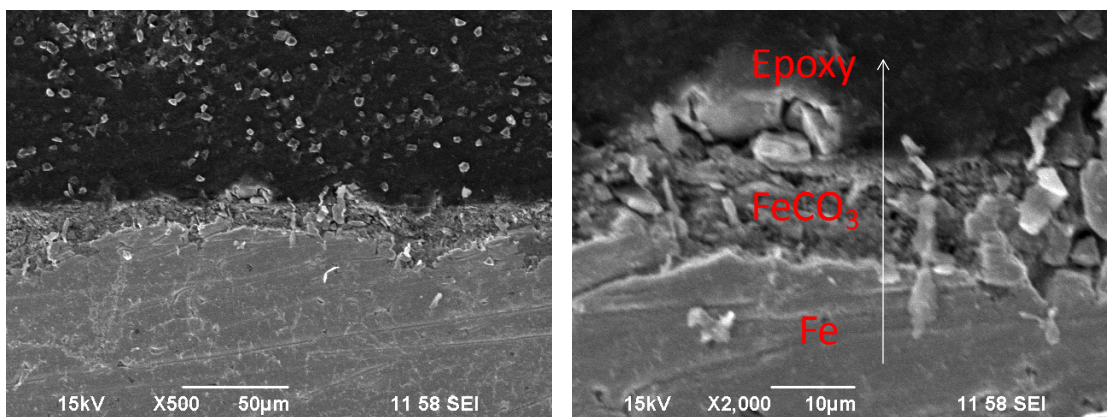


Figure 81. SEM images of X65 cylindrical sample cross-section. 80°C, 0.53 bar CO<sub>2</sub>, 1 wt.% NaCl, stagnant, pH 6.0, initial [Fe<sup>2+</sup>] = 100 ppm, 10 days of the test. Left: 500 magnification; Right: 2000 magnification. (LPR corrosion rate is shown in Figure 76)

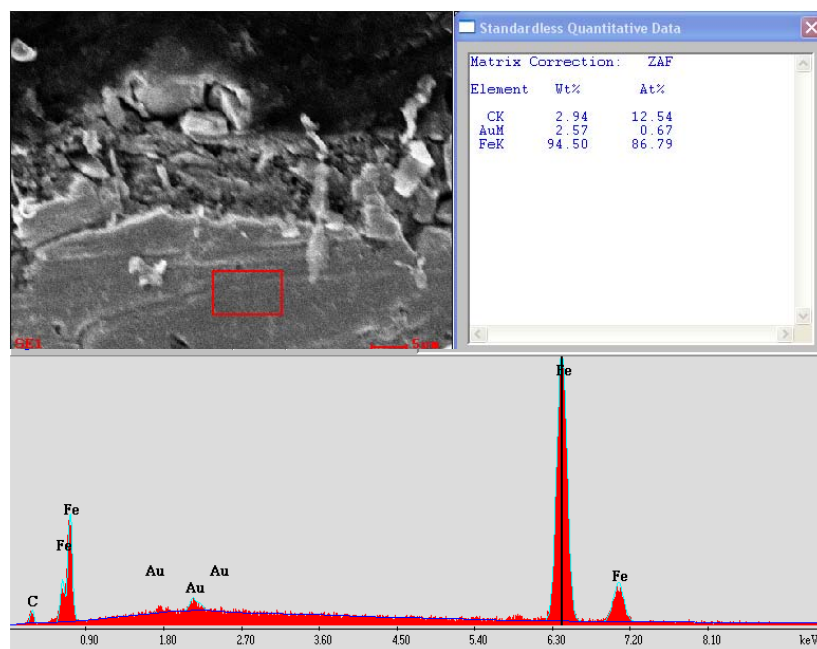


Figure 82. SEM-EDS data of Fe substrate, X65 sample, 80°C, 0.53 bar CO<sub>2</sub>, 1 wt.% NaCl, stagnant, pH 6.0, initial [Fe<sup>2+</sup>] = 100 ppm, 10 days of the test. (LPR corrosion rate is shown in Figure 76)

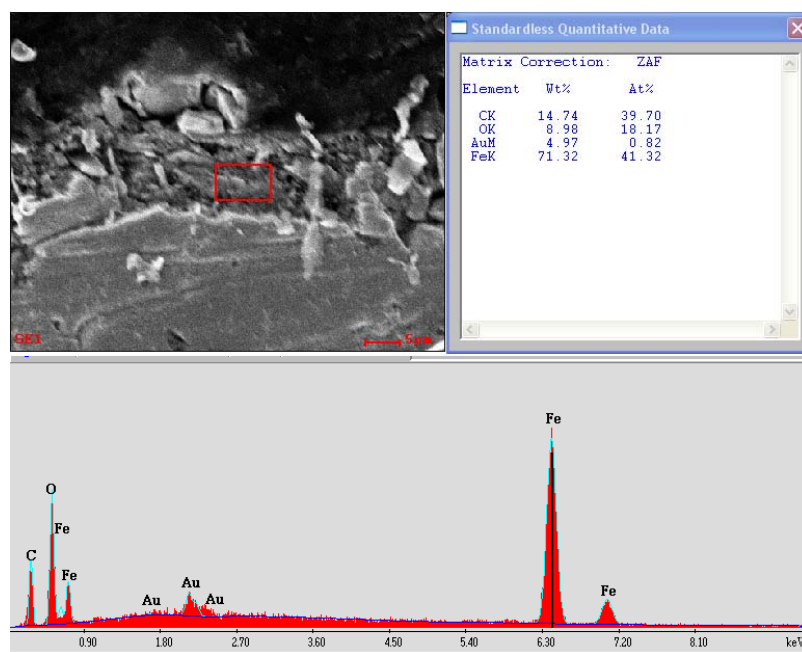


Figure 83. SEM-EDS data of FeCO<sub>3</sub> layer, X65 sample, 80°C, 0.53 bar CO<sub>2</sub>, 1 wt.% NaCl, stagnant, pH 6.0, initial [Fe<sup>2+</sup>] = 100 ppm, 10 days of the test. (LPR corrosion rate is shown in Figure 76)

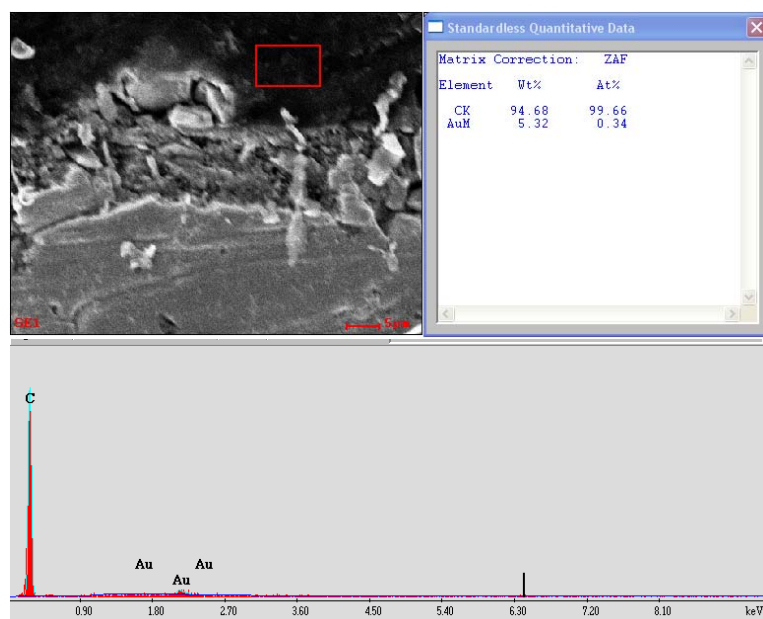


Figure 84. SEM-EDS data of epoxy layer.  
(LPR corrosion rate is shown in Figure 76)

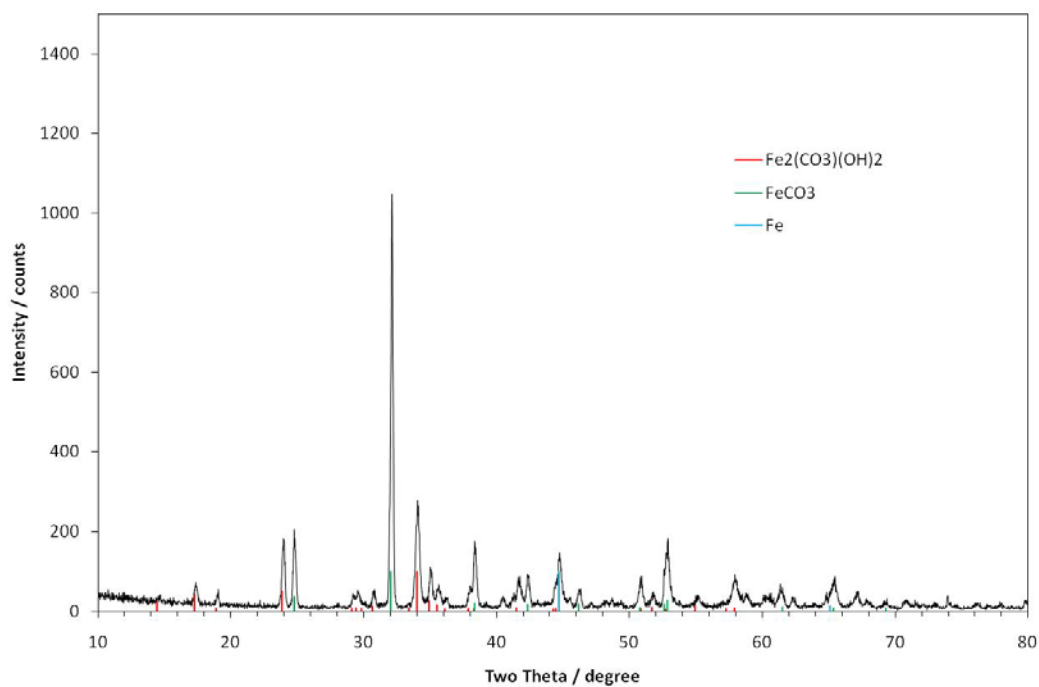


Figure 85. XRD pattern of X65 flat sample, day 8 of test. 80°C, 0.53 bar CO<sub>2</sub>, 1 wt.% NaCl, stagnant, pH 6.0, initial [Fe<sup>2+</sup>] = 100 ppm.  
(LPR corrosion rate is shown in Figure 76)

#### 4.3.5 Tests at pH 5.6

In this test, a pH 5.6, 1000 ppm initial  $[\text{Fe}^{2+}]$  system was studied. This relatively extreme test conditions was used to investigate if pseudo-passive layer could form at this pH value with a relatively high  $\text{FeCO}_3$  saturation value. The pH was initially maintained at 6.0. After adding 1000 ppm  $[\text{Fe}^{2+}]$ , the pH spontaneously dropped to 5.6 within one day. The pH was then maintained at 5.6 by minute additions of  $\text{NaHCO}_3$  powder.

In Figure 86, open circuit potential and corrosion rate variations *versus* time are plotted. In the test, ferrous ion concentration was monitored. The specific times at which  $[\text{Fe}^{2+}]$  was measured, are marked by green vertical dotted lines in Figure 86. The corrosion rate halved after initial addition of ferrous ion, from 1.2 mm/y to 0.6 mm/y. In the first 13 days of this test, both open circuit potential and corrosion rate were unstable due to the constant adjustment of pH. Open circuit potential had a slight increase (approximately 30 mV), and corrosion rate decreased to 0.3 mm/y. After 13 days, without any notable sign of achieving pseudo-passivation, more ferrous ion was added into the system, to a level of 1400 ppm. From day 14 through day 18, the corrosion rate lowered to 0.1 mm/y and the system was more stable. Another 50 mV potential increase was observed, this might be in response to the second addition of  $[\text{Fe}^{2+}]$  rather than, a sign of pseudo-passivation. Between day 18 and 22, a significant corrosion rate increase was observed. By day 22, the corrosion rate was 1.2 mm/y, the same level as that in the initial stage of this test. Simultaneously, the open circuit potential dropped to approximately -620 mV, which was identical to the potential at the beginning of the tests. All of these observations indicate that the protective layer failed completely during this period.

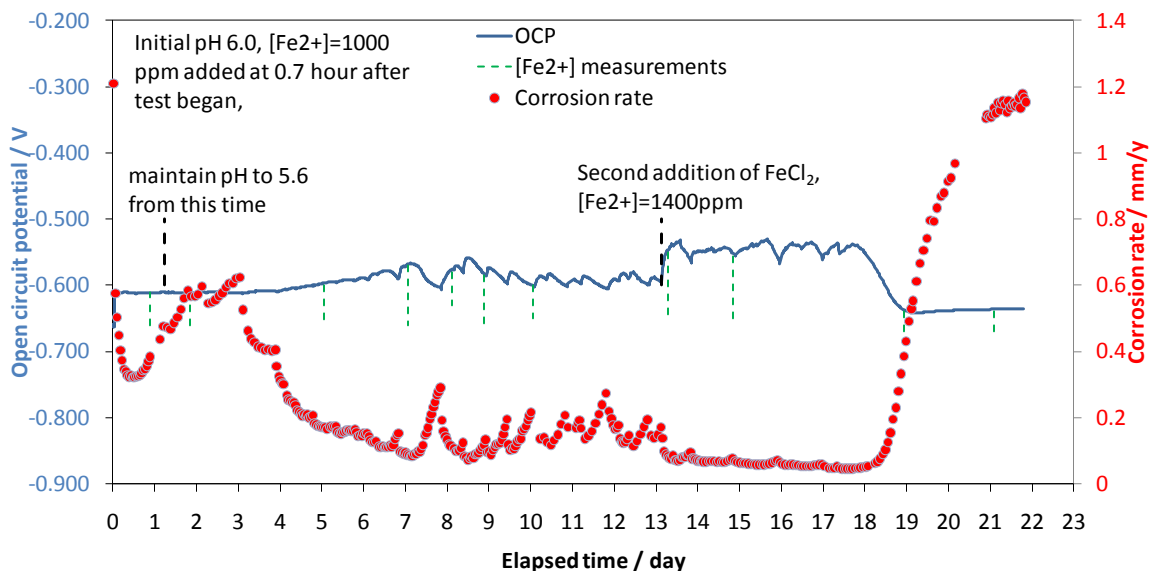


Figure 86. Variations of open circuit potential and corrosion rate with time. 80°C, 0.53 bar CO<sub>2</sub>, 1 wt.% NaCl, stagnant, pH 5.6, initial [Fe<sup>2+</sup>] = 1000 ppm. (SEM image of the sample is shown in Figure 90)

By examining the ferrous ion concentration variations with time, a trend of [Fe<sup>2+</sup>] decrease in the solution can be seen for the time period after each ferrous ion addition (Figure 87 and Figure 88). Although this could be an indication of FeCO<sub>3</sub> precipitation in the system, no protective layer formed on the steel surface after 22 days of the test. From Figure 89, it can be seen that FeCO<sub>3</sub> had precipitated in the glass cell. However, it was not a favorable condition for the formation of pseudo-passivation on the steel according to the electrochemical measurements.

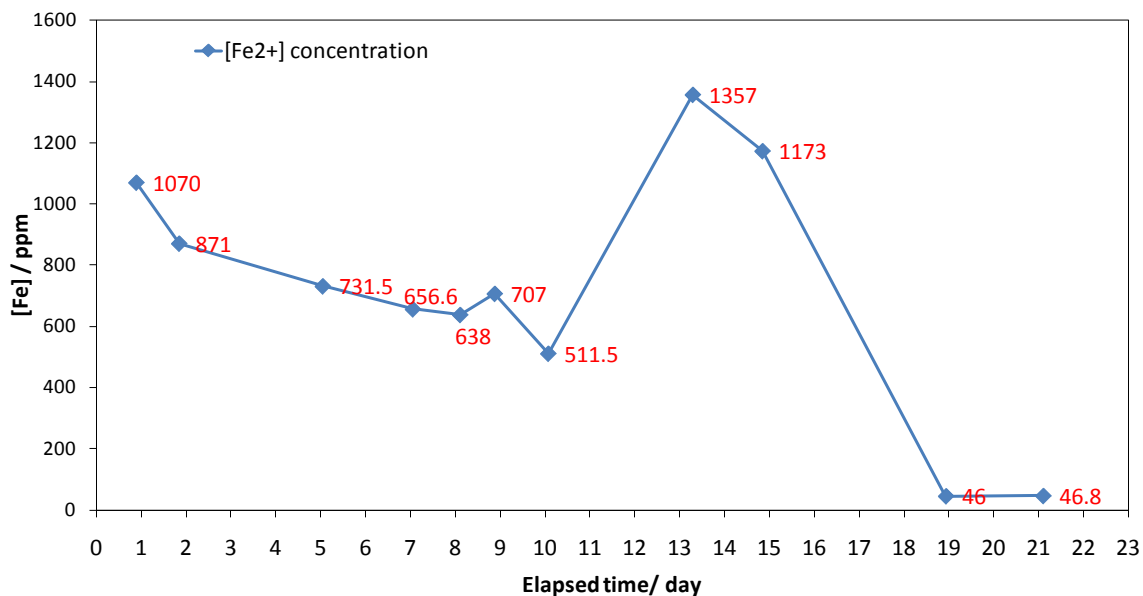


Figure 87. [Fe<sup>2+</sup>] variations with time. 80°C, 0.53 bar CO<sub>2</sub>, 1 wt.% NaCl, stagnant, pH 5.6, initial [Fe<sup>2+</sup>] = 1000 ppm.

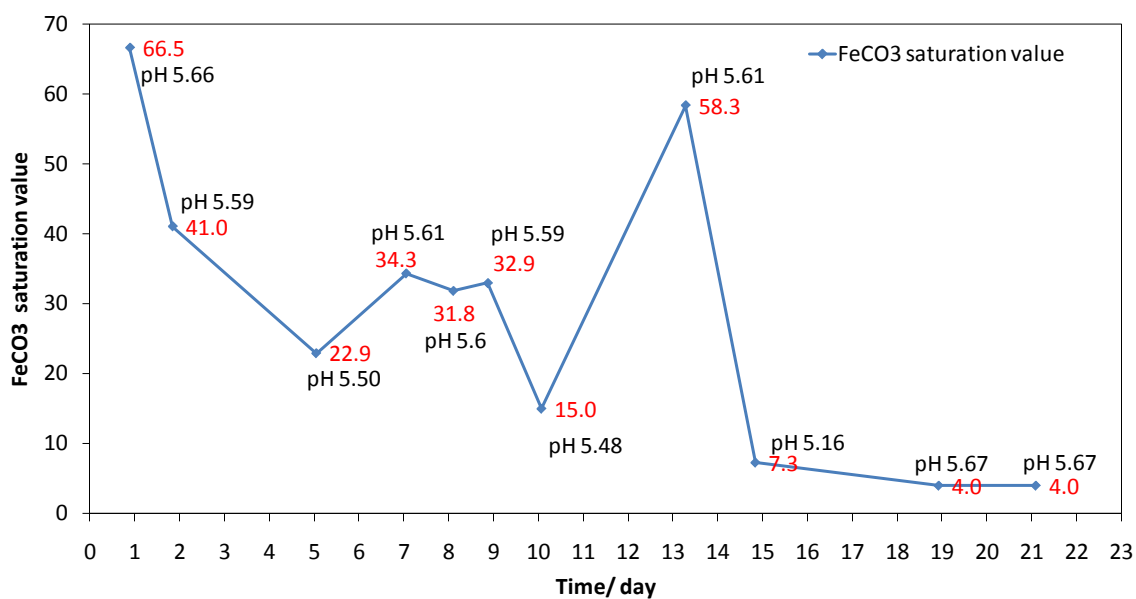


Figure 88. FeCO<sub>3</sub> saturation value variations with time. 80°C, 0.53 bar CO<sub>2</sub>, 1 wt.% NaCl, stagnant, pH 5.6, initial [Fe<sup>2+</sup>] = 1000 ppm.

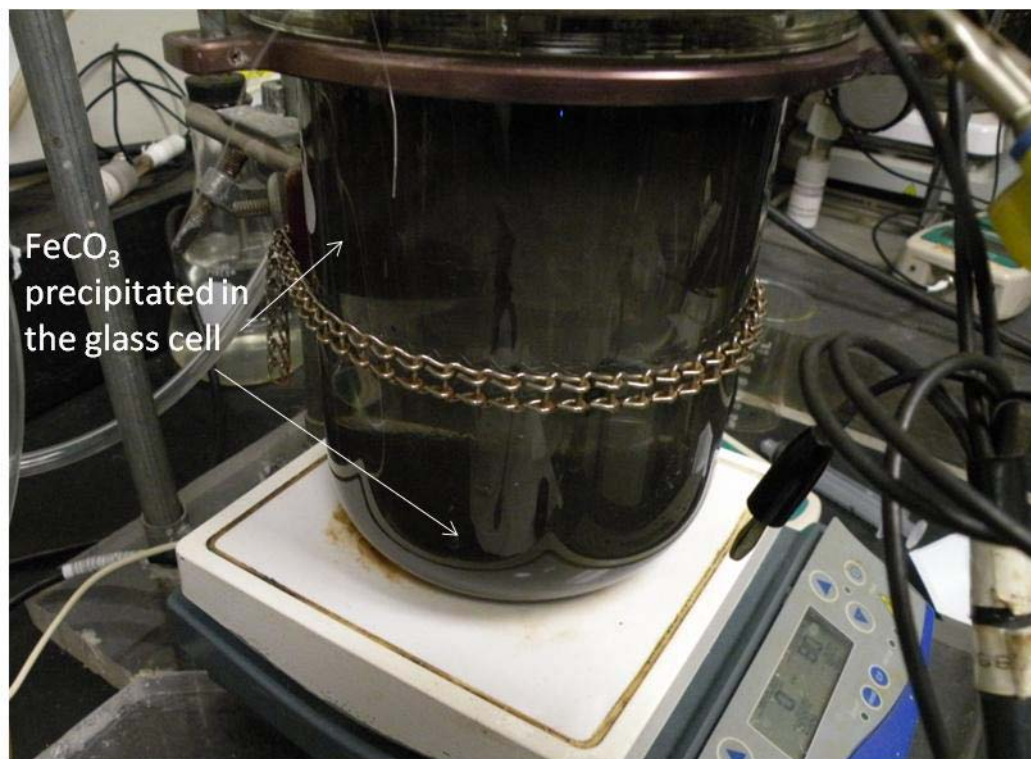


Figure 89. Picture of test cell taken after 22 days of the test. 80°C, 0.53 bar CO<sub>2</sub>, 1 wt.% NaCl, stagnant, pH 5.6, initial [Fe<sup>2+</sup>] = 1000 ppm.

Figure 90 shows the surface morphology of the steel sample after the test. FeCO<sub>3</sub> can be seen in these images and dissolution and collapse of previously precipitated FeCO<sub>3</sub> layer can also be found, which suggests the competition between FeCO<sub>3</sub> dissolution and precipitation was severe in this test. According to this incomplete coverage of FeCO<sub>3</sub>, no protection is expected. This agrees well with previous electrochemical observations. A cross-section SEM of the cylindrical sample was done after the test. The SEM images shown in Figure 91 indicate that the surface is barely covered with FeCO<sub>3</sub>, with no coverage at all at some locations. This observation is also supported by EDS analyses (Figure 92, Figure 93 and Figure 94). XRD (work done at Ohio University) data shown in Figure 95 indicates that iron is the majority phase on the

surface. Consequently, insufficient  $\text{FeCO}_3$  was present to cover and effectively protect the steel surface. It is noteworthy that  $\text{Fe}_2\text{CO}_3(\text{OH})_2$  was again observed during this test and likely corresponded to the thin, plate-like crystals presenting on the surface.

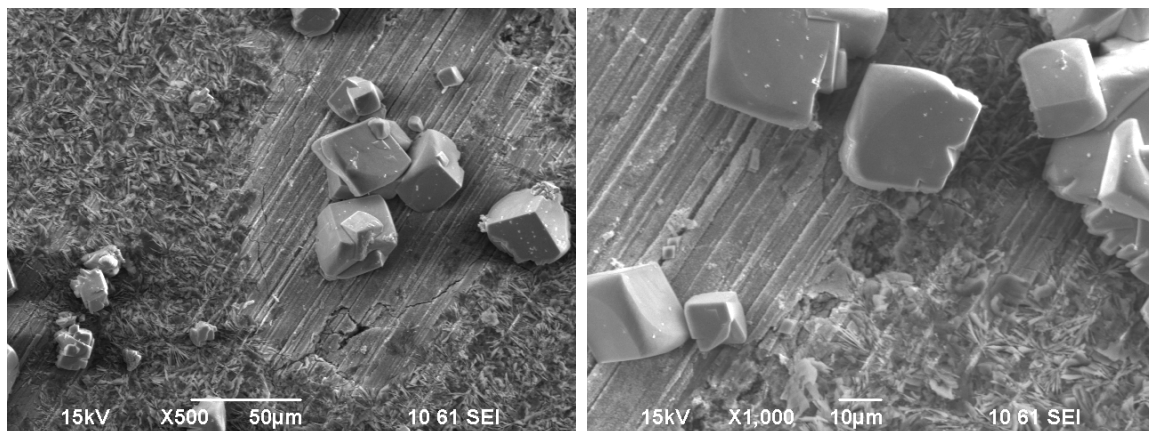


Figure 90. SEM images of X65 cylindrical sample.  $80^\circ\text{C}$ , 0.53 bar  $\text{CO}_2$ , 1 wt.% NaCl, stagnant, pH 5.6, initial  $[\text{Fe}^{2+}] = 1000$  ppm, 22 days of the test. Left: 500 magnification; Right: 1000 magnification. (LPR corrosion rate is shown in Figure 86)

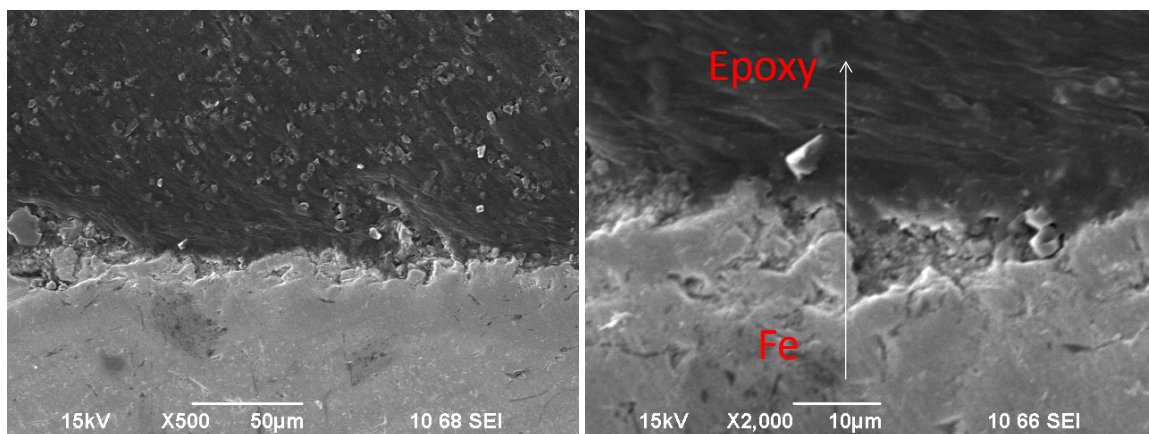


Figure 91. SEM images of X65 cylindrical sample cross-section.  $80^\circ\text{C}$ , 0.53 bar  $\text{CO}_2$ , 1 wt.% NaCl, stagnant, pH 5.6, initial  $[\text{Fe}^{2+}] = 1000$  ppm, 22 days of the test. Left: 500 magnification; Right: 2000 magnification. (LPR corrosion rate is shown in Figure 86)

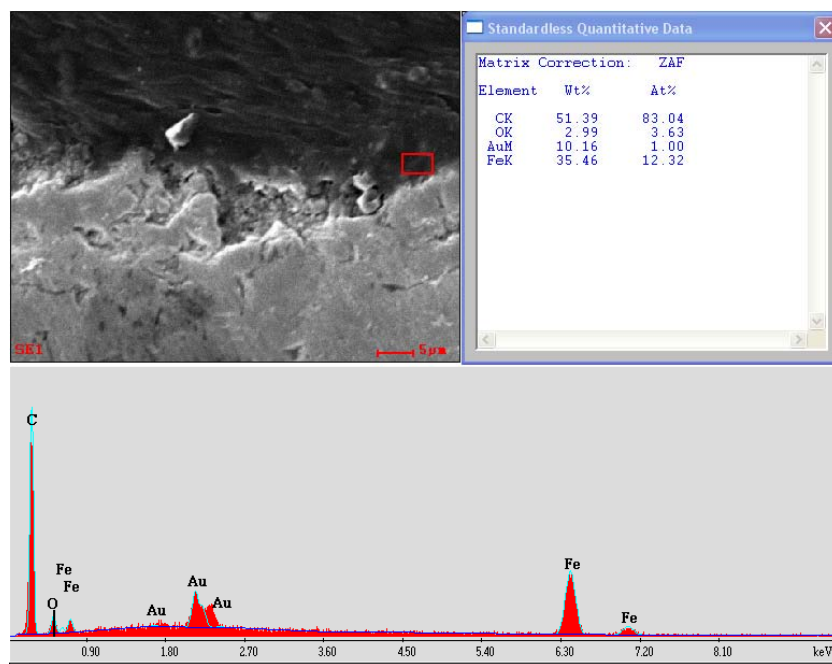


Figure 92. SEM-EDS data of epoxy, X65 cylindrical sample cross-section. (LPR corrosion rate is shown in Figure 86)

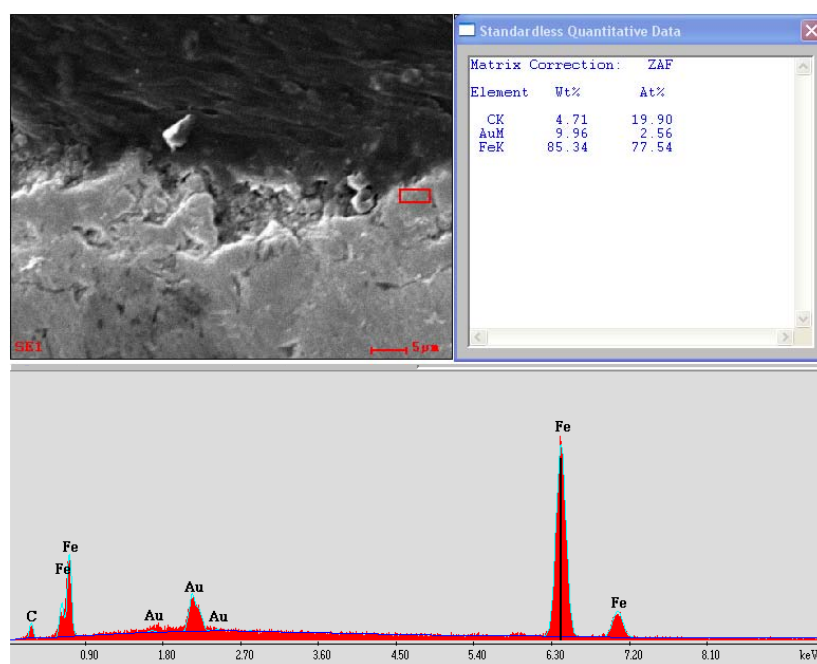


Figure 93. SEM-EDS data of Fe substrate, X65 cylindrical sample cross-section. (LPR corrosion rate is shown in Figure 86)

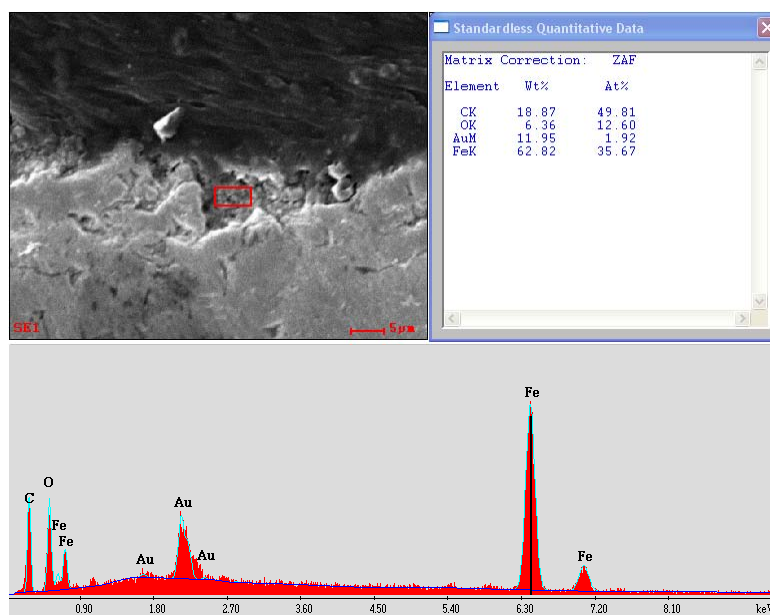


Figure 94. SEM-EDS data of  $\text{FeCO}_3$ , X65 cylindrical sample cross-section. (LPR corrosion rate is shown in Figure 86)

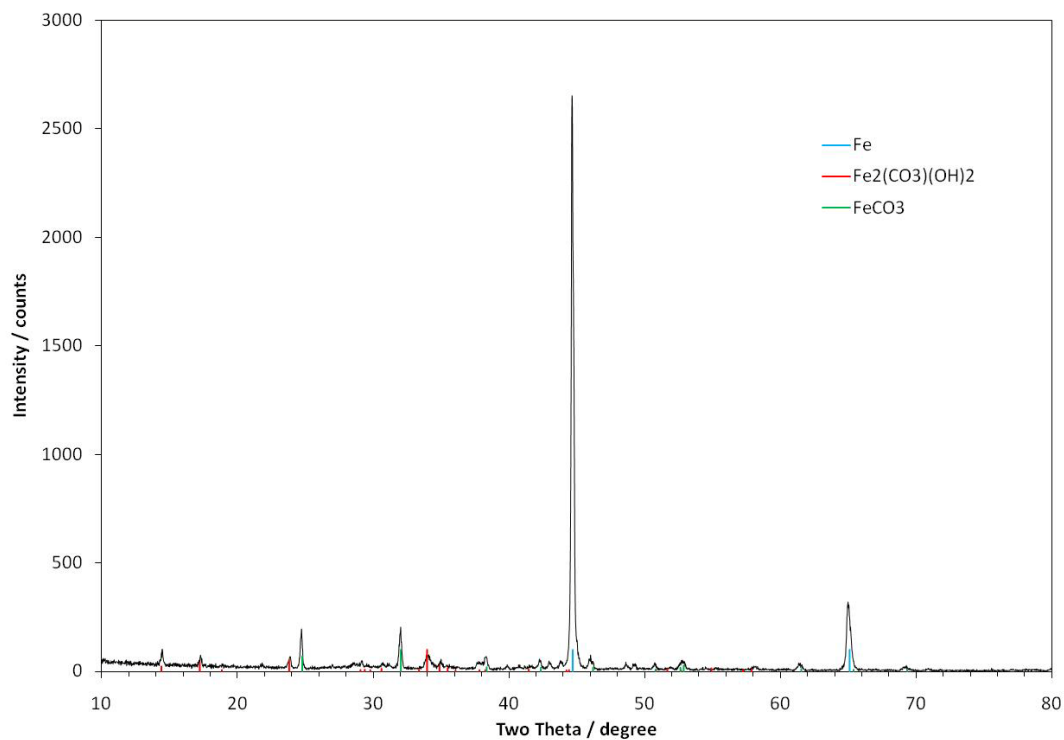


Figure 95. XRD pattern of X65 flat sample, day 22 of test.  $80^\circ\text{C}$ , 0.53 bar  $\text{CO}_2$ , 1 wt.% NaCl, stagnant, pH 5.6, initial  $[\text{Fe}^{2+}] = 1000$  ppm. (LPR corrosion rate is shown in Figure 86)

According to electrochemical measurements and surface analyses, no pseudo-passivation was achieved at this test. Incomplete surface coverage by  $\text{FeCO}_3$  on the steel surface is likely the dominant factor that attributed to the failure of protection. The reason why no complete  $\text{FeCO}_3$  layer can be found on the steel surface with such high initial ferrous ion concentration might be due to the unfavorable precipitation condition at this relatively low pH.

#### 4.3.6 Discussion

Several corrosion systems at 80°C, 0.53bar CO<sub>2</sub> have been studied in a wide pH range from 7.8 to 5.6. A pseudo-passivation behavior accompanying a potential increase and decreased corrosion rate has been observed for tests at pH 7.8, 7.1, 6.6 and 6.0. For test at pH 5.6, no stable protective FeCO<sub>3</sub> layer had formed at a high initial concentration of ferrous ion.

Examining the samples of test samples revealed that a dense, continuous FeCO<sub>3</sub> inner layer that adheres to the steel surface could be the cause of corrosion protection. The morphology of FeCO<sub>3</sub> outer layer changes drastically from high pH to low pH. FeCO<sub>3</sub> prisms are the dominant at the steel surface for high pH conditions, while the majority of the FeCO<sub>3</sub> and Fe<sub>2</sub>CO<sub>3</sub>(OH)<sub>2</sub> has plate-like morphology at low pH. The plate-like crystals are believed to correspond to the initial form of FeCO<sub>3</sub> in CO<sub>2</sub> corrosion. The drastic morphology change is possibly due to the variation of FeCO<sub>3</sub> solubility with pH.

The reason why the potential increases with such layer remains under investigation. Trace amounts of iron oxides may exist in this layer and account for the positive shift of corrosion potential. Another possibility is that potential increase may be due to the reduced conductivity on the surface as a result of the complete coverage of FeCO<sub>3</sub>, which is a poor conductor.

## CHAPTER 5: CONCLUSIONS

Investigation of pseudo-passive layer formation in CO<sub>2</sub> corrosion in a pH range from 7.8 to 5.6 at elevated temperature has been conducted. A relatively new electrochemical technique, electrochemical frequency modulation, has been applied to this pseudo-passive layer study. The structure and chemical compositions of this layer have also been studied by materials characterization techniques. Based on the observations of this work, the following conclusions have been made:

- EFM provides instantaneous Tafel slopes and corrosion rate measurements. The EFM also introduces causality factors to corroborate the reliability of EFM measurements.
- EFM worked well in several mild steel/NaCl CO<sub>2</sub> un-inhibited and inhibited systems and gave reasonable agreement with other corrosion monitoring techniques. However, EFM was unsuitable for the study of CO<sub>2</sub> pseudo-passivation.
- EFM requires predetermined corrosion models for corrosion calculations, which reduces its applicability in corrosion systems with in advance unknown mechanisms.
- A pseudo-passive layer did form with a positive open circuit potential shift and a significantly retarded corrosion rate in the pH range from 7.8 to 6.0 at 80°C, 0.53 bar CO<sub>2</sub>.

- A continuous  $\text{FeCO}_3$  inner layer was observed when pseudo-passivation was achieved, which suggests complete surface coverage by this  $\text{FeCO}_3$  layer could be the main cause of pseudo-passivation.
- Plate-like crystals were observed at low pH tests and at the beginning of high pH tests. These plates are possibly  $\text{Fe}_2\text{CO}_3(\text{OH})_2$  and assumed to be the initial stage of  $\text{FeCO}_3$  layer formation.
- A stable and protective pseudo-passive layer could not be achieved at pH 5.6,  $80^\circ\text{C}$ , 0.53 bar  $\text{CO}_2$ , even with ferrous ion concentrations greater than 1000 ppm.
- Due to the increased solubility of  $\text{FeCO}_3$ , the approximate threshold pH value for the formation of pseudo-passive layer at  $80^\circ\text{C}$  and 0.53 bar  $\text{CO}_2$ , was determined to be 6.0.

## REFERENCES

- [1] Y. P. Virmani, "Corrosion costs and preventive strategies in the united states," Federal Highway Administration, U.S. Department of Transportation, Tech. Rep. FHWA-RD-01-156, 2002.
- [2] A. Dugstad, L. Lunde and S. Nešić, "Control of internal corrosion in multi-phase oil and gas pipelines," in *Prevention of Pipeline Corrosion Conference*, Marriott Houston Westside Hotel, Houston, Texas, USA, 1994.
- [3] L. S. Moiseeva, "Carbon dioxide corrosion of oil and gas field equipment," *Protection of Metals*, vol. 41, pp. 76-83, 2005.
- [4] C. De waard and D. E. Milliams, "Prediction of carbonic acid corrosion in natural gas pipelines." in *1st International Conference on the Internal and External Protection of Pipes*, University of Durham, UK, 1975.
- [5] G. Schmitt and B. Rothmann, "Corrosion Mechanism of Unalloyed Steel in Oxygen-Free Carbon Dioxide Solutions - 1. Kinetics of the Liberation of Hydrogen," *Werkst. Korros.*, vol. 28, pp. 816-822, 1977.
- [6] G. Schmitt and B. Rothmann, "Corrosion of Unalloyed and Low Alloyed Steels in Carbonic Acid Solutions." *Werkst. Korros.*, vol. 29, pp. 237-245, 1978.
- [7] L. G. S. Gray, B. G. Anderson, M. J. Danysh and P. R. Tremaine, "Mechanisms of carbon steel corrosion in brines containing dissolved carbon dioxide at pH 4," in *NACE Corrosion 89*, New Orleans Convention Center, New Orleans, Louisiana, USA, 1989.
- [8] L. G. S. Gray, B. G. Anderson, M. J. Danysh and P. R. Tremaine, "Effect of pH and temperature on the mechanism of carbon steel corrosion by aqueous carbon dioxide," in *NACE Corrosion 90*, Bally's Hotel, Las Vegas, Nevada, USA, 1990.
- [9] S. Nešić, J. Postlethwaite and S. Olsen, "An Electrochemical Model for Prediction of Corrosion of Mild Steel in Aqueous Carbon Dioxide Solutions," *Corrosion (Houston)*, vol. 52, pp. 280-294, 1996.
- [10] S. Nešić and K. -. J. Lee, "A mechanistic model for carbon dioxide corrosion of mild steel in the presence of protective iron carbonate films - Part 3: Film growth model," *Corrosion*, vol. 59, pp. 616-628, 2003.
- [11] S. Nešić, M. Nordsveen, R. Nyborg and A. Stangeland, "A mechanistic model for carbon dioxide corrosion of mild steel in the presence of protective iron carbonate films - Part 2: A numerical experiment," *Corrosion*, vol. 59, pp. 489-497, 2003.

- [12] M. Nordsveen, S. Nešić, R. Nyborg and A. Stangeland, "A mechanistic model for carbon dioxide corrosion of mild steel in the presence of protective iron carbonate films - Part 1: Theory and verification," *Corrosion*, vol. 59, pp. 443-456, 2003.
- [13] A. Dugstad, "Fundamental aspects of CO<sub>2</sub> metal loss corrosion part I: Mechanism," in *NACE - International Corrosion Conference Series*, 2006, pp. 061111-0611118.
- [14] G. Schmitt and M. Hörstemeier, "Fundamental aspects of CO<sub>2</sub> metal loss corrosion - Part II: Influence of different parameters on CO<sub>2</sub> corrosion mechanisms," *NACE - International Corrosion Conference Series*, pp. 061121-0611226, 2006.
- [15] T. Li, Y. Yang, K. Gao and M. Lu, "Mechanism of protective film formation during CO<sub>2</sub> corrosion of X65 pipeline steel," *Journal of University of Science and Technology Beijing*, vol. 15, pp. 702-706, 2008.
- [16] J. Han, B. N. Brown and S. Nešić, "Investigation of the galvanic mechanism for localized carbon dioxide corrosion propagation using the artificial pit technique," *Corrosion*, vol. 66, pp. 0950031-09500312, 2010.
- [17] S. Nešić, "Key issues related to modelling of internal corrosion of oil and gas pipelines – A review," *Corros. Sci.*, vol. 49, pp. 4308-4338, 2007.
- [18] S. Nešić and W. Sun, "Corrosion in acid gas solutions," in *Shreir's Corrosion*, Tony J.A. Richardson, Ed. Oxford: Elsevier, 2010, pp. 1270-1298.
- [19] Y. K. Kharaka and Geological Survey, *SOLMINEQ.88, a Computer Program for Geochemical Modeling of Water-Rock Interactions*. Menlo Park, Calif.: Dept. of the Interior, U.S. Geological Survey, 1989.
- [20] J. E. Oddo and M. B. Tomson, "Simplified calculation of CaCO<sub>3</sub> saturation at high temperatures and pressures in brine solutions." *Journal of Petroleum Technology*, vol. 34, pp. 1583-1590, 1982.
- [21] D. A. Palmer and R. Van Eldik, "The chemistry of metal carbonate and carbon dioxide complexes," *Chem. Rev.*, vol. 83, pp. 651-731, 1983.
- [22] W. Sun, S. Nešić and R. C. Woollam, "The effect of temperature and ionic strength on iron carbonate (FeCO<sub>3</sub>) solubility limit," *Corros. Sci.*, vol. 51, pp. 1273-1276, 2009.
- [23] C. Ding, K. Gao and C. Chen, "Effect of Ca<sup>2+</sup> on CO<sub>2</sub> corrosion properties of X65 pipeline steel," *International Journal of Minerals, Metallurgy and Materials*, vol. 16, pp. 661-666, 2009.

- [24] J. Han, D. Young, H. Colijn, A. Tripathi and S. Nešić, "Chemistry and Structure of the Passive Film on Mild Steel in CO<sub>2</sub> Corrosion Environments," *Ind Eng Chem Res*, vol. 48, pp. 6296-6302, 2009.
- [25] Y. Sun, "Localized CO<sub>2</sub> Corrosion in Horizontal Wet Gas Flow," PhD dissertation, Ohio Univ., Athens, OH, 2003.
- [26] R. G. Ehl and A. J. Ihde, "Faraday's electrochemical laws and the determination of equivalent weights," *J. Chem. Educ.*, vol. 31, pp. 226-232, 1954.
- [27] E. C. Potter, *Electrochemistry :Principles & Applications*. New York: Macmillan, 1956.
- [28] V. S. Sastri, *Corrosion Inhibitors :Principles and Applications*. Chichester; New York: Wiley, 1998.
- [29] R. G. Kelly, "Chapter1. introduction," in *Electrochemical Techniques in Corrosion Science and Engineering*, R. G. Kelly, J. R. Scully, D. W. Shoesmith and R. G. Buchheit, Eds. New York: Marcel Dekker, 2003, pp. 4-5.
- [30] J. A. V. Butler, "Studies in heterogeneous equilibria. Part II. - The kinetic interpretation of the nernst theory of electromotive force," *Transactions of the Faraday Society*, vol. 19, pp. 729-733, 1924.
- [31] J. A. V. Butler, "Studies in heterogeneous equilibria. Part III. A kinetic theory of reversible oxidation potentials at inert electrodes," *Transactions of the Faraday Society*, vol. 19, pp. 734-739, 1924.
- [32] J. A. V. Butler, "The Theory of the Hydrogen Overvoltage," *Journal of Chemical Physics*, vol. 9, pp. 279-280, 1941.
- [33] A. J. Bard and L. R. Faulkner, *Electrochemical Methods :Fundamentals and Applications*. New York: Wiley, 1980.
- [34] G. T. Burstein, "A hundred years of Tafel's Equation: 1905-2005," *Corros. Sci.*, vol. 47, pp. 2858-2870, 2005.
- [35] D. A. Jones, *Principles and Prevention of Corrosion*. Upper Saddle River, NJ: Prentice Hall, 1996.
- [36] W. H. Durnie, "Development of a structure/activity relationship for carbon dioxide corrosion inhibitors," PhD dissertation, Curtin Univ., Perth, Australia, 2000.

- [37] L. M. Callow, J. A. Richardson and J. L. Dawson, "Corrosion monitoring using polarisation resistance measurements - 2. Sources of error." *Br. Corros. J.*, vol. 11, pp. 132-139, 1976.
- [38] R. W. Bosch and W. F. Bogaerts, "Harmonic analysis of corroding systems considering diffusion phenomena," *J. Electrochem. Soc.*, vol. 143, pp. 4033-4039, 1996.
- [39] R. W. Bosch and W. F. Bogaerts, "Instantaneous Corrosion Rate Measurement with Small-Amplitude Potential Intermodulation Techniques," *Corrosion (Houston)*, vol. 52, pp. 204-211, 1996.
- [40] R. W. Bosch, J. Hubrecht, W. F. Bogaerts and B. C. Syrett, "Electrochemical frequency modulation: A new electrochemical technique for online corrosion monitoring," *Corrosion*, vol. 57, pp. 60-70, JAN, 2001.
- [41] W. Durnie, R. De Marco, A. Jefferson and B. Kinsella, "Harmonic analysis of carbon dioxide corrosion," *Corros. Sci.*, vol. 44, pp. 1213-1221, 2002.
- [42] D. W. Michael, "7. principles and application of the electrochemical quartz crystal microbalance," in *Physical Electrochemistry :Principles, Methods, and Applications*, I. Rubinstein, Ed. New York: M. Dekker, 1995, pp. 293-338.
- [43] J. Han, "Galvanic Mechanism of Localized Corrosion for Mild Steel in Carbon Dioxide Environments," PhD dissertation, Ohio Univ., Athens, OH, 2009.
- [44] Laboratory Testing Inc., "Certified Test Report," 2003.
- [45] H. Fang, "Low Temperature and High Salt Concentration Effects on General CO<sub>2</sub> Corrosion for Carbon Steel," M.S. thesis, Ohio Univ., Athens, OH, 2006.
- [46] E. Kuş and F. Mansfeld, "An evaluation of the electrochemical frequency modulation (EFM) technique," *Corros. Sci.*, vol. 48, pp. 965-979, 2006.
- [47] M. Drogowska, H. Menard, A. Lasia and L. Brossard, "Impedance study of the passive film on stainless steel 304 in pH 8 carbonate solution," *J. Appl. Electrochem.*, vol. 26, pp. 1169-1177, 1996.

## APPENDIX: MATHEMATICAL DESCRIPTION OF THE EFM TECHNIQUE

The complete mathematical description of the electrochemical frequency modulation (EFM) technique has been published by Bosch *et al.*<sup>1</sup>. This incorporates built-in activation, diffusion and passivation models that can be applied to different corrosion systems, each is described below.

### 1. Activation Model

In the activation model, EFM assumes the anodic and cathodic reactions are governed by charge transfer process. The theoretical basis of EFM is the Butler-Volmer equation:

$$i = i_{\text{corr}} \left[ \exp\left(\frac{\eta}{\beta_a}\right) - \exp\left(-\frac{\eta}{\beta_c}\right) \right] \quad (1)$$

The EFM technique uses a small overpotential ( $\eta$ ) with two sine waves of different frequencies as the input signal. The  $\eta$  value is defined by the following expression:

$$\eta = U_0 \sin \omega_1 t + U_0 \sin \omega_2 t \quad (2)$$

Where:

$\eta$  is the overpotential

$U_0$  is the amplitude of the applied potential

$\omega_1, \omega_2$  are two different frequencies

Combination of the equation (1) and (2) gives:

$$i = i_{\text{corr}} \left[ \exp\left(\frac{U_0 \sin \omega_1 t}{\beta_a}\right) \exp\left(\frac{U_0 \sin \omega_2 t}{\beta_a}\right) - \exp\left(-\frac{U_0 \sin \omega_1 t}{\beta_c}\right) \exp\left(-\frac{U_0 \sin \omega_2 t}{\beta_c}\right) \right] \quad (3)$$

---

<sup>1</sup> R. W. Bosch, J. Hubrecht, W. F. Bogaerts and B. C. Syrett, "Electrochemical frequency modulation: A new electrochemical technique for online corrosion monitoring," *Corrosion*, vol. 57, pp. 60-70, JAN, 2001.

Considering the Taylor series:

$$e^x = 1 + \frac{x}{1!} + \frac{x^2}{2!} + \frac{x^3}{3!} + \dots, \quad -\infty < x < \infty \quad (4)$$

If the applied potential is sufficiently small in equation (3), then the exponential terms in equation (3) above can be expanded in a Taylor series to the third order, neglecting all higher order terms:

$$\begin{aligned} i = i_{\text{corr}} \left\{ \left[ 1 + \frac{U_0 \sin \omega_1 t}{\beta_a} + \frac{1}{2} \left( \frac{U_0 \sin \omega_1 t}{\beta_a} \right)^2 + \frac{1}{6} \left( \frac{U_0 \sin \omega_1 t}{\beta_a} \right)^3 \right] \left[ 1 + \frac{U_0 \sin \omega_2 t}{\beta_a} + \frac{1}{2} \left( \frac{U_0 \sin \omega_2 t}{\beta_a} \right)^2 + \right. \right. \\ \left. \left. \frac{1}{6} \left( \frac{U_0 \sin \omega_2 t}{\beta_a} \right)^3 \right] - \left[ 1 - \frac{U_0 \sin \omega_1 t}{\beta_c} + \frac{1}{2} \left( \frac{U_0 \sin \omega_1 t}{\beta_c} \right)^2 - \frac{1}{6} \left( \frac{U_0 \sin \omega_1 t}{\beta_c} \right)^3 \right] \left[ 1 - \frac{U_0 \sin \omega_2 t}{\beta_c} + \right. \right. \\ \left. \left. \frac{1}{2} \left( \frac{U_0 \sin \omega_2 t}{\beta_c} \right)^2 - \frac{1}{6} \left( \frac{U_0 \sin \omega_2 t}{\beta_c} \right)^3 \right] \right\} \quad (5) \end{aligned}$$

Considering trigonometric relationships:

$$(\sin a)^2 = \frac{1}{2} (1 - \cos 2a) \quad (6)$$

$$(\sin a)^3 = \frac{1}{4} (3 \sin a - \sin 3a) \quad (7)$$

Applying these relationships to the second order and third order terms in equation (5), all higher order terms are eliminated. For example:

$$\left( \frac{U_0 \sin \omega_1 t}{\beta_a} \right)^2 = \left( \frac{U_0}{\beta_a} \right)^2 (\sin \omega_1 t)^2 = \left( \frac{U_0}{\beta_a} \right)^2 \frac{1}{2} (1 - \cos 2 \omega_1 t) \quad (8)$$

After several mathematical manipulations, equation (5) can be rearranged as a summation of currents of different frequencies, which contains harmonic and intermodulation currents:

$$\begin{aligned}
i = & i_{fr} + i_{\omega_1} \sin \omega_1 t + i_{\omega_2} \sin \omega_2 t - i_{2\omega_1} \cos 2\omega_1 t - i_{2\omega_2} \cos 2\omega_2 t - i_{3\omega_1} \sin 3\omega_1 t - \\
& i_{3\omega_2} \sin 3\omega_2 t + i_{\omega_2 \pm \omega_1} \cos(\omega_2 t - \omega_1 t) - i_{\omega_2 \pm \omega_1} \cos(\omega_2 t + \omega_1 t) + \\
& i_{2\omega_2 \pm \omega_1} \sin(2\omega_2 t - \omega_1 t) - i_{2\omega_2 \pm \omega_1} \sin(2\omega_2 t + \omega_1 t) + i_{2\omega_1 \pm \omega_2} \sin(2\omega_1 t - \omega_2 t) - \\
& i_{2\omega_1 \pm \omega_2} \sin(2\omega_1 t + \omega_2 t)
\end{aligned} \tag{9}$$

Where:

$i_{fr}$  is the Faraday rectification current

$$i_{\omega_1} = i_{\omega_2} = i_{corr} \left( \frac{1}{\beta_a} + \frac{1}{\beta_c} \right) U_0 \tag{10}$$

$$i_{2\omega_1} = i_{2\omega_2} = i_{corr} \left( \frac{1}{\beta_a^2} - \frac{1}{\beta_c^2} \right) \frac{U_0^2}{4} \tag{11}$$

$$i_{3\omega_1} = i_{3\omega_2} = i_{corr} \left( \frac{1}{\beta_a^3} + \frac{1}{\beta_c^3} \right) \frac{U_0^3}{24} \tag{12}$$

$$i_{\omega_1 \pm \omega_2} = i_{corr} \left( \frac{1}{\beta_a^2} - \frac{1}{\beta_c^2} \right) \frac{U_0^2}{2} \tag{13}$$

$$i_{2\omega_1 \pm \omega_2} = i_{2\omega_2 \pm \omega_1} = i_{corr} \left( \frac{1}{\beta_a^3} + \frac{1}{\beta_c^3} \right) \frac{U_0^3}{8} \tag{14}$$

By solving equations (10), (13), (14), (assuming  $\omega_2 > \omega_1$ ,  $\beta_a < \beta_c$ ), the  $i_{corr}$  and Tafel parameters are calculated in terms of the current with different frequencies:

$$i_{corr} = \frac{i_{\omega_1, \omega_2}^2}{2 \sqrt{8i_{\omega_1, \omega_2} i_{2\omega_2 \pm \omega_1} - 3i_{\omega_2 \pm \omega_1}^2}} \tag{15}$$

$$\beta_a = \frac{i_{\omega_1, \omega_2} U_0}{i_{\omega_2 \pm \omega_1} + \sqrt{8i_{\omega_1, \omega_2} i_{2\omega_2 \pm \omega_1} - 3i_{\omega_2 \pm \omega_1}^2}} \tag{16}$$

$$\beta_c = \frac{i_{\omega_1, \omega_2} U_0}{-i_{\omega_2 \pm \omega_1} + \sqrt{8i_{\omega_1, \omega_2} i_{2\omega_2 \pm \omega_1} - 3i_{\omega_2 \pm \omega_1}^2}} \tag{17}$$

By measuring the current responses at different frequencies to the applied potential perturbation, the corrosion rate and the Tafel parameters are determined. In addition, the currents at different frequencies in equations (11), (12), (13) and (14) have the following relationships:

$$\frac{i_{\omega_1+\omega_2}}{i_{2\omega_1,2\omega_2}} = 2 \quad (18)$$

$$\frac{i_{2\omega_1+\omega_2,2\omega_2+\omega_1}}{i_{3\omega_1,3\omega_2}} = 3 \quad (19)$$

The EFM technique uses these relationships to corroborate the reliability of the acquired data; when the ratios of the measured currents at different frequencies are close to the theoretical values (2 and 3), then the data is considered valid. These relationships are called Causality Factor 2 and 3, respectively.

## 2. Diffusion Model

In the diffusion model, a central assumption is that the cathodic reaction is fully governed by mass transfer process. The cathodic Tafel parameter  $\beta_c$  is then assumed to be infinite. EFM assumes the Butler-Volmer equation is again applicable in this case. Hence, equation (1) can be rewritten as:

$$i = i_{\text{corr}} \left[ \exp\left(\frac{\eta}{\beta_\alpha}\right) - 1 \right] \quad (20)$$

Applying the same potential perturbation ( $\eta$ ) described in equation (2) and using the same mathematical manipulations,  $i_{\text{corr}}$  and  $\beta_\alpha$  can be determined:

$$i_{\text{corr}} = \frac{i_{\omega_1,\omega_2}^2}{2i_{\omega_2+\omega_1}} \quad (21)$$

$$\beta_a = \frac{i_{\omega_1,\omega_2} U_0}{2i_{\omega_2+\omega_1}} \quad (22)$$

In diffusion model, only  $i_{\omega_1 \pm \omega_2}$  and  $i_{\omega_1, \omega_2}$  are presented in the expressions of  $i_{\text{corr}}$  and  $\beta_a$ . Therefore, Causality Factor 2 is deemed suitable for evaluation of data reliability. Calculation of Causality Factor 3 is unnecessary in this case.

### 3. Passivation Model

Similarly, in the passivation model, EFM assumes the anodic reaction is fully controlled by passivation process. The anodic Tafel parameter  $\beta_a$  is assumed to be infinite. Therefore, equation (1) can be rewritten as:

$$i = i_{\text{corr}} \left[ 1 - \exp \left( -\frac{\eta}{\beta_c} \right) \right] \quad (23)$$

Applying the same potential perturbation ( $\eta$ ) and mathematical manipulations described in section 1,  $i_{\text{corr}}$  and  $\beta_c$  can be determined:

$$i_{\text{corr}} = \frac{i_{\omega_1, \omega_2}^2}{2i_{\omega_2 \pm \omega_1}} \quad (24)$$

$$\beta_c = \frac{i_{\omega_1, \omega_2} U_0}{2i_{\omega_2 \pm \omega_1}} \quad (25)$$

Similarly, in passivation model, only  $i_{\omega_1 \pm \omega_2}$  and  $i_{\omega_1, \omega_2}$  are presented in the expressions of  $i_{\text{corr}}$  and  $\beta_c$ . Therefore, Causality Factor 2 is deemed suitable for evaluation of data reliability. Calculation of Causality Factor 3 is unnecessary in this case.